

# **Processability and Characterisation of Innovative Materials for Cutting Elements**

Ines Vega-Prieto

4866428

TU Delft Supervisor: Prof.dr.ir. J. Sietsma

P&G Supervisors: Dr. E. Sabattié and Dr. D. Korn

Date of submission: 24.06.2021

Date of Thesis Defence: 02.07.2021

# Abstract

Essential criteria to a shaving blade include wear resistance, corrosion resistance and a sharp cutting edge. The material selection for improved cutting elements as well as increasing the longevity of the blade would provide benefits not only to the consumer experience of a more efficient shaving performance, but also a more sustainable solution to the recurring disposal of blunt razors. Amorphous metals, also called metallic glasses, have been exploited in recent technological and structural development due to the superior mechanical and electrochemical properties associated with the unique structure. As opposed to standard crystalline metals, amorphous metals are cooled at high rates to maintain a “glass-like” disordered atomic structure without grains or grain boundaries. From this, properties such as corrosion resistance and hardness are prominently improved compared to the crystalline metals. Additionally, due to the lack of crystalline structure, amorphous metals can be sharpened to a nanometer-level cutting edge. For these reasons, metallic glasses have been explored as the next generation innovative cutting material for shaving. The practical aspect of this project involved the processing of amorphous metals through currently established industrial processes in the production of cutting elements. The materials were then characterised analytically through thermal analysis, hardness measurements, corrosion resistance analysis, and the rate of nickel release. Understanding and outlining the benefits and challenges of implementing metallic glasses in shavers were explored through prototyping. Throughout the experimental procedure of this project, the amorphous metals were constantly compared to traditional shaving materials to highlight the superior qualities achieved.

# Acknowledgements

I am very grateful to all the people who have supported me in the completion of this thesis. A huge thank you to my TU Delft supervisor, Jilt Sietsma, for your constant patience and thoughtful insight on the topic, making me look forward to our 8 A.M. meetings. I also greatly appreciate your support during the difficult period with Covid-19 for both the internship and thesis project.

Having the opportunity to carry out this project with Procter & Gamble, I have been fortunate to meet and collaborate with a range of teams and expertise. To Elise Sabattié and Andrea Schuering, my P&G supervisor and manager, your guidance and encouragement throughout the development of the project motivated me on a daily basis. To my technical coaches, Dietmar Korn and Andreas Moehring, the countless material science discussions we have had were not only invaluable, but thoroughly enjoyable. Spending most of the days in the lab with H. Miguel Perez-Molina was a highlight of this experience, achieving PM results from running programs at full-power.

Completing this materials science and engineering degree at TU Delft has been an incredible experience overall. To my friends in Delft: Can, Kelsey, Rohan, and Luis, you have all had a major impact on both my academic achievements as well as my personal growth. Finally, my parents have always encouraged my scientific curiosity – gracias por todo!

# Table of Contents

1.	Introduction.....	5
1.1	Context .....	5
1.2	Replacing Stainless Steel Cutting Elements .....	6
1.3	Sustainability of Shavers .....	8
1.4	Elemental Consideration .....	9
1.5	This Thesis .....	10
2.	Background on Amorphous Metals .....	12
2.1	Glass Forming Ability .....	12
2.2	Methods of Producing Metallic Glass .....	14
2.2.1	Melt Spinning.....	15
2.2.2	3D Printing: Selective Laser Melting.....	15
2.2.3	Injection Molding.....	16
2.3	Atomic Structure .....	17
2.3.1	Atomic Packing.....	17
2.3.2	Structural Relaxation, Internal Free Volume and Glass Transition.....	19
2.3.3	Crystallisation from Amorphous Structure .....	22
2.4	Mechanical Properties .....	24
2.5	Corrosion Resistance .....	26
3.	Materials and Methods.....	29
3.1	Materials.....	29
3.1.1	Amorphous Metal Samples .....	29
3.1.2	Reference Materials .....	30
3.2	Processing Methods.....	30
3.2.1	Photochemical Machining (Etching).....	30
3.2.2	Precision/Pulse Electrochemical Machining (PECM).....	32
3.3	Material Characterisation .....	34
3.3.1	Thermal Analysis .....	34
3.3.2	Hardness.....	35
3.3.3	Corrosion Resistance.....	37
3.3.4	Nickel Release.....	39
4.	Results.....	41
4.1	Processing.....	41
4.1.1	Photochemical Machining (Etching).....	41
4.1.2	Precision/Pulse Electrochemical Machining (PECM).....	46
4.1.3	Comparing Etching and PECM.....	50
4.2	Material Characterisation .....	52
4.2.1	Thermal Analysis .....	53
4.2.2	Hardness.....	55
4.2.3	Corrosion Resistance.....	58

4.2.4 Nickel Release.....	62
5. Discussion .....	65
5.1 Processability .....	65
5.2 Characterisation.....	65
5.3 Integration in Shaving Appliance .....	66
5.4 Trade-Offs .....	67
6. Conclusion .....	68
References .....	69

# 1. Introduction

## 1.1 Context

An exciting aspect of materials science and engineering is the investigation and finding of the most suitable and efficient material for specific applications. Whether this involves replacing outdated materials with innovative solutions from advancing technology or utilising more sustainably sourced primary components, all contributions to the field provide an impactful resolution.

With the different trends and fashions throughout the centuries, men have used shavers to trim, shape or fully shave their facial hair. Durability and effective cutting capability are at the forefront in electrical shaver requirements. These properties are greatly influenced by the materials selected for the shaving blades. This research project was carried out with the Material Process and Delivery (MPD) department in Procter & Gamble GIC-K and is dedicated to the processability and application of new and innovative materials for cutting elements in shavers.

The class of material under investigation as the next generation cutting element for this project was amorphous metals, also called metallic glasses. This involved the verification and proof of principle of the processability of amorphous metals through currently established industrial processing methods. A strong collaboration with the Analytical department of P&G also allowed for the characterisation of the material to be carried out parallel to the processing of the metals. With the material science understanding of amorphous metals as well as the engineered cutting element prototypes, discussions with the Front-End Innovation (FEI) department at P&G were necessary to find the most intelligent integration of the metallic glass in shaving devices.

Amorphous metals are formed through the rapid cooling of molten alloys, resulting in the atoms “locked” in a disordered structure at the atomic scale. Figure 1 schematically illustrates the fundamental difference between amorphous metals and crystalline materials.

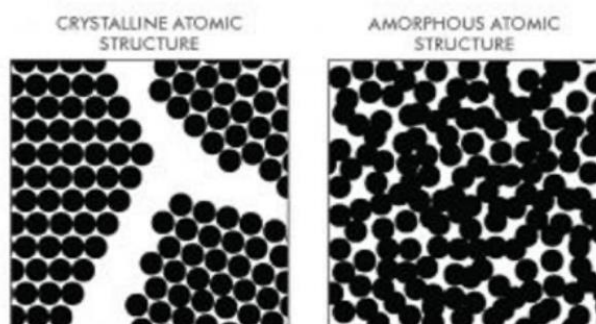


*Figure 1: Illustration of the microstructure, where the circles symbolise atoms of, (left) ordered grains in crystalline materials and (right) disordered amorphous metals [1]*

Amorphous metals have been identified as potential next generation materials for commercial electric shavers due to the superior properties associated to the unique structure. With respect to the application in

shavers, metallic glasses are attractive due to the high hardness relating to its resistance to repeated wear, excellent corrosion resistance and the ability to obtain a sharp cutting edge.

From the conclusions and understandings brought on by the literature study, as well as the results from the six-month internship carried out prior to this master's thesis on the similar topic of the processability of amorphous metals, the title of the thesis project was extended to the processability and characterisation of the innovative cutting material. Three research questions were developed based on these findings to guide and refine the experimental investigation:

1. How does the composition of the amorphous metal influence the processability of the material?
2. Are the advantageous amorphous metal properties maintained after processing?
3. How can amorphous metals be best utilised as cutting elements in shavers?

The first question relates to understanding how the composition of the amorphous metal can influence the method through which it is machined into a final cutting element. These results could also facilitate future decisions based on understanding the correlation between the composition of elements present in the amorphous alloy and the specific techniques used to produce the shaving element. The second question is aimed at not only exploring the unique properties that amorphous metals exhibit due to the nature of the structure, but also to verify that the processing does not cause unwanted physical or chemical alterations to the structure resulting in changes in the superior mechanical and electrochemical properties. Since it is the processed piece that would be implemented in the final shaving product, it is important to highlight these properties after processing. Finally, the third question explores the most suitable application of the scientific and engineering knowledge of metallic glasses into a real-world product for consumers.

An engaging and enjoyable experience of this project was the interdepartmental collaboration at P&G, as each research question related to one of the three departments: Material Process and Delivery (MPD) through processing, Analytical through the characterisation of the material and Front-End Innovation (FEI) for the application and prototyping, respectively.

## 1.2 Replacing Stainless Steel Cutting Elements

Throughout each of the different aspects of this project with the processing and characterisation of the metallic glass, it was essential to constantly compare to the standard reference materials used in shavers today, stainless steels. For the past several decades, stainless steel has been used as razors blades for shavers. In August 2020, a research article from MIT outlining the metallurgical aspects of how hair deforms steel by Roscioli *et al.* [2] provided great insight into how the steel becomes deformed after repeated use. Figure 2 summarises the key findings of the materials and mechanics of the shaving process.

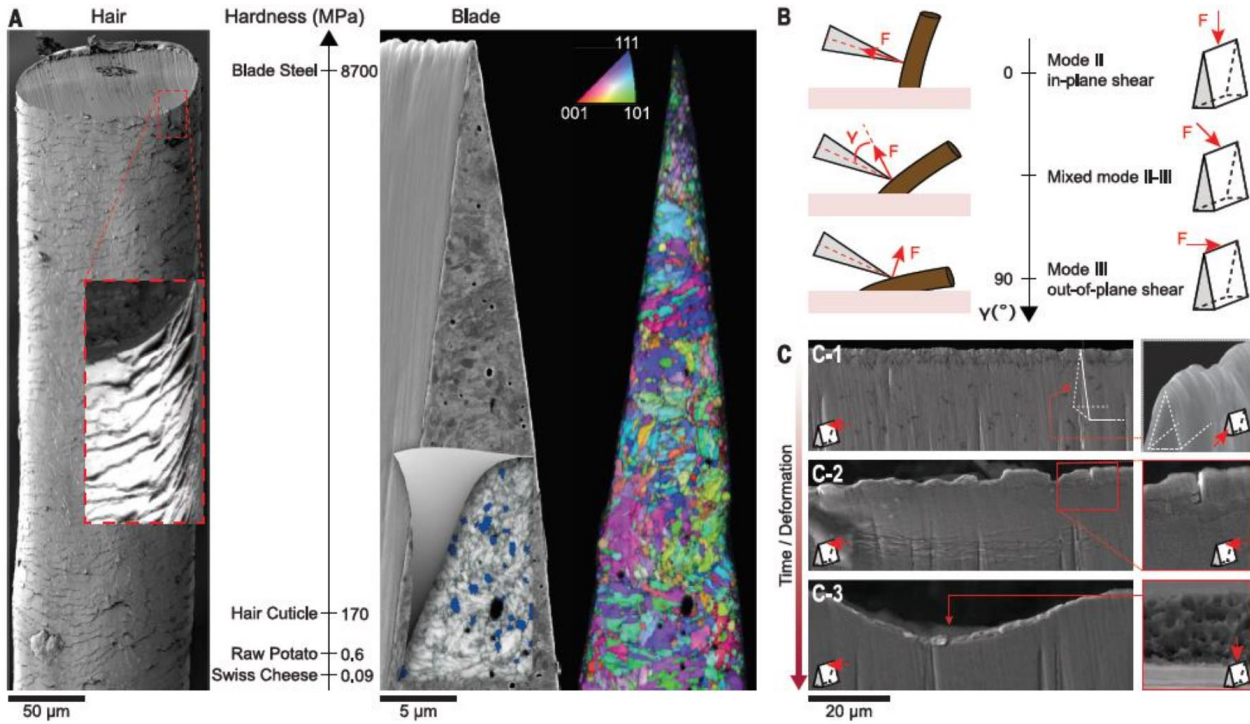


Figure 2: Interaction between hair and martensitic stainless steel during shaving process [2]

Figure 2 (A) outlines the human hair (left) and martensitic stainless steel blade (right) with their internal structure. The hair is a layered anisotropic material whilst the steel has a fine lath martensitic matrix. The hardness scale between the two emphasises the difference in hardness of these two materials, showing the steel hardness to be about 50 times greater. Figure 2 (B) shows how the stress state on the blade during the cutting of the hair depends on the force angle  $\gamma$ . It shows the configurations between the in- and out-of-plane shear that are possible. Finally, Figure 2 (C) shows the images of deformation from an unused blade (C-1), to the initial crack nucleation at the sharp edge and localised bending (C-2) and the final ductile failure (C-3) [2].

Although the steel is 50 times harder than the human hair, people are required to throw away their razor every few weeks. Initially believed to be due to the sharp tip becoming blunt, it was found that the interaction between the hair and the steel caused cracking and chipping at the edge [3]. Three critical factors for lath martensite failure during the cutting of hair include: i) the incidence angle at which the hair comes into contact with the blade, ii) microstructural heterogeneity, as it was found that cracks formed at the boundaries where soft and hard areas of the steel meet, and iii) the relative position of the cracked edge of the blade to the hair being cut [2]. It is stated that the probability of failure of the cutting element depends on whether these conditions are met simultaneously [2].

As opposed to martensitic stainless steel, amorphous metals have a homogenous atomic structure; it is a single phase, without grains, or grain boundaries. Therefore, there are no boundaries between soft and hard areas where the cracks can form (Point ii from the previous paragraph), thereby reducing the formation of cracks.

Moreover, additional microcracks will form in martensitic stainless steel from carbide cracking or carbide matrix decohesion and further open as micro-voids [4]. Point iii relates to the interaction between the position of the incoming hair to the asperity on the edge of the material. With the premise that there is a smaller probability of crack formation on the edge of an amorphous metal blade, this would reduce the probability of a hair coming into contact with a crack edge. For these reasons it is suggested that the design of a hard but more homogenous microstructure be used for cutting tools. This can be achieved by having a finer structure at sharp edges, using nanostructured alloys, or by avoiding crystallinity altogether [5] [6].

### 1.3 Sustainability of Shavers

A crucial factor when making commercial products is sustainability. This can take form in a variety of ways: responsibly sourced materials with respect to environmental and social implications, longer product lifetimes, recyclable materials, cradle-to-cradle designs to minimise disposal, etc.

Although shavers seem to be a trivial product, in 1990 the Environmental Protection Agency reported that the United States produced 2 billion disposable razors and blades [7], which ultimately collect in landfills. Replacing stainless steel with amorphous metals would increase the longevity of the shaver, allowing consumers to use a single blade for a longer period of time. Often the reasons to throw away a shaver are due to cutting tip bluntness or metal deterioration caused by corrosion. The wear resistance, characterised by the hardness, of metallic glasses as well as the corrosion resistance could offer consumers more repeated use resulting in fewer disposal rates.

The energy required to produce the primary materials is also to be taken into consideration. Metallic glasses can be produced in the form of ribbons and wires much more economically and environmentally friendly than traditional metals, since energy intensive processes such as rolling and drawing are not necessary [8]. Additionally, amorphous metal ribbons produced via melt spinning can be produced at a rate of approximately 1.5 kilometers per minute [9]. This aspect becomes significant when regarding the mass production of shavers.

The recycling of amorphous metals could be challenging due to different and complex alloying compositions used for varying purposes. However, the recycling of specific amorphous metal appliances with the same composition offer a start to the progress. In February 2013, Hitachi Metals announced the establishment of a recycling plant dedicated for amorphous metals used in amorphous transformers. This facility will process, melt and reuse amorphous metal materials [10]. With a plant already in function in 2011, Hitachi Metals have been involved in the separation process; removing the amorphous cores from scrapped transformers and removing any insulating oil and other impurities that adhere to the cores [11]. Should amorphous metals be used as cutting elements in electric shavers, partnering metallic glass producers with shaver manufacturers to arrange a collection and recycling scheme could offer not only a more sustainable conclusion to end of life shavers but possibly a more economical solution as well.

## 1.4 Elemental Consideration

The elemental composition of the amorphous alloy can be a factor in the discussion of sustainability with respect to the sourcing of the material. Additionally, the metals in question are to be used in direct contact to the face and must therefore have an aspect of biocompatibility.

Figure 3 illustrates the overall results of the 2020 criticality assessment of raw materials by the European Commission [12]. This is based on the supply risk with respect to the material's economic importance.

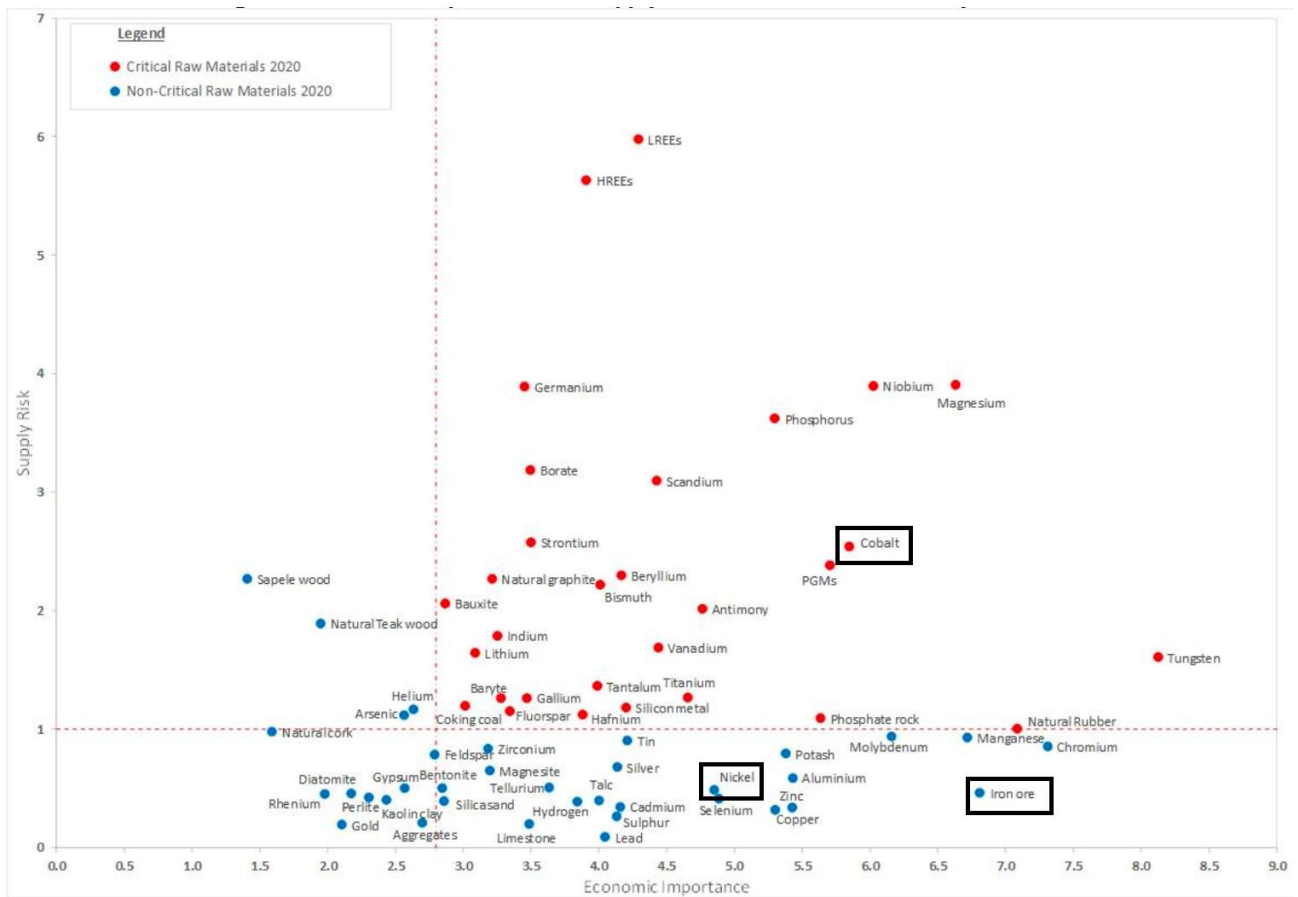


Figure 3: Economic importance and supply risk of 2020 criticality assessment. The red dots represent the critically assessed raw materials and the blue dots are non-critical raw materials [12]. The boxes outline nickel, iron and cobalt.

Amorphous metals are often based with transition metals such as iron, nickel and cobalt. Figure 3 shows that the iron ore is of economic importance with no current supply risk associated to it. Cobalt, on the other hand, is shown to be labelled as a critical raw material. There are also humanitarian violations associated with the sourcing of cobalt in the Democratic Republic of Congo (DRC). In 2016 Amnesty International published a report entitled “This is what we Die for” [13] outlining the human rights abuses in order to source the increasing demand for cobalt. “Artisanal miners”, as they are referred to, is understood to mean “mining by hand”, using rudimentary tools and most often their bare hands. Fatal accidents due to tunnel collapses and underground fires killing these miners often go unreported [14]. Furthermore, another reason why the mining of cobalt in the DRC has been under investigation is the use of children, ages between 7 and 16 years old [13].

Like the adults, the children are not wearing masks, gloves or protective clothing. The constant exposure of cobalt in dust leads to respiratory problems such as asthma and decreased pulmonary function [15].

Nickel is not considered a critical raw material. However, nickel allergies are common throughout the population, often triggered by jewellery and dentistry [16]. Studies have shown that between 12-15% of women and 1-2% of men are allergic to nickel [17]. Nickel ions are released, penetrate into the skin and can result in skin inflammation [18]. With more increasing awareness and understanding, an EU Directive was set in place in 1994 to limit the sensitisation of nickel and its related toxicity [19]. The conditions for NACD (Nickel Allergic Contact Dermatitis) are the direct skin contact with nickel-releasing items through prolonged skin exposure to nickel and the amount of nickel released being above a set threshold. It was also stressed that it is the nickel release, and not nickel content, that is the critical factor in assessing the risk associated with the nickel allergy or NACD [19].

The European Union restriction on the Nickel Directive has established limits to the levels of nickel release, separated into two categories [17]:

- a) "...assemblies which are inserted into pierced ears and other pierced parts of the human body unless the nickel release is less than  $0.2 \mu\text{g}/\text{cm}^2/\text{week}$ ."
- b) "...articles intended to come into direct and prolonged contact with the skin such as: earrings, bracelets, rings, [etc.] if the Nickel release rate from the parts of these articles coming into direct and prolonged contact with the skin is greater than  $0.5 \mu\text{g}/\text{cm}^2/\text{week}$ ."

The definition of "prolonged contact" was also established as [17]:

- "More than 2 hours for one occurrence within two weeks, or
- More than 30 minutes for three occurrences within two weeks"

Although the act of shaving may not fall into the category of prolonged contact, there are reports highlighting nickel related dermatitis from electric shavers [20]. Therefore, reducing the nickel release by replacing the nickel element in the shaver with an amorphous metal with low levels of release could reduce the chance of this dermatitis.

## 1.5 This Thesis

This report begins with Chapter 2, a literature review introducing amorphous metals from the fundamental basics to the complex theories developed throughout the decades. The physical and kinetic phenomenon of the internal free volume as well as its relation to the glass transition of amorphous metals is explained, including susceptibility of crystallisation. The advanced mechanical and electrochemical properties of amorphous metals are illustrated. Chapter 3 introduces and describes the materials used in the practical investigation of the project and an explanation of the processing and analytical characterisation experiments. The results are outlined in Chapter 4 following the same order as highlighted in the previous section, with relevant discussion of the data.

The overall discussion of the application of amorphous metals as cutting elements in shavers is detailed in Chapter 5, reviewing the three research questions mentioned in the introduction. This report concludes in Chapter 6 outlining the main conclusions and future considerations. The literary sources are listed at the end in order of appearance, following the reference of experts within P&G that have contributed to the results achieved in this thesis, emphasised throughout the text as [PG].

## 2. Background on Amorphous Metals

### 2.1 Glass Forming Ability

Amorphous metals are formed through the rapid quenching of molten alloys which results in a disordered structure at the atomic scale [21]. In order to maintain a glassy (disordered) state upon cooling, and avoid crystallisation, a sufficiently high cooling rate must be applied to prevent nucleation of the crystalline phase [22]. In the mid to late 1900's, the required cooling rate ranged from  $10^5$  to  $10^6$  K/s [23] resulting in very low thickness of the first generation of amorphous metals (Au<sub>75</sub>Si<sub>25</sub> alloy [24]) that were being developed.

To overcome this challenge, in 2000 Inoue *et al.* [25] were able to develop metallic glass alloy systems, “Bulk Metallic Glasses”, that required lower cooling rates. The fundamental reason behind this success was the involvement of different kinds of elements in the alloy system, with significantly different atomic sizes [21]. Inoue summarised these findings as the “three empirical rules” to making amorphous metals with relatively low cooling rates [25]:

- 1) “Multicomponent systems consisting of more than three elements
- 2) Significant difference in atomic size ratios, above 12% among the three main constituent elements
- 3) Negative enthalpy of mixing among the three main constituent elements”

With these rules in place, it was found that specific alloys have a high Glass-Forming Ability (GFA) [22] [25]; referring to the ease of vitrification of an alloy to form an amorphous structure by suppressing nucleation of crystals when cooled [26]. By cooling the liquid below the melting temperature,  $T_m$ , with a sufficiently high quench rate to impede crystallisation, the supercooled liquid will reach a metastable state with a high viscosity [27]. These alloys should have a low driving force for crystallisation [28]. The glass-forming ability is therefore often interpreted through the critical cooling rate,  $R_c$ , (the lowest quenching rate avoiding crystallisation); the greater the GFA of the alloy, the lower this rate [27].

Thus, the complexity of the alloy also influences the maximum (critical) thickness an amorphous metal can obtain [27]. The correlation between the GFA and the maximum thickness at which alloys still have an amorphous microstructure, by maintaining the same cooling rate of casting and varying the thickness of the amorphous metal casted in the mould, was explored by Senkov *et al.* [29]. The findings presented in the research show the maximum thickness at which different calcium-based alloys remain fully amorphous during copper mould casting. The X-Ray diffraction patterns in Figure 4 illustrate the wide and diffuse halo observed for amorphous metals at low thicknesses (green box). However, once the thickness becomes too large, the material crystallises as seen with sharp and distinct peaks in the spectra (red box). The maximum thickness for Figure 4 (a) and (b) of the specified alloys is between 6 and 8 mm for Ca<sub>53</sub>Mg<sub>23</sub>Cu<sub>24</sub> and between 10 and 13 mm for Ca<sub>58</sub>Mg<sub>18</sub>Zn<sub>12</sub>Cu<sub>12</sub>.

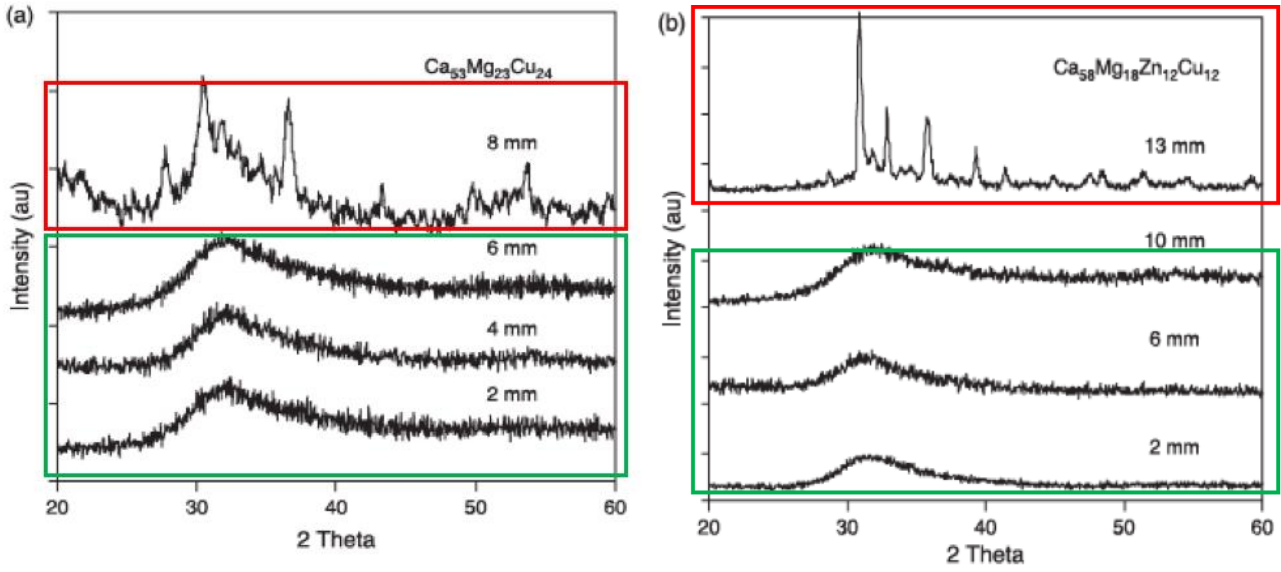


Figure 4: X-Ray Diffraction patterns taken from various thicknesses of (a)  $\text{Ca}_{53}\text{Mg}_{23}\text{Cu}_{24}$  and (b)  $\text{Ca}_{58}\text{Mg}_{18}\text{Zn}_{12}\text{Cu}_{12}$  cast alloys [30]

There is a relationship between GFA and the maximum thickness as seen in Figure 4; alloys with more complex elemental compositions achieve a higher thickness and are better glass formers [29]. As seen in these figures, the desired amorphous microstructure is replaced by crystallinity when surpassing the critical thickness of the metallic glass.

The processes in which the amorphous metals can be manufactured traditionally include casting, melt spinning or gas atomisation. More recent advances include additive manufacturing techniques as well [27]. Figure 5 classifies various metallic glasses according to their critical cooling rate ( $R_c$ ) and critical thickness ( $d_c$ ) alongside the processing techniques and the range of their respective cooling rates. Along the x-axis is the quantity  $T_g/T_{liq}$ , the ratio of the glass transition temperature,  $T_g$  (further in Section 2.3.2) and the melting temperature of the alloy  $T_{liq}$ .



### 2.2.1 Melt Spinning

One of the most common methods of producing amorphous metals is through melt spinning, with cooling rates of up to  $10^4$  to  $10^6$  K/s [33], as required to prevent the formation of crystals for relatively simple compositions. Ribbons of metallic glass are produced with a ranging thickness of 10 to 75  $\mu\text{m}$ . More complex alloys are also formed commercially today through melt spinning.

The alloy is melted in a crucible (typically made of boron nitride that can withstand high temperatures [34]) and heated by an induction coil, as seen in Figure 6 (left). Nozzles at the bottom of the crucible allow the outlet of the molten alloy, the configuration of which determines the resulting dimensions of the ribbon. Beneath the crucible is a rotating refrigerated copper drum which absorbs a large part of the heat that is released upon quenching [34]. A pressure is applied above, pushing the liquid alloy through the nozzles and the liquid is cooled rapidly as it makes contact with the copper drum. This is illustrated schematically (left) and in real life processing (right) in Figure 6.

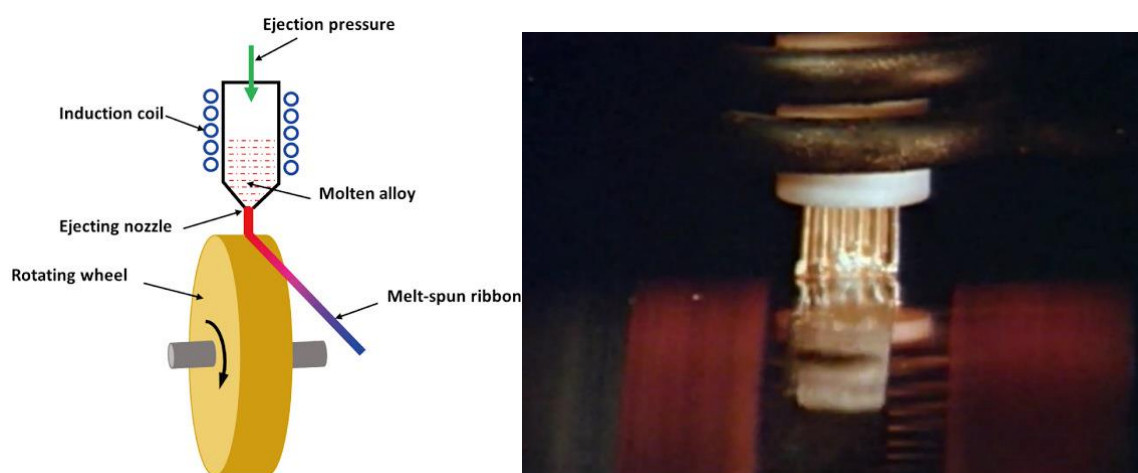


Figure 6: Schematic of melt spinning (left) [35] and screenshot of live slow-motion video (right) [34] in a range of 10 to 75  $\mu\text{m}$  in thickness

The melt should impinge on the drum in a laminar flow and at an angle that allows a constant thickness to be maintained throughout the product [34]. If the adhesion between the drum and the alloy is not sufficient, the molten metal will not form a ribbon but instead coalesce into droplets. The melt spun ribbon is collected and coiled. Research shows that the physical properties associated with melt-spun ribbons, as well as thermal stability of non-equilibrium structures, is dependent on the parameters of the process such as the speed of the wheel, gas ejection pressure, the gap between the nozzle and wheel, etc. [33].

### 2.2.2 3D Printing: Selective Laser Melting

More recently, amorphous metals are being produced via 3D printing (specifically Selective Laser Melting) with increasing popularity. With the use of aided design components (CAD), specific shapes and geometries can be structured. Figure 7 illustrates the process.

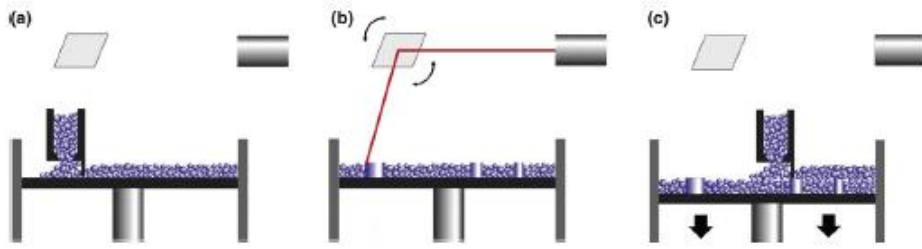


Figure 7: Illustration of SLM process [36] layers of metal powder ranging from 20-100  $\mu\text{m}$  in thickness [37]

Figure 7 (a) shows a layer of powder on a base plate. Following this, Figure 7 (b), a high-power laser selectively melts the powder in spots that were previously determined by the 3D CAD model with a ranging thickness between 20 to 100  $\mu\text{m}$  [37]. This melt solidifies quickly and fuses with the structure in the layer below. Once this is complete, the entire base plate is lowered and the powder layer is added, Figure 7 (c), continuing with the next layer of the designed shape [36].

Due to the small interaction volume (few hundred microns<sup>3</sup>) [38] between the laser beam and the material during this process, this method allows for very high cooling rates ( $10^3$  to  $10^8$  K/s) [39]. Through this, the amorphous microstructure can be theoretically tailored by influencing the processing parameters such as the laser energy, scan speed, layer thickness and lens focus offset [38].

The main advantages of this process are the versatility of product design and geometry. In combination with the biocompatibility exhibited by certain amorphous metal alloys, this technique has modernised the field of medical research, since prosthetics can not only be made from metallic glasses with excellent mechanical properties, they can be made patient specific. However, studies have shown that 3D-printing specimens results in poor ductility and the presence of micro-cracks forming during the SLM process, triggered from thermal stress concentration around micro-pores [32].

### 2.2.3 Injection Molding

Injection moulding has both the advantage of achieving larger thicknesses, through a lower cooling rate for certain alloys, than melt spinning, as well as a final desired shape. Hence, this process is more common for application in aerospace and the automotive industry [40]. *Liquidmetal Technologies* describe the process in which amorphous metals can be injection moulded, through the use of a vacuum chamber to avoid oxygen contamination [41], as seen in Figure 8.

## The Liquidmetal Process

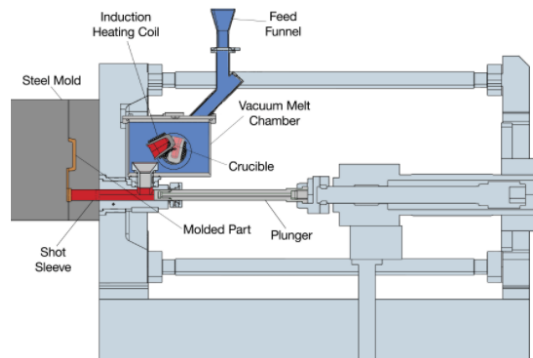


Figure 8: Amorphous metal injection moulding process by Liquidmetal, maximum sample dimension of 100 mm [41]

The process begins as it does in melt spinning, by inductively heating the metallic alloy and reaching temperatures up to 1000°C. Once the alloy is fully liquified (in some cases after 1-2 minutes of the melting period) the alloy is injected into the mould. Subsequent to the injection, the alloy freezes in the mould, forming an amorphous metal in the net shape and is ejected from the mould. The sample is removed from the gate initially with waterjet for a rough and quick extraction, finished with further machining for the precise polish [41]. Unlike traditional metals, there is little to no shrinkage during the solidification in the mould due to the absence of crystallisation allowing for more consistent precision [42].

## 2.3 Atomic Structure

### 2.3.1 Atomic Packing

Amorphous metals have no crystal lattice and therefore no periodicity or long-range order. There are no defects such as grain boundaries or dislocations as seen in crystal structures. Figure 9 illustrates the fundamental differences between the crystalline and amorphous structure at the atomic level through the transmission electron microscope (TEM) and the inset (top right-hand corner image) through selected-area electron diffraction (SAED).

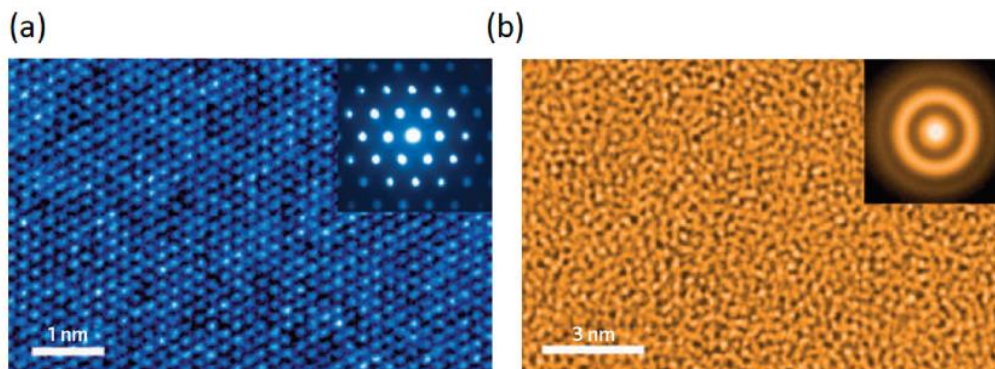


Figure 9: Atomic-level structures of (a) crystalline low-carbon steel and (b) amorphous  $Zr_{67}Ni_{33}$ . Main image is of high-resolution TEM and inset is of corresponding SAED pattern in right corner [27]

The TEM image of a low carbon crystalline steel (Figure 9 (a)) shows well defined long-range order of the lattice planes with the corresponding SAED pattern showing sharp crystalline spots, whereas those of the amorphous  $\text{Zr}_{67}\text{Ni}_{33}$  metallic glass in Figure 9 (b) show a “maze-like” pattern and diffusive haloes respectively [27].

Research has progressed to interpreting short-range order in the structure, at a level of nearest-neighbour atomic coordination. Medium-range order (positional correlations over 1 to 2 nm) however, is more difficult to characterise as there are no unit cells and the atomic environments within a given structure are diverse [22]. The modelling of the metallic glass atomic structure has continuously developed as more experimental and computational research provide further information.

One of the initial difficulties in characterising the structure of metallic glasses is how to pack 3D space with hard spheres without introducing crystalline order [23]. Bernal in 1964 [43] founded the idea of the Dense Random Packing (DRP) model, geometrically and statistically reproducing the possible structure of initially simple liquids, later applied to metallic glasses. Given the notion that there should not exist an empty space between atoms large enough to accommodate an additional atom, five basic polyhedral units are likely to be present in an amorphous structure [23], as seen in Figure 10. The tetrahedral and octahedral voids (the smaller holes) occur the most often [22].



Figure 10: Dense Random Packing of hard spheres: polyhedra formed according to Bernal [44]

Although this was a starting point, it failed to predict interactions between metalloid nearest neighbours in early metal-metalloid glasses. Through the interpretation of computational and experimental Radial Distribution Function, Gaskell [45] proposed the Local Coordination model which suggests that the nearest-neighbour coordination of metalloid atoms in metal-metalloid glasses is equivalent to the corresponding crystalline compound [22]. The metalloid in the  $\text{M}_3\text{N}$  crystal, where M is the metal and N the metalloid [45], has nine neighbouring metal atoms and the basic coordination of polyhedron is a trigonal prism (six nearest neighbours and three further away). Recognising the partially covalent atomic bonds, this model is shown in Figure 11 for amorphous compositions of  $\text{M}_3\text{N}$  [45].

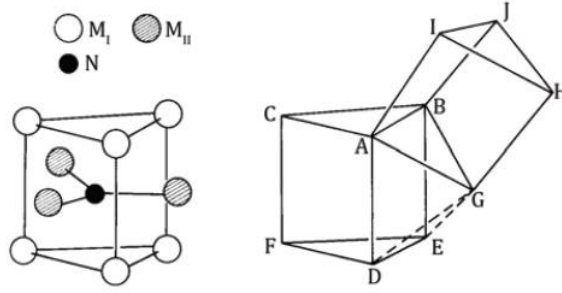


Figure 11: Packing of trigonal prisms with a metalloid atom at its center [45]

To give further information on the short/medium-range order, Miracle [46] explores the densest possible packing of atoms of different sizes through the concept of efficiently filling space, considering that the density difference between metallic glasses and their crystalline equivalent is less than 0.5% [47]. Figure 12 was suggested as a way to efficiently pack the solute-centered clusters of quaternary alloys and fill in the space.

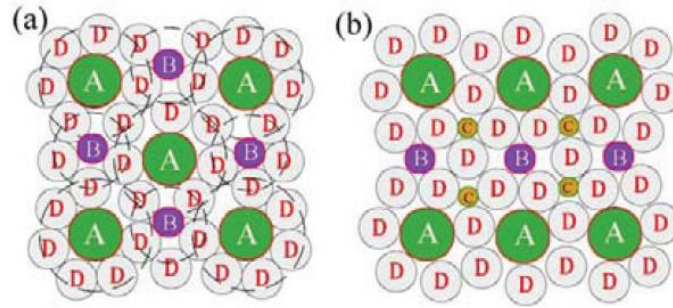


Figure 12: Schematic representation of a dense cluster-packing structure in planes (a) (100) and (b) (110) [47]

In this model, the cluster consists of a primary solute A, surrounded by solvent atoms D. Additionally, secondary B solute atoms (in the cluster-octahedral interstices) and tertiary C solute atoms (in the cluster-tetrahedral interstices) are topologically distinct. This model is named the Efficient Cluster Packing (ECP) model [47]; adjacent clusters share solvent atoms in common edges, vertices or faces resulting in neighbouring clusters overlapping in a dense packing 3D space. This in fact shows that although long-range order is not present, the atomic-level structure is not random and has distinctive short and medium-range order.

### 2.3.2 Structural Relaxation, Internal Free Volume and Glass Transition

As described, in order to prevent melted metal from crystallising, and promote vitrification, the melt must be cooled at a rate exceeding that of the critical cooling rate value,  $R_c$ . Figure 13 is a schematic of a Continuous Cooling Transformation (CCT) diagram, illustrating the effect of cooling rates in the formation of glass, crystals and supercooled liquids.

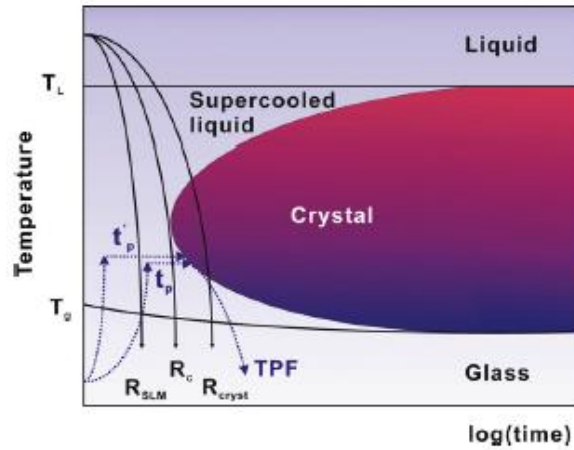


Figure 13: Schematic CCT diagram of metallic melt [36]

From Figure 13, lower cooling rates ( $R_{cryst}$  for example) will result in the melt partially or fully crystallising. The alloy system should have a low driving force for crystallisation in order to hinder the atomic rearrangements during cooling [28].  $R_{SLM}$  refers to the cooling rate derived by selective laser melting. TPF illustrates the temperature profile for thermoplastic forming [36].

The driving force of crystallisation is a thermodynamic property, while structural relaxation represents the system's kinetics [48]. Structural relaxation refers to the changes in physical properties of metals below the crystallisation temperature including viscosity, electrical resistivity and diffusivity while the structure remains amorphous [49]. This is particularly evident in the viscosity of the glass as it is directly related to the atomic mobility in this metastable structure. Through the annealing of metallic glass below the crystallisation temperature, the quenched-in disorder is lessened, leading to a lower atomic mobility, thereby influencing the viscosity [50].

According to Johari and Goldstein [51], the atomic and molecular configuration of liquids and glasses change in motions labelled as primary and secondary relaxations. A primary relaxation describes the major rearrangements represented in viscous flow. During cooling from the liquid phase, the glass transition is reached when the mobility decreases such as to impede these rearrangements. The material is a glass and there are no primary relaxations for temperatures below the glass transition. However, there exists the possibility for minor, localised and reversible rearrangements called secondary relaxations. Johari and Goldstein believed them to be a “near-universal feature of the glassy state” and those are suggested to be responsible for many mechanical responses during structural changes from annealing [22].

The observation of atomic transport properties and structural relaxation in amorphous metals prompted the idea of structural defects as a representation of free volume [52]. Although initially introduced by Batschinski in 1913 as the amount of extra space between molecules, Cohen and Turnbull in 1959 differentiated free volume from the excess volume [52], defining it as a dynamic quantity that can be divided into more parts without costing free energy [53]. In other words, it is an excess volume that can be redistributed freely without free-

energy change [54]. Therefore, the notion of free volume is correlated to defects in the structure. A defect is defined as “a site which the free volume exceeds a critical value” and according to this model, the atomic mobility, which is represented by the viscosity and diffusivity, is thought to be proportional to the concentration of defects [55]. It is further argued that the atomic transport is only possible when the atom is next to a free volume element that is larger than a critical size,  $v^*$ , estimated to be about 80% of the atomic volume [52]. Several research articles introduce variations of the following equation, Eq. 1, as an expression of viscosity,  $\eta$ , from Doolittle in 1951

$$\eta \sim \exp\left(b \frac{v^*}{\bar{v}_f(T)}\right) \quad \text{Eq. 1}$$

where  $b$  is a constant and  $\bar{v}_f(T)$  is the free volume at temperature  $T$ , the equilibrium free volume, and is experimentally determined to be linearly dependent on temperature [52]. When a liquid is rapidly quenched, the system would have no time to relax to its thermal metastable equilibrium and therefore the excess volume may be trapped in the glass and could be treated as structural defects [52].

A study on the characterisation of free volume in atomic models of metallic glasses published by Sietsma and Thijssse in 1995 [55] highlights the correlation between defects and atomic mobility. Three findings were discussed in the paper:

- 1) With support from numerous other experimental studies on diffusion in metallic glasses [56] [57], it is shown that the collective motions of atoms are found to take place rather than single-atom jumps. Therefore, the atomic mobility is thought to take place at holes. Holes are defined to be packing imperfections with a typical volume of 0.02 to 0.07 nm<sup>3</sup> [54].
- 2) Previous studies [58] on structural relaxation in palladium-nickel-phosphorus amorphous alloys have demonstrated that viscous flow and diffusion are governed by different defects. It was found that the concentration of defects for diffusion,  $c_d$ , is related to the concentration of defects for viscous flow,  $c_f$  by the following:  $c_d = \sqrt{c_f}$ . Furthermore, in the case of a random distribution of defects throughout the structure, this relationship implies that a diffusion defect is a “single entity” whereas viscous flow can occur when two of these defects interact.
- 3) Finally, during structural relaxation, the reduction of defects leads to a reduction of atomic mobility. It was found that the rate of reduction of defect concentration:  $\frac{-dc_d}{dt}$  is proportional to  $c_d c_f$ : the mobility needed to break up holes is supplied only if there are three holes interacting.

Differential Scanning Calorimetry (DSC) measures the heat flow in a material as a function of time and temperature. It is used to evaluate the glass transition, the devitrification temperature and heat of devitrification of metallic glasses [9]. It is believed that the glass transition, a kinetic phenomenon, is due to the free volume being out of equilibrium and continuously approaching a metastable equilibrium [59]. The rate of change of free volume in an amorphous metal is dependent on the actual free volume, which determines the glass transition

peak. Therefore, if two samples have the same initial free volume, they will have identical glass transition peaks [60].

### 2.3.3 Crystallisation from Amorphous Structure

The rapid quenching of the liquid metal prevents the nucleation of grains and the material maintains an amorphous structure. This causes the material to be in a metastable state where it is susceptible to changes in microstructure from external influences, such as heat or stress. Heating the amorphous metal will provide internal energy for the atoms to move into a more energetically favourable position – eventually crystalline. Therefore, the crystallisation of metallic glasses refers to the loss of an amorphous structure and crystal formation.

Applying stress to the material can also cause crystallisation. The absence of dislocations and slip systems in metallic glasses, although providing superior yield strength, also creates undesirable effects on plastic deformation. In crystalline metals, shear events occur throughout the structure, resulting in the plastic strain spreading throughout the material [61]. In metallic glasses however, the shear deformation is microscopically localised, giving the name “shear bands”. Figure 14 illustrates an example of these shear bands on (a) a Zr-based alloy and (b) characteristic “vein” like patterns in a PdSi glassy sample.

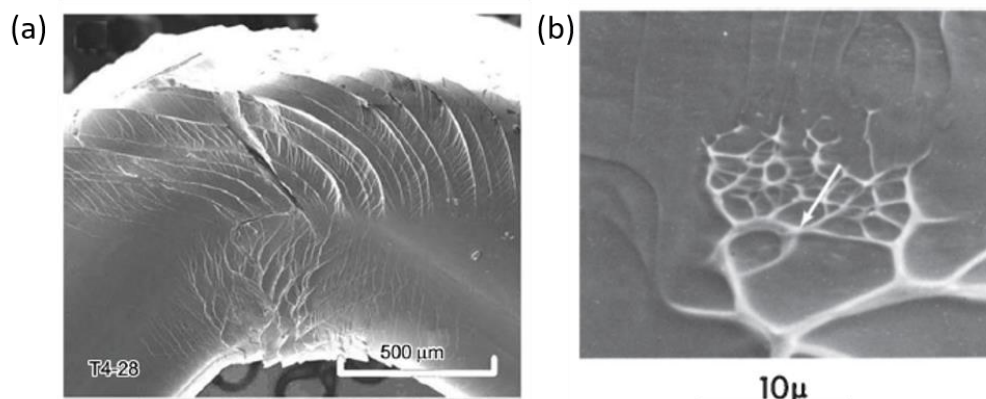


Figure 14: (a) Zr-based bulk metallic glass [27] and (b) vein pattern of Pd<sub>82</sub>Si<sub>12</sub> [61] exhibiting extensive plastic deformation

The mechanism through which the deformation-induced crystallisation occurs has been debated. Whereas plastic deformation in crystalline metals create additional defects (dislocations) and harden the material, deformation in amorphous metals increases the internal free volume and produces voids [62]. In these regions of free volume, the mechanical bonding to the surrounding is weaker, allowing inelastic relaxation through local atom rearrangements without affecting the surroundings. These areas are called “soft spots” [63] and can lead to the crystallisation of the structure.

It has been shown that room-temperature mechanical deformation of amorphous metals can induce crystallisation from structural instability [62]. Figure 15 illustrates this local crystallisation in a Ti<sub>40</sub>Zr<sub>29</sub>Cu<sub>9</sub>Ni<sub>8</sub>Be<sub>14</sub> amorphous alloy using high resolution transmission electron microscope (TEM).

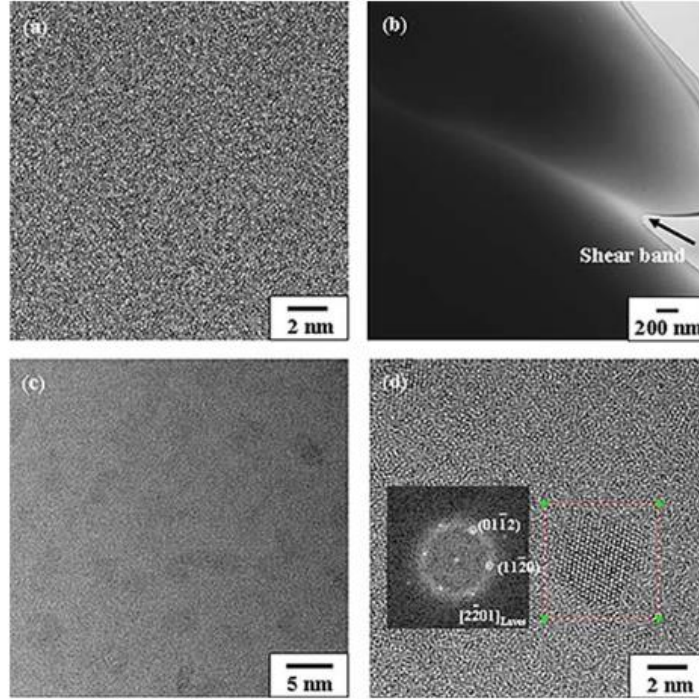


Figure 15: High resolution TEM micrographs obtained from  $\text{Ti}_{40}\text{Zr}_{29}\text{Cu}_9\text{Ni}_8\text{Be}_{14}$  metallic glass sample  
 (a) before deformation; (b) region containing shear band after deformation; (c) part of the area indicating presence of small crystallites; (d) area containing one of the crystals with inset showing Fourier transform of crystal [64].

As amorphous metals crystallise during heating, it has been associated that crystallisation occurs in shear bands due to localised heating. However, the increased atomic mobility found in shear bands could be from a temperature rise or from structural changes caused by the shear (generating free volume) [62]. Ultimately, the shear bands from plastic deformation result in fracture culminating to a more brittle material [65]; a factor that is to be taken into consideration when implementing amorphous metals in various applications.

Studies show that the crystallisation of amorphous metals cause drastic effects on mechanical [66] [67], magnetic [68] [69] and corrosion [70] [71] properties. There are several characterisation methods that can be used to determine the crystallinity of an amorphous structure. The most extensively used is X-ray diffraction (XRD), either employing the individual peaks in the XRD pattern or the entire pattern to define a relationship between the phase composition and the intensity of the peaks [72]. As can be seen from Figure 4 in Section 2.1, the XRD patterns of amorphous metals display broad signals as opposed to the sharp peaks present in crystalline patterns. Hermans and Weidinger [73] [74] developed a procedure for the quantification of crystallising of amorphous structures using XRD based on the crystalline intensity and amorphous intensity of samples with varying crystallinity percentages and computationally analyse the proportionality between the two. Transmission electron microscopy (TEM) can also be useful in determining crystalline phase with electron diffraction, but is complicated in procedure and analysis [72]. Electron backscatter diffraction (EBSD) is used for the determination of orientation and phase identification; the electron beam interacting with crystallographic planes within the sample [75]. Thermal analysis, such as differential scanning calorimetry (DSC) has also been

widely used. To calculate the crystallinity percentage of an amorphous sample, the specific heat of fusion for a partially crystalline sample is measured from the area under the exothermic peak in the heat flow curve and divided by specific heat of fusion for a fully crystalline sample [72]. The characterisation of amorphous metals structure after a potentially crystallising process is crucial to verify that the advantageous properties of metallic glasses are not lost.

## 2.4 Mechanical Properties

Relating back to the application of amorphous metals as cutting elements, an important quality required in shaving blades is a high hardness, in order for the material to be wear resistant and avoid deformation from repeated use. Hardness is the resistance of a material to plastic indentation. Additionally, a material's elasticity is characterised by the Young's modulus which describes the linear relationship between the applied stress and the resulting elastic strain. Traditionally, the values of elastic moduli are determined by two factors: the crystalline structure of the material and the interatomic bond strengths [30]. The comparison between amorphous metals and crystalline materials is illustrated in Figure 16, showing the Vickers hardness against the Young's modulus of different materials. The figure has been annotated to distinguish between the amorphous metal trend compared to the crystalline metals, highlighting stainless steels as a reference point.

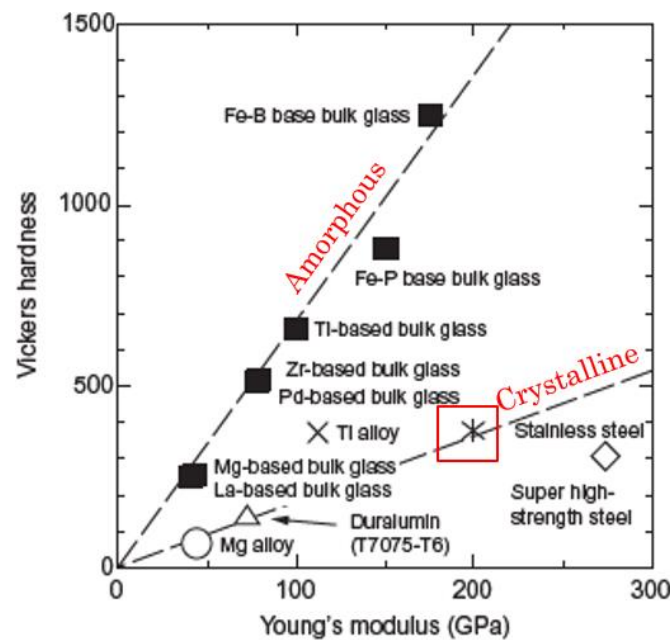


Figure 16: Comparison of Vickers hardness as a function of Young's modulus of metallic glasses and crystalline alloys.

Adapted from [76]

Amorphous metals have a higher hardness for comparable Young's modulus than crystalline metals. The effect of alloy composition on the microhardness was explored by Masumoto [77], shown in Figure 17 (a). The general trend describes an increase in the microhardness as the metalloid content increases.

Specifically, the hardness increases in the order of P, C, Si and B in the alloy systems, with Si-B systems being the most prominent [7].

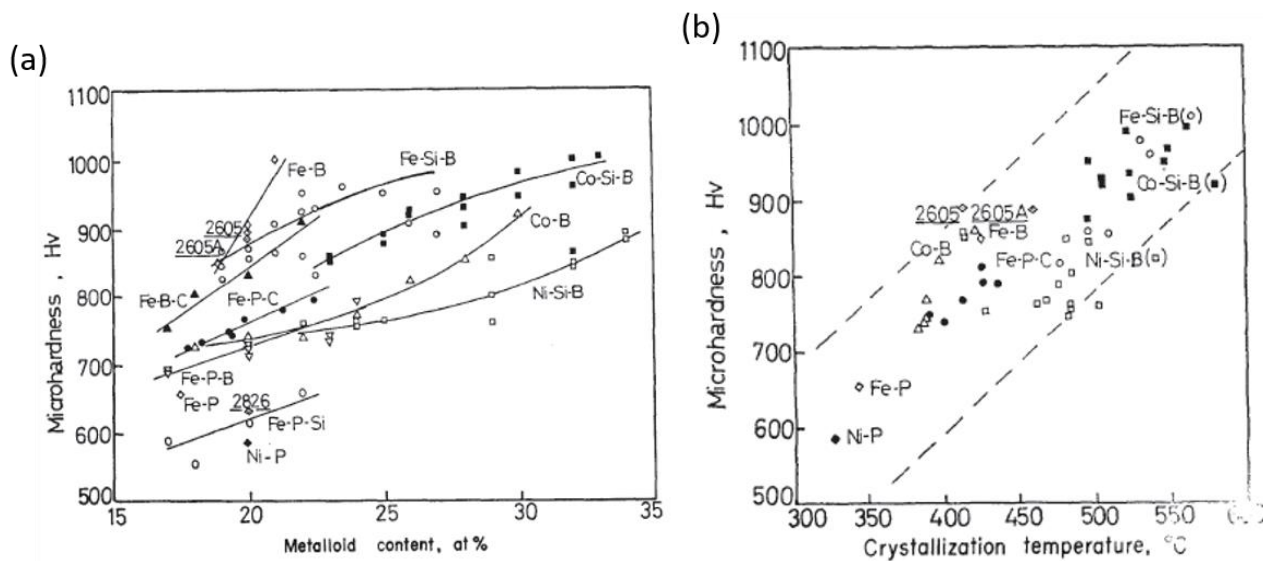


Figure 17: Correlation between microhardness and (a) metalloid content, (b) crystallisation temperatures of Fe-, Co- and Ni-base amorphous alloys with combinations of metalloids (C, P, B, Si) [77]

Furthermore, Figure 17 (b) includes the crystallisation temperature in correlation with microhardness which can be a measure of structural stability [77]. The similar trend can be seen in terms of the ranking of metalloids, although now the comparison between the base metal is more evident. Iron-base alloys are shown to have not only the highest hardness values in each metalloid system respectively but also a higher crystallisation temperature, implying its greater stability. Therefore, obtaining iron-based amorphous metals with a high metalloid content, specifically silicon and boron, would result in stronger and more stable shaving blades.

Another factor that demonstrates the improved mechanical properties of amorphous metals compared to that of crystalline is the high resilience [65]. Resilience measures the maximum energy stored elastically without damaging the material, and which is released upon unloading [78]. Figure 18 demonstrates the resilience against the loss coefficient between various materials (dark ellipses are amorphous alloys).

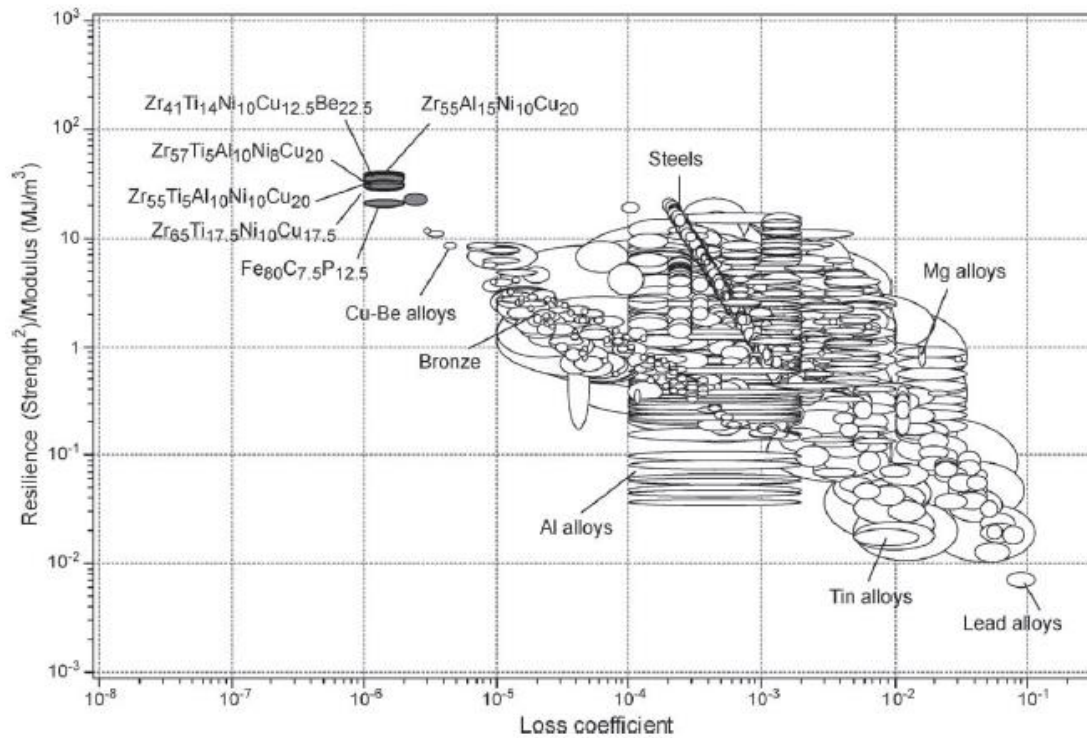


Figure 18: Resilience against loss coefficient of metals (amorphous shown in dark) [65]

The loss coefficient is a measure of the energy loss or mechanical damping in an elastic load cycle [65]. In this figure it can be seen that amorphous metals have superior resilience combined with a very low loss of energy compared to other metals. These qualities have made metallic glasses attractive for vibrating systems including gyroscopes and fast-acting springs [65].

## 2.5 Corrosion Resistance

The metal components of shavers are often in contact with not only water but also human sweat. The corrosion resistance is thereby important for the longevity of the shaver. Amorphous metals have an enhanced corrosion resistance. In general, as there are no structural defects in metallic glasses such as grain boundaries, dislocations or second-phase precipitates, as are present in crystalline materials, amorphous metals are more resistant to the corrosion that often initiates at these localised defects. As opposed to uniform corrosion, localised corrosion can be the most difficult to predict and often the most destructive.

Precipitates or second phases in crystalline metals are subject to galvanic corrosion. As the electrochemical potential of the two phases are different, for example martensite and ferrite in dual phase steels, this results in an increase in dissolution as a local anode (ferrite) and local cathode (martensite) created within the microstructure [79]. Although amorphous metals are composed of many different compositional elements, the microstructure is homogeneously single phased and is therefore theoretically not subjected to galvanic corrosion. However, defects and heterogeneities could be created during casting including gas bubbles, small crystallites forming or phase separation which could act as nucleation sites for pit initiation [47].

Gostin *et al.* [31] published a report on the comparison of the corrosion resistance of conventional steel and of bulk amorphous steel. The paper is aimed at comparing this behaviour of bulk glassy ( $\text{Fe}_{44.3}\text{Cr}_5\text{Co}_5\text{Mo}_{12.8}\text{Mn}_{11.2}\text{C}_{15.8}\text{B}_{5.9}\text{Y}_{1.5}$ ) alloy, with that of its crystalline counterpart as well as comparing to X210Cr12 steel. A series of potentiodynamic polarisation tests were performed on the three samples to investigate the free corrosion behaviour (absence of net electrical current) and anodic passivation behaviour. Figure 19 shows the potentiodynamic anodic polarisation curves in (a) sulfuric acid and (b) in sodium chloride.

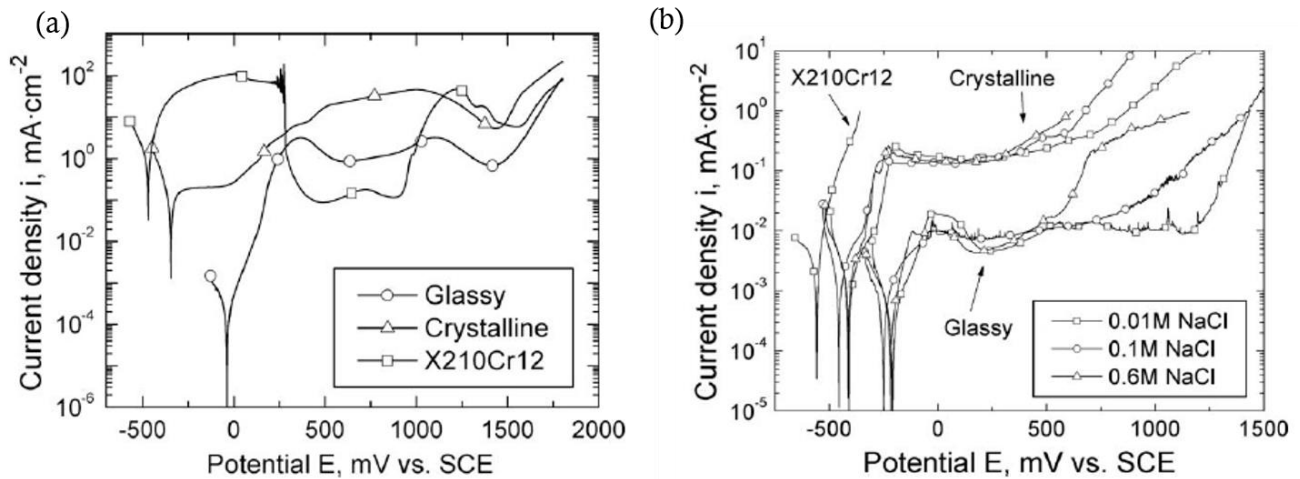


Figure 19: Potentiodynamic anodic polarisation curves of bulk glassy ( $\text{Fe}_{44.3}\text{Cr}_5\text{Co}_5\text{Mo}_{12.8}\text{Mn}_{11.2}\text{C}_{15.8}\text{B}_{5.9}\text{Y}_{1.5}$ ) alloy, of its crystalline counterpart and of conventional steel X210Cr12 in (a) 0.5 M  $\text{H}_2\text{SO}_4$  and (b) in neutral 0.001, 0.1 and 0.6 M NaCl electrolytes [31]

Figure 19 (a) shows that the glassy alloy has a much lower corrosion current density than the conventional steel sample. The high corrosion activity of the steel sample is due to the galvanic coupling between the  $(\text{Fe,Cr})_7\text{C}_3$  particles and the  $\text{Fe}(\text{Cr})$  matrix. Similarly, the crystalline counterpart of the glassy alloy also has a multiphase structure which results in galvanic coupling between the main phase ( $\text{M}_{23}(\text{B,C})_6$ ) and the interdendritic phase(s) [31], shown to imply a higher corrosion current density than for the single-phase glassy alloy. These potentiodynamic polarisation experiments carried out in NaCl are shown in Figure 19 (b). Compared to the glassy alloy, the crystalline counterpart alloy has less noble corrosion potentials and a higher current density, thereby exhibiting a poorer free corrosion behaviour [31]. Both the glassy and crystalline counterpart form a passive film (demonstrated by the plateau region), although it can be seen that the crystalline counterpart passive film is less protective than the glassy alloy as it exhibits more than a higher order of magnitude of the passive currents. The conventional stainless steel does not form a passive film even on the lowest concentration of NaCl and only a small polarisation increases the dissolution rate [31].

Additionally, research shows that the corrosion rate of amorphous metals is strongly dependent on the chemical composition of the alloy. Similar to crystalline metals, iron-based alloys with considerable concentrations of chromium and molybdenum have superior corrosion resistance [80]. However, the metalloid element in the amorphous alloy has an impactful influence on the corrosion rate. A study by Naka *et al.* [81] investigated the influence of the metalloid element and concentration on the corrosion rate of iron-chromium

amorphous alloys. It was stated that amorphous alloys containing phosphorus and carbon as metalloids exhibit higher corrosion resistance than alloys with silicon and boron. Furthermore, the study showed that when the major metalloid element consisting of 13 at% is changed from boron to phosphorus the corrosion rate of amorphous Fe-Cr alloys decreases by 2 or 3 orders of magnitude [81]. This is illustrated in Figure 20 where the Fe-Cr amorphous alloy contains 13 at% of boron as the major metalloid and 7 at% of X as a minor metalloid.

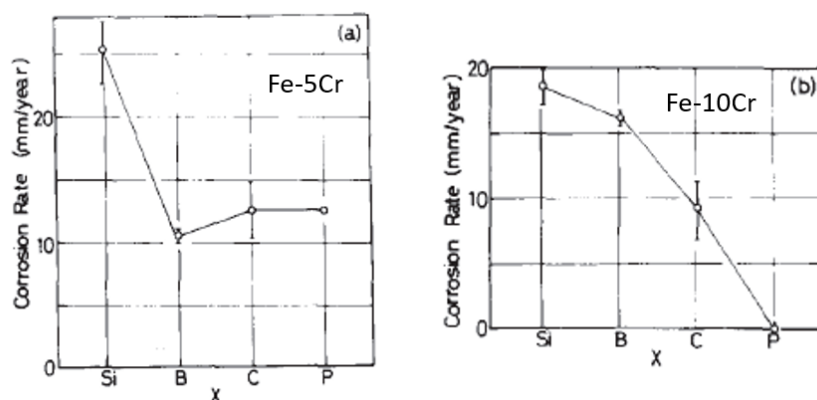


Figure 20: Effect of metalloid element X on corrosion rates of amorphous Fe-Cr-13B-7X alloys in 0.1N H<sub>2</sub>SO<sub>4</sub> at 30°C. Chromium content (a) 5 at% and (b) 10 at%. Adapted from [81]

With the generally low corrosion resistance of alloys with chromium content of 5 at%, the influence of the metalloid concentration is not as obvious as seen in Figure 20 (a). However, the effect of the minor metalloid is more distinguishable in Figure 20 (b) with an increasing order of corrosion resistance of alloys containing silicon, boron, carbon and phosphorus. This trend is similar to that observed in 3% NaCl solution with the order of alloys being boron, silicon, carbon and phosphorus [81]. The effect of metalloid concentration on corrosion behaviour has been further studied [82] as more amorphous metal alloys became commercially available. However, as developing technology allows for more complex amorphous metal compositions through various production methods, a comprehensive study on the corrosion resistance of a metallic glasses produced through different methods would offer information on the quality and homogeneity of the amorphous metal product.

Not only is it important that the metal passivates but also that the passive films are very stable and repassivate quickly if the film is damaged [83]. As stated, localised corrosion, such as pitting, is often the most detrimental. Research by Virtanen and Böhm [84] shows that the pit initiation rate is significantly lower and the tendency to repassivate is much higher for amorphous metals containing phosphorus due to the higher resistance against pit initiation as well as higher passivation ability [84]. Therefore, cutting elements made of amorphous metal alloys containing higher levels of phosphorus would have an increased lifetime owing to the superior corrosion resistance.

### 3. Materials and Methods

This section will introduce the sample materials of both amorphous metals and the reference materials that were used in this project. The background theory of the two methods of processing the metals into the cutting elements, photochemical machining and pulse/precision electrochemical machining, are explained as well as the physical application of these processes. Finally, the various analytical characterisation experiments are outlined and described.

#### 3.1 Materials

##### 3.1.1 Amorphous Metal Samples

The following table illustrates the nominal composition of each of the four amorphous metals, as well as the thicknesses that were available and the density of the material.

*Table 1: Dimensions, density, and compositions of amorphous metal samples*

	<b>MG-A</b>	<b>MG-B</b>	<b>MG-C</b>	<b>MG-D</b>
<b>Thickness Available [μm]</b>	25, 50, 75	25, 50, 75	35	38
<b>Density [g/cm<sup>3</sup>]</b>	7.70	7.82	7.51	7.57
<b>Nominal Composition (wt.%)</b>				
<b>Ni (Balance)</b>	70	82.4	43.6	42.5
<b>Fe</b>	≤ 1.0	3.0	35	32
<b>Cr</b>	21	7.0	11	16
<b>Si</b>	0.5	4.5	6.4	1.5
<b>P</b>	8.0	≤ 0.02	-	6.0
<b>B</b>	0.5	3.1	1.5	0.5
<b>Mo</b>	-	-	1.5	1.5
<b>Co</b>	≤ 1.0	≤ 0.1	-	-
<b>C</b>	≤ 0.1	≤ 0.06	≤ 0.1	-
<b>Cu</b>	-	-	1.0	-
<b>Al</b>	-	≤ 0.05	-	-
<b>S</b>	-	≤ 0.02	-	-
<b>Ti</b>	-	≤ 0.05	-	-
<b>Zr</b>	-	≤ 0.05	-	-
<b>Se</b>	-	≤ 0.005	-	-

As can be seen, all four amorphous metal samples are nickel based. However, samples MG-A and MG-B both contain the highest levels of nickel and lowest levels of iron. This is also represented in the available thickness of the alloy, as MG-C and MG-D contain high levels of iron and are only produced in a maximum thickness of 35 μm and 38 μm respectively.

An important factor that was recognised during this project was the difference in processability of the two sides of the amorphous metal. Due to the use of melt-spinning as the method of production, the side of the metallic glass that makes contact with the rotating copper drum is distinctly different to the opposing side, as shown in Figure 21. One side is a “glossy”, microscopically smooth surface with the presence of ribbon-like stripes running parallel along the coil while the other side is “matte” with a more constant surface roughness. The side which is processed against will be clearly stated.



Figure 21: Both sides of amorphous metals, (left) matte and (right) glossy

### 3.1.2 Reference Materials

Throughout the processing and characterisation of the amorphous metals, it was essential to have standard crystalline metals to compare to. Shaving blades are currently mainly composed of stainless steel. For research purposes, both martensitic and austenitic stainless steels have been used as reference materials. The austenitic stainless steel sample, labelled in this report as StAust, contains 0.120% C, 7% Ni and 16% Cr. Two martensitic stainless steel were used; one in a soft condition and one hardened through heat treatment. The soft martensitic stainless steel, labelled in this report as StMart, contains 0.33% C, 15.5% Cr and 0.8% Mo. The hardened martensitic stainless steel, labelled in this report as StMartHd, contains 0.53% C, 14% Cr and 1.0% Mo, and underwent austenitizing, quenching and tempering heat treatment. Furthermore, an additional reference material was a 99.8% Ni sheet that is used in specific elements of shavers. Each of these reference materials used were in a thickness of 60  $\mu\text{m}$ .

## 3.2 Processing Methods

There are numerous methods of processing raw metal coils into cutting elements. For this project two processes were explored, Photochemical Machining and Precision/Pulse Electrochemical Machining. The theory and application of both methods is described in this section.

### 3.2.1 Photochemical Machining (Etching)

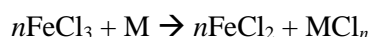
#### 3.2.1.1 Theory

Photochemical machining, often called etching, consists of sequential steps, each a critical prerequisite to the next. The overall concept of etching is the selective dissolution of material with an acid using a laminate to protect designated areas. Each step is defined below.

- 1) De-greasing and Pre-etching: The first step of the process is the sheet preparation carried out in conveyor belt chambers. The material is cut to a specified sheet size and goes through mechanical

cleaning with brushes and a degreasing solvent. The sheet is then exposed to a mild version of the chemical etchant, iron chloride, called pre-etching. This is intended to activate the surface for the subsequent step, lamination, as well as to remove any remaining contaminants. The sheet is then rinsed and dried fully.

- 2) Laminating: This is the application of the photoresist. The metal sheet is fitted between two rollers and a hot-roll lamination system applies the photoresist on both sides of the sheet. From this point it is essential that the process is done in a yellow safe-light room.
- 3) Illumination: The purpose of the illumination step is to selectively activate polymers within the photoresist. The UV light will cause the polymers to crosslink and harden. A designed pattern is created beforehand of which its black negative covers the surface of the metal sheet with the photoresist. Therefore, the UV light will expose and crosslink only the areas of the photoresist that are not covered by black pattern.
- 4) Developing: Following illumination, the metal sheet goes through another conveyor chamber to remove the unexposed (not-crosslinked) areas of the photoresist. This is done with spraying an alkaline solution and exposing the bare the metal and leaving the illuminated areas of the resist on the surface.
- 5) Etching: The metal sheet is sprayed through a conveyor chamber with iron chloride from the spray nozzles located at the bottom of the machine. This causes the bare metal to dissolve, although not impacting the areas still covered by the photoresist. The reaction involved in etching an  $n$ -valent metal (M) is as follows:



- 6) Stripping: This final step is the removal of the crosslinked photoresist remaining on the surface of the un-etched metal surface. Similar to the developing stage, this strong base however removes the illuminated photoresist. After another rinsing and drying step, the metal sheet has been chemically etched with the pattern of the original design.

### 3.2.1.2 Experimental Application

The established etching process in place is tailored to stainless steel sheets in dimensions of approximately 600 mm x 600 mm. The materials that were used for etching in this project were MG-B, MG-C, and the hardened martensitic stainless steel, StMartHd. These metals were in strips, 500 mm long x 22 mm wide and the thickness ranged from 0.06 mm (StMartHd), 0.05 mm (MG-B) and 0.035 mm (MG-C). Therefore, the overall process had to be adapted to the metal strips as opposed to metal sheets.

Primarily, for the steps involving a conveyor belt chamber, the sample strips were taped to the edge of a normal metal sheet,

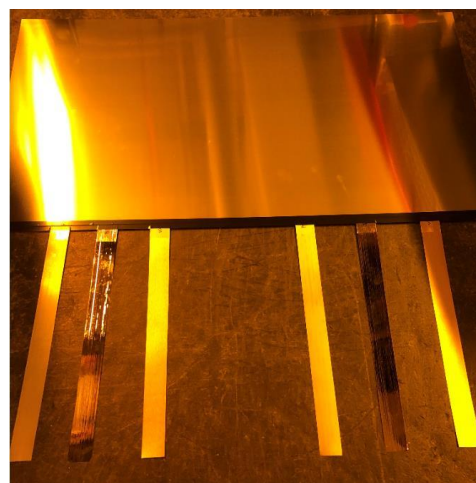


Figure 22: Amorphous metal strips taped to the edge of a standard metal sheet

thereby using it as a “drag-sheet” to pull the metal strips through the chambers, as shown in Figure 22. This was also the case for the lamination. However, the strips were individually illuminated.

Various etching parameters can be changed to achieve specifications. The traveling velocity (the speed of the sample through the etching chamber) [meter/second] influences the amount of metal dissolved, since the lower the speed, the more metal is etched away. Additionally, the pressure [liters] of the nozzle spray can be adjusted to have this similar effect. Since these trials were done in parallel to other business needs, the chemistry of the etchant was not changed.

### 3.2.2 Precision/Pulse Electrochemical Machining (PECM)

#### 3.2.2.1 Theory

As opposed to photochemical etching, the Precision/Pulse Electrochemical Machining utilises electrical pulses to machine metals into shape. It is based on the controlled anodic dissolution during the electrolysis process [85]. The PECM uses electrodes and a pulsating direct current to dissolve electrically conductive materials, as illustrated schematically in Figure 22. The main components are as follows:

Anode: positively polarised electrode and it is the workpiece being machined. This part sits in the flushing chamber.

Cathode: negatively polarised electrode. It is attached to the top of the machine and travels downwards in the z direction as it machines into the workpiece. It has the negative imprint of the desired geometry.

Electrolyte:  $\text{NaNO}_3$  is used and flows into the flushing chamber from connected tubes on the side as well as through the center of the cathode. Three important functions of the electrolyte are: it creates an electrical connection between cathode and anode; it constantly flushes and removes dissolved material; and continuously cools the process.

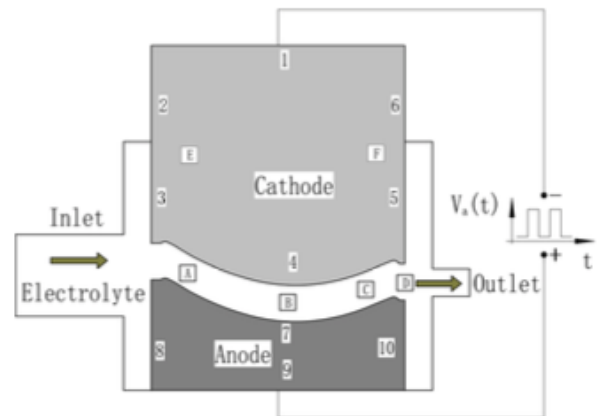


Figure 22: Schematic of the three elements in PECM: cathode, anode, and electrolyte [85]

The overall process of PECM involves the cathode moving downwards at a specified feeding velocity,  $V_f$ , with a set voltage to machine the workpiece into shape. The gap between the cathode and anode is a crucial factor to the process and should be kept as small as possible. The manufacturers of the PECM used in this project recommend a working gap of  $30\text{ }\mu\text{m}$ . In ideal conditions, the feeding velocity of the cathode would match the dissolution rate of the metal workpiece in order to maintain a constant working gap throughout. As the cathode travels down, it also oscillates a small margin in the z direction at a set frequency (commonly 50 Hz). During the lowest point of this oscillation (the cathode closest to the workpiece), a working voltage pulse is supplied across the two electrodes. The anodic electrochemical dissolution takes place in these short

pulse times, ranging from 1  $\mu$ s to 5 ms. This dissolution creates by-products such as sludge and gas bubbles which is then flushed away by the electrolyte as the cathode moves back to the higher point of the oscillation. If the dissolution rate of the workpiece is lower than the feeding velocity at which the cathode is moving down, in other words closing the gap between cathode and anode, there is a risk of the cathode and anode making contact. When this happens, it causes a short circuit and the entire process will stop.

The relation between the applied voltage and material dissolution can be interpreted by the current generated, following Ohm's Law:

$$V = I \cdot R \quad \text{Eq. 2}$$

The voltage,  $V$ , is programmed and kept constant and the current generated,  $I$ , is displayed on screen and measured. If the current is seen to increase, this would indicate a decrease in resistance,  $R$ , which is a representation of the working gap between cathode and anode. A small resistance implies a shortened working gap [PG1]. The P can refer to Pulse because of the pulse of electricity or to Precision due to very low tolerance and high precision in machining.

#### *3.2.2.2 Experimental Application*

As opposed to the etching, the PECM process did not have to be as drastically adapted to the dimensions of the sample metals. Each of the amorphous metals (MG-A,B,C,D) as well as the three stainless steels, StAust, StMart, and the hardened martensitic stainless steel, StMartHd, were machined with PECM. This allowed for direct comparison between the etching and PECM process on the same material (MG-B, MG-C, StMartHd). However, one important factor that needed to be minimised is the sample buckling. As the cathode oscillates at the set frequency, the motion causes the risk of the thin metal to lift in the middle and buckle upwards. If this happens, there is a strong likelihood that the metal will make contact with the cathode, causing the short circuit. During the normal business process, magnets below the base of the sample holder pull the metal down and eliminate this risk. However, as the amorphous metal samples are not magnetic, double sided tape was used to fix the sample down.

As described, the PECM has specific parameters that can be controlled during the process. The voltage [Volts] will determine the potential applied and the pulse [milliseconds] will control for how long this voltage is emitted throughout the oscillating intervals. The feeding velocity [meters/second] will define how fast the cathode travels in the downward direction. This feeding velocity and the voltage/pulse need to be well balanced to ideally remove material at the same rate the cathode is travelling down in order to maintain a working gap of 30  $\mu$ m. This process is defined by the absolute distance [meters] programmed outlining the overall trajectory the cathode moves.

### 3.3 Material Characterisation

The second aspect to the project is the analytical characterisation of the materials. Essential properties of cutting elements in shavers include high hardness values, corrosion resistance and a sharp cutting edge. Amorphous metals have shown in literature to be harder than stainless steels and have an improved corrosion resistance due to the lack of grain boundaries and second phases. However, it is important that the beneficial properties of amorphous metals are not affected from processing. This relates to the second research question: Are the advantageous amorphous metal properties maintained after processing? The characterisation experiments included in this project are thermal analysis, hardness testing, corrosion resistance and the rate of nickel released in artificial skin sweat. This section introduces the different characterisation methods used in the project as well as the procedure.

#### 3.3.1 Thermal Analysis

##### 3.3.1.1 Background

The thermal analysis of metallic glasses can give indications of the material's thermal stability as well as changes in the microstructure. As described, advanced mechanical and electrochemical properties arise from an amorphous structure. External stresses such as mechanical deformation or applied heat can cause undesired crystallisation and affect these properties. It was hypothesised that the processing could potentially cause crystallisation in the amorphous metal samples.

Like common glasses, metallic glasses have glass transitions, and most will crystallise almost immediately after this transition point [86]. Therefore, knowing this transition temperature is important for material application to maintain within its operating conditions. Differential Scanning Calorimetry (DSC) measures the heat flow in materials as a function of time and temperature [86] and can indicate not only the glass transition temperature ( $T_g$ ), but also crystallisation temperature ( $T_x$ ), and liquidus melting temperature ( $T_l$ ) [87].

##### 3.3.1.2 Experimental Application

###### Sample Preparation:

The amorphous metal sample was cleaned and cut into small pieces, weighing between 3 to 5 mg. These weighed fragments were placed in a crucible and sealed with a press. The lid of the crucible was punctured to release pressure during the heating process. Two replicates of each analysis were prepared. For comparison purposes, two stainless steel references were also measured, StAust and StMart.

###### DSC:

The differential scanning calorimeter detects the heat flow rate between two crucibles containing the material under investigation and a reference sample. Figure 23 illustrates the DSC principle of an amorphous sample and its typical DSC scan.

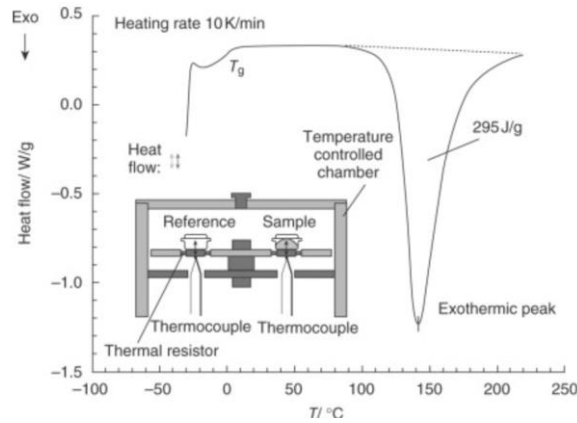


Figure 23: DSC heat flow against temperature of epoxy resin showing crosslinking. Insert: measuring principle of DSC [88]

First a baseline scan is recorded with both crucibles empty, thereby measuring any bias inherent in the system. The next step is the reference test, in which a sample with a well-defined specific heat capacity is tested as a comparison [89]. Finally, the experimental sample is tested. The DSC equipment used was Netzsch DSC 204 F1 Phoenix, serial No. 240-11-051L with a temperature program of initial temperature 30°C for 2 minutes, heating with 10 K/min to 600°C.

### 3.3.2 Hardness

#### 3.3.2.1 Background

The hardness of a material is the resistance to plastic indentation. This value is roughly proportional to the strength of a metal and is therefore useful during the selection of a material for specific application. Metals in shavers should have a high hardness value in order to be wear resistant and avoid deformation from repeated use. Various forms of hardness testing exist and can be classified based on the magnitude of the indentation load and indenter; macrohardness ( $> 1$  kgf), microhardness ( $< 1$  kgf) and nanohardness (as small as 0.1 mN) [90].

The hardness tester used in this project was the microhardness testing, specifically the Vickers Indenter. This is a square base pyramid indentation as shown in Figure 24. This hardness value is the load supported by the unit area of the indentation, expressed in kilograms force per square millimeter (kgf/mm<sup>2</sup>) [90].

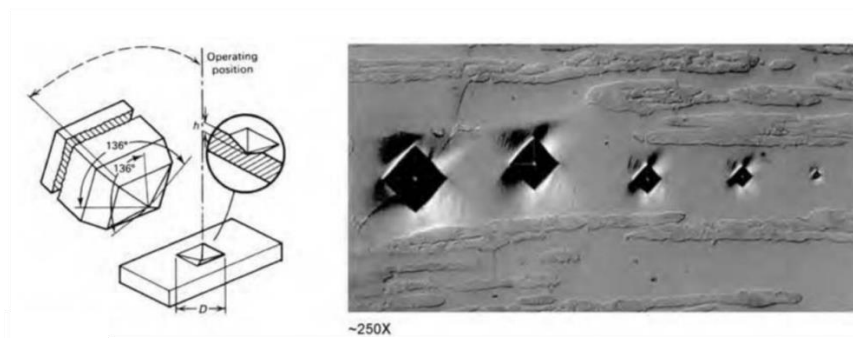


Figure 15: Vickers Microhardness Indentation of a ferritic-martensitic high carbon stainless steel [90]

### *3.3.2.2 Experimental Application*

#### Sample Preparation:

The sample preparation for the hardness measurements is the embedding of the cross section of the material sample. Prior to the embedding process, the samples were cleaned with isopropanol in the ultrasonic bath for 5 minutes to remove contaminants that would cause difficulty in the epoxy bonding. The samples were then fixed into a holder with specific orientation; for each material both the parallel and perpendicular to the rolling direction (the direction of melt spinning) were measured.

In a plastic cup, 15 mL of the Epoxy-Resin and 2 mL of the Epoxy-Fix Hardener were mixed and stirred with a wooden stick for 90 seconds and poured into the sample holder. To ensure a homogenous spread of the epoxy and eliminate bubbles present, the samples were put in a desiccator with a vacuum pump and left for one minute with reduced pressure. Finally, 24 hours are needed for the epoxy to harden.

A hammer and wooden stick were used to free the hardened resin containing the samples from the holder. Using sequential grinding paper with decreasing grain size, the samples were grinded with constant water running:

P320 | P600 | P800 | P1000 | P1200 | P2000 | P4000 – the coarsest grinding paper (P320) was also used to remove the back skin (opposite side of the sample embedding) to smoothen and flatten out the back surface.

After the final P4000 grinding, the samples were cleaned with distilled water in the ultrasonic bath for 15 minutes. Using a semi-automated grinding machine, the samples were polished following a similar procedure to the grinding by reducing the grain size of the polishing plate:

6  $\mu\text{m}$  | 3  $\mu\text{m}$  | 1  $\mu\text{m}$  – with a set applied force of 25 N.

The final polishing step is a chemical cleaning for a glossy surface using a silica colloidal suspension. The result of this process is the cross-section of the material sample embedded in resin of which hardness measurements can be made.

#### Hardness Measurements

The hardness instrument is a microindenter, Helmut Fischer Company, type H100 SMC. The sample is fitted in the holder with the cross sections facing up. A built-in microscope can guide and specify the area of indentation. It then moves across and begins the Vickers hardness indentation. The load used for the samples was equivalent to HV0.01, a lower load due to the small thicknesses of the samples. Each sample was measured 8 to 10 times making sure that the subsequent measurement area was spaced more than three times the diameter of the diagonal of the previous indentation. Using a light microscope, the two diagonals of the pyramid indentations of each sample were measured and the hardness values calculated.

### 3.3.3 Corrosion Resistance

#### 3.3.3.1 Background

Corrosion resistance is crucial to the longevity of a metal. Specifically for shaving blades, the consequence of corrosion is the weakening of the blade structure and could lead to a possible sudden breakage of the blade. Additionally, macroscopic holes on the surface of the cutting area of the element can cause an uncomfortable shaving process.

Shaving blades are exposed to human sweat, mainly composed of water, organic acids and chlorides. The chlorides in the sweat are primarily responsible for the localised corrosion of stainless steel cutting elements. Chloride-induced corrosion attacks occur preferably at grain boundaries of the microstructure.

Various electrochemical techniques are used in predicting the potential lifetime of metals in specific environments. In this project, three main methods were used, each describing a different aspect of the corrosion resistance of amorphous metals compared to the reference metals.

#### Open Circuit Potential

The open circuit potential is the equilibrium potential of a metal in a solution, with no applied potential to the system, measured as a function of time. It is an indication of the corrosion resistance and stability of the metal in the chemical. More noble elements have a greater corrosion resistance (positive potential).

#### Potentiodynamic Polarisation Scans

The potentiodynamic polarisation technique is used to determine the potential region at which a metal or alloy creates a passive layer when exposed to a specific environment. It analyses both the ability of the material to create this spontaneous passive layer as well as the critical current density required for the passivation. This method estimates the corrosion active region, the onset of passivation, the critical current density, the primary passive potential and the current and voltage span of the passive region [91].

#### Double Loop Electrochemical Potentiokinetic Reactivation

Chromium depletion along the grain boundaries of stainless steels is a phenomenon known as sensitisation and is due to the precipitation of chromium carbides [92]. These zones are therefore not as corrosion resistant, making the stainless steel more prone to intergranular corrosion. The Single and Double Loop Electrochemical Potentiokinetic Reactivation techniques (SL-EPR and DL-EPR) are potentiodynamic scans that assess the degree of sensitisation [92]. The Double Loop-EPR was used in the project. The sample is initially stabilised at an open circuit potential (around -0.5V). A potential is then applied to the system, up to +0.8V, and then back to the original potential. The peak current of the anodic polarisation (first scan)  $I_a$ , is compared to the peak current on the reverse scan,  $I_r$ . A typical DL-EPR scan is schematically shown in Figure 25.

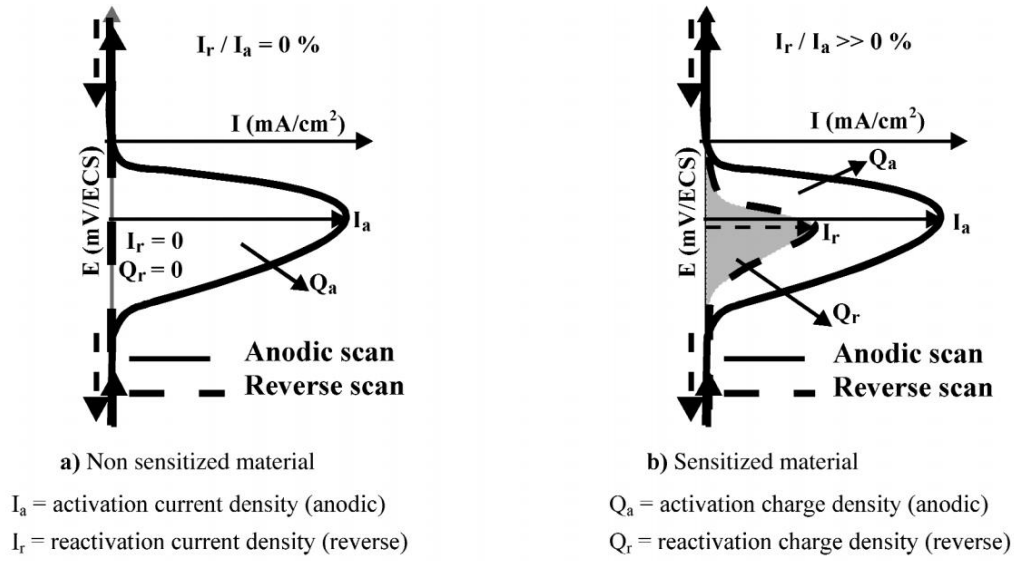


Figure 25: Principle of Double Loop-EPR technique on (a) non sensitised material and (b) sensitised material [93]

The current on the return scan is assumed to be primarily due to the reactivation of the chromium depleted grain boundaries. Therefore, the ratio of  $I_r : I_a$  is used to measure the degree of sensitisation and intergranular corrosion [93].

### 3.3.3.2 Experimental Application

The samples are stamped into a coin shape with a diameter of 15.6 mm and cleaned in isopropanol in the ultrasonic bath for 5 minutes. Figure 26 is a live image of the experimental set up.

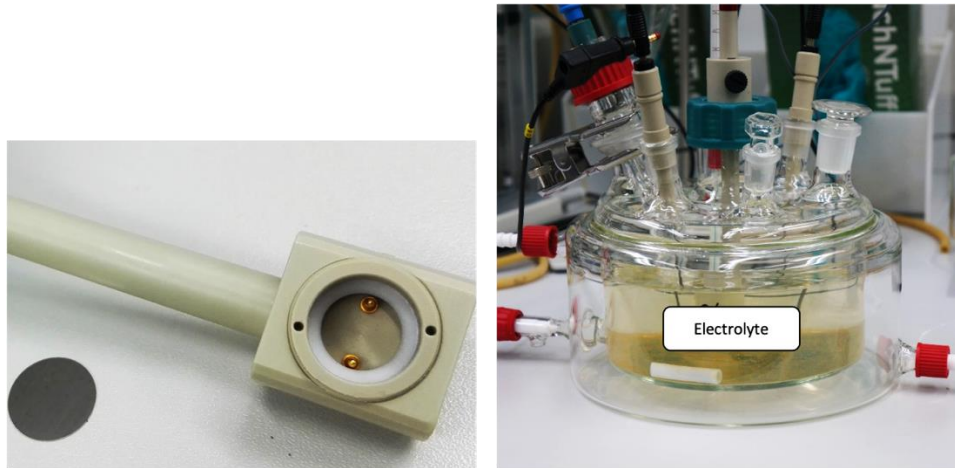


Figure 26: Corrosion experiment apparatus (a) sample in coin shape and working electrode fixture (b) Electrochemical cell [Live image by PG2]

The three different corrosion experiments were conducted with the same apparatus using an electrochemical cell. This is composed of the cell body and three electrodes. The cell body contains the environment of the system and controls the operating parameters such as temperature, pH, etc. The three electrodes include the working, counter and reference electrode. The working electrode is the material under investigation. The

reference electrode provides a standard “reference” against which the applied potential can be measured [92], in this case a silver/silver-chloride. The counter electrode is used to provide an applied current and is made of highly corrosion resistant material, such as platinum.

The open circuit potential and polarisation experiments were carried out in an artificial skin sweat solution to understand how the material would resist to repeated human contact. The Double Loop-EPR was measured in a solution containing 30 mmol/L of  $\text{H}_2\text{SO}_4$  and 1 mmol/L of KSCN.

### 3.3.4 Nickel Release

#### 3.3.4.1 Background

The purpose of this experiment is to analyse the rate of nickel release in the material when exposed to an artificial skin sweat. This gives an indication of how much nickel in the alloy will be released during the shaving experience.

A common method of detecting trace levels of elements is through Inductively Coupled Plasma-Optical Emission Spectrometry (ICP-OES), illustrated in Figure 27.

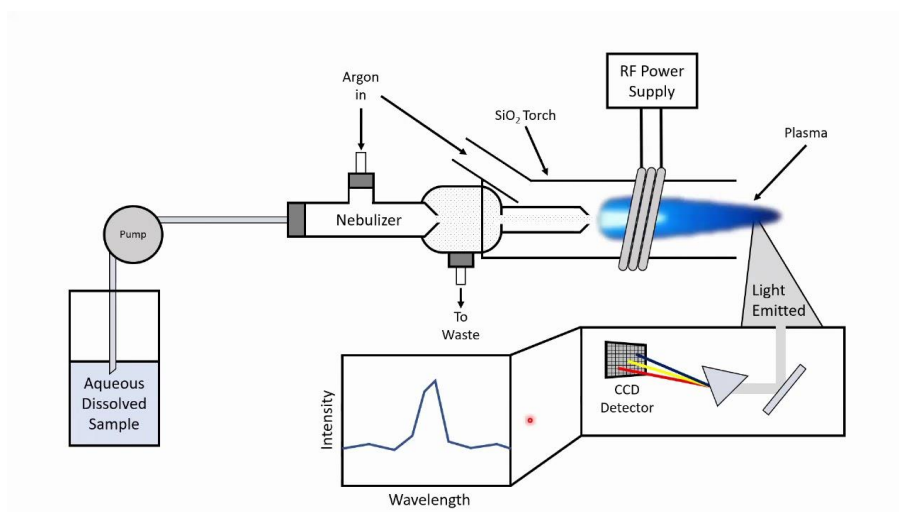


Figure 27: Schematic of ICP-OES [94]

The optical emission spectrometry is based on the characteristic of the radiation emitted by the ions, involving three steps [95]:

1. The sample is vaporized, generating a gas phase. The atoms are excited and the optical radiation is emitted. This is done through the inductively coupled plasma, a partially ionised gas in a high-frequency electromagnetic field when current flows through the induction coil. The generated flame discharge (plasma torch) reaches temperatures of around 10,000 K.
2. The compound radiation emitted by the optical source is dispersed according to the wavelength by the monochromator, thereby forming a spectrum.

3. Finally, the wavelength and intensity of the spectral lines are detected by the detector. The element detection depends on the wavelength detected and the intensity is proportional to the signal intensity.

#### *3.3.4.2 Experimental Application*

##### Sample Preparation:

The solution created represents an artificial human sweat solution. This is composed of urea, sodium chloride, and lactic acid mixed in distilled water. The pH of the solution was controlled at 6.5.

For direct comparison, the material samples were stamped into a coin shape, 15 mm in diameter. After being cleaned with isopropanol in the ultrasonic bath, each sample was submerged in 10 mL of the artificial sweat solution. Kept in a plastic vial, the samples were stored for 7 days.

##### Analysis:

Following the week, the samples were removed from the solution. The levels of nickel released in the solution were analysed through Inductively Coupled Plasma-Optical Emission Spectrometry by an expert [PG3].

## 4. Results

### 4.1 Processing

Both the etching and PECM processing experiments performed in this project were a proof of principle, designed to verify the general processability of the material. Therefore, meeting design specifications and optimisations were not the objective. The main aspect was the adjustment of parameters to obtain sharp cutting edges.

#### 4.1.1 Photochemical Machining (Etching)

##### 4.1.1.1 Processability with respect to amorphous compositions

The first aspect to the processability of amorphous metals through photochemical machining is to verify whether or not the metallic glass can dissolve in the etchant, an iron chloride solution. This was confirmed with a beaker experiment prior to running the full etching line process. The mass loss of each amorphous metal was measured with respect to time to evaluate the dissolvability in iron chloride and compare to the reference stainless steels.

The experimental set up is illustrated in the schematic in Figure 28. The sample was cut into a coin shape of 15.6 mm in diameter in order to maintain a constant surface area exposed to the etchant. Each sample was weighed and recorded (initial mass). One side of the coin was placed against a tape and attached to the end of a glass rod and immersed in the solution. A range of immersion times were measured: 1 minute up to 6 minutes. After each determined time in the solution, the coin was removed from the etchant and placed in water immediately to terminate the reaction. After cleaning, the sample is weighed again (final mass). The iron chloride solution was maintained at 60°C. Both the glossy and matte side of the amorphous metals were measured and compared to the martensitic stainless steel, StMart.

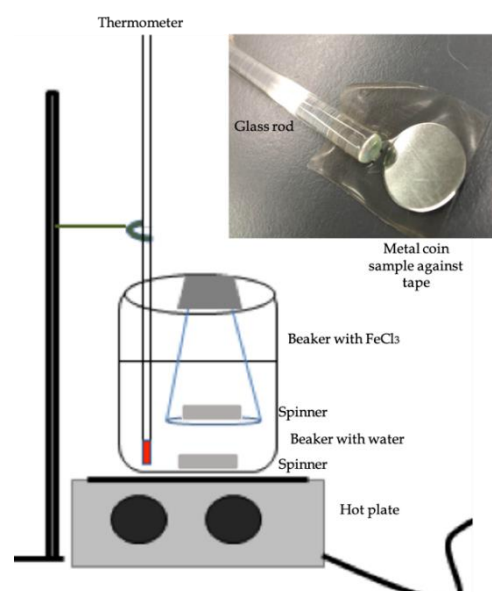


Figure 28: Schematic of mass loss experiment

From the mass measured after each minute, the rate of mass loss was calculated. Table 2 summarises the average mass loss rate in milligram per minute and standard deviation.

Table 2: Average mass loss of materials in iron chloride

Material	Average Mass Loss Rate [mg/min]
MG-A	No Mass Loss Detected
MG-B: Glossy Side	$4.2 \pm 0.7$
MG-B: Matte Side	$5.5 \pm 0.2$
MG-C: Glossy Side	$4.7 \pm 0.7$
MG-C: Matte Side	$5.2 \pm 0.3$
MG-D	No Mass Loss Detected
StMart	$7.2 \pm 1.4$

The first point of observation is that not all amorphous metals dissolve in the iron chloride solution; MG-A and MG-D showed no detectable significant change in mass after being exposed to the etchant. This may be because these two compositions contain high levels of chromium (21% in MG-A and 16% in MG-D) thereby exhibiting higher degree of corrosion resistance. Additionally, it has been demonstrated in literature [81] that phosphorus also enhances corrosion resistance (8.0% in MG-A and 6.0% in MG-D). By comparison, MG-B and MG-C have 7.0% and 11% chromium respectively and negligible (less than 0.02% in MG-B) to no levels of phosphorus.

The samples were also observed with the scanning electron microscope, SEM. Figure 29 is comprised of the SEM images of samples MG-B and MG-C at different magnifications.

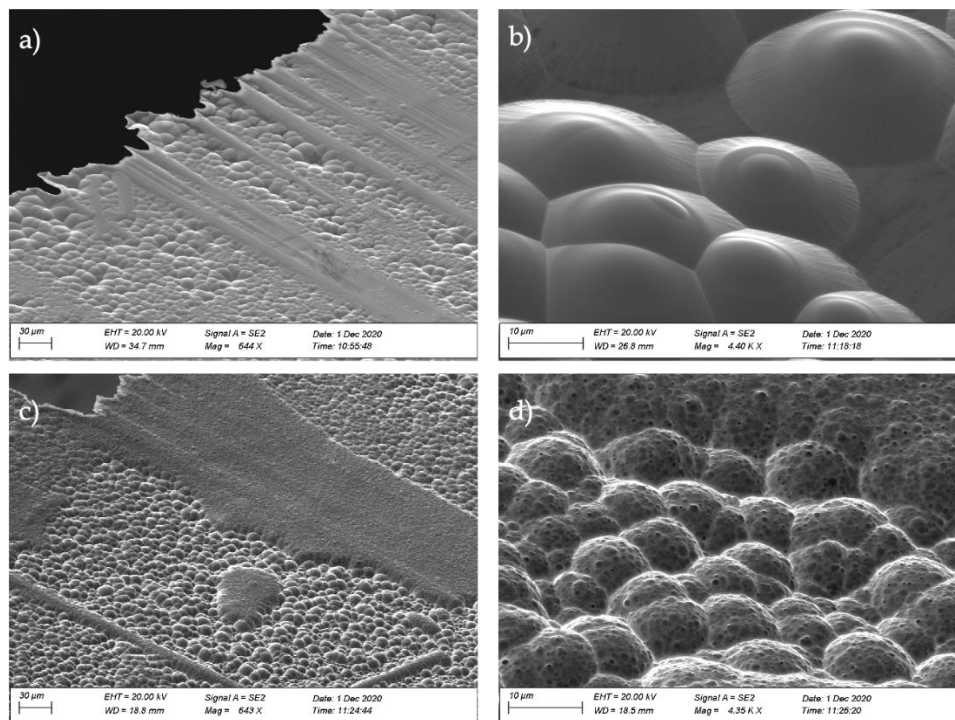


Figure 29: SEM images of the glossy side amorphous metals after 6 minutes in iron chloride: (a,b) MG-B and (c,d) MG-C

Both materials show the presence of “dome-like domains” on the surface. While the MG-B sample has what appears to be “hard shell-like” spheres, MG-C has more texture on the spheres with darker spots distributed around. However, both amorphous metals have sections between these domains of clear area. Since both samples were produced by the same manufacturing company through melt spinning, these differences in domain textures could be attributed to the composition of the material. Further investigation into these surfaces could be explored through analysing the impact of different solutions on the solubility and resulting surface.

Between the glossy and matte side of MG-B and MG-C, it can be seen that for both cases the matte side loses mass on average at a higher rate than the glossy side. Additionally, either side of the metallic glass samples dissolves at a lower rate than the martensitic stainless steel. This will influence the parameters required for the

experiments in the real etching line. Although it is not clear why this is the case, it is most likely due to the method of producing amorphous metals (melt spinning) creating two different surface textures.

Relating back to the first research question of understanding the influence of the amorphous metal composition and the processability, this experiment has made it clear that not all amorphous metals can be etched. Moving forward with the etching experiments, only MG-B and MG-C will be tested.

#### 4.1.1.2 Etching Trials

From the beaker mass loss experiment, only MG-B and MG-C were used in the etching trials. Additionally, it was seen that the glossy and matte side lose mass at different rates. Since the etching is sprayed from below, the orientation of the metallic glass becomes important. Therefore, for each trial it can be said that five materials were used: the reference stainless steel StMartHd (60  $\mu\text{m}$  thick), MG-B-Glossy side, MG-B-Matte side (50  $\mu\text{m}$  thick), MG-C-Glossy side and MG-C-Matte side (35  $\mu\text{m}$  thick). Due to similarities in thickness between the StMartHd and MG-B samples, these were carried out simultaneously and MG-C separately. These experiments were performed with the aid of two technicians [PG4] [PG5].

The first aspect to the etching process is the sheet preparation. This involves a mechanical cleaning of the surface to remove grease and other impurities followed by a spraying of the pre-etchant. The reference material, StMartHd, as well as the amorphous metal samples MG-B and MG-C went through the same sheet preparation. This was also the case for the lamination and illumination, all materials had the same design geometry of the final cutting part printed on the laminate.

The samples after the sheet preparation were analysed with the SEM to understand the impact of the pre-etchant on the surface of the metal. Figure 30 shows the surface of the materials.

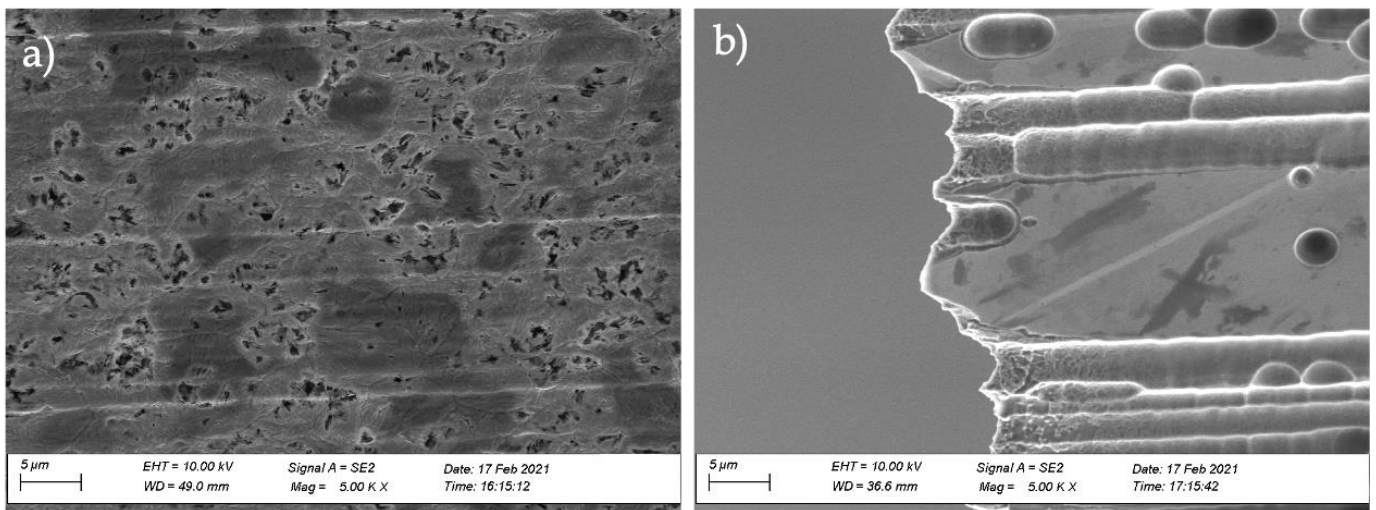


Figure 3016: SEM images after pre-etching of (a) StMartHd and (b) MG-B

As can be seen, both the crystalline and amorphous metal have an impact from the iron chloride pre-etchant. On the StMartHd, this type of attack could be due to the chlorine ions targeting the grain boundaries of

the structure. The surface of the MG-B sample shows the same effect that was seen in the beaker mass loss experiment. These imperfections could hinder the adhesion between the damaged surface and the photoresist.

The first etching trial was carried out using the known etching parameters of the StMartHd stainless steel of 60  $\mu\text{m}$ . For direct comparison, this material as well as MG-B-Glossy side and MG-B-Matte side were run at the same time. Since the etching parameters were specified for the StMartHd sample, this material was etched to the design specifications. However, the two MG-B samples were almost completely etched through, sample MG-B-Matte side more so than MG-B-Glossy side. It was then clear that even although the MG-B sample dissolves slowly in the beaker mass loss experiment, the difference in thickness is also an impactful factor.

In the next experiment the speed was increased so that the amorphous metal does not spend as long exposed to the etching solution. This was repeated until each material side reached acceptable specifications. An interesting conclusion that arose from these trials was regardless of the parameters, the cutting edges of the amorphous metal MG-B etching against the glossy side were not as smooth as etching against the matte side. This is illustrated in the light microscope images shown in Figure 31.

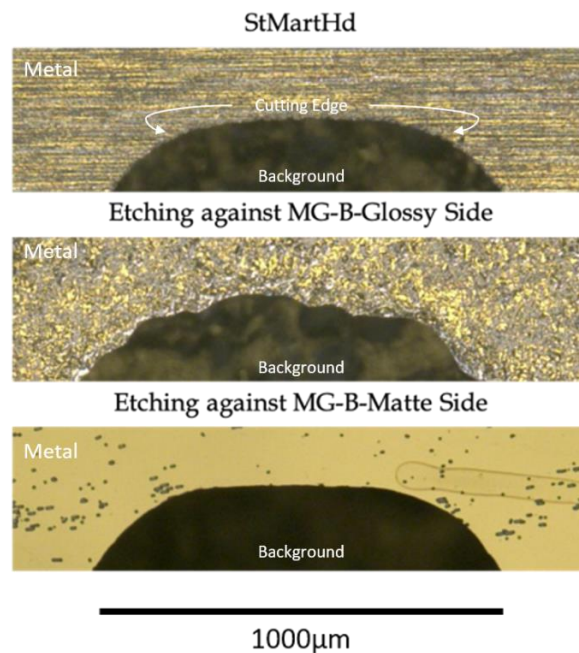


Figure 31: Light microscope images of the cutting edges of StMartHd, MG-B-Glossy side and MG-B-Matte side. Note: the yellow tone of the surface is due to the reflection of the light from the microscope. Annotations indicating the metal sample and the background surface of the light microscope plate. First image indicates the cutting edge of the material, applicable to all three images.

As can be seen, the cutting edges of the MG-B-Glossy side are rough and uneven. This could result in a more uncomfortable shaving experience as opposed to the StMartHd and MG-B-Matte side edges. Therefore, it was concluded that should amorphous metals be processed through etching, it is the matte side that should be etched against.

Comparing the resulting cutting elements of the standard martensitic stainless steel to the amorphous metal, see the SEM images in Figure 32 of the cutting edge in Figure 31.

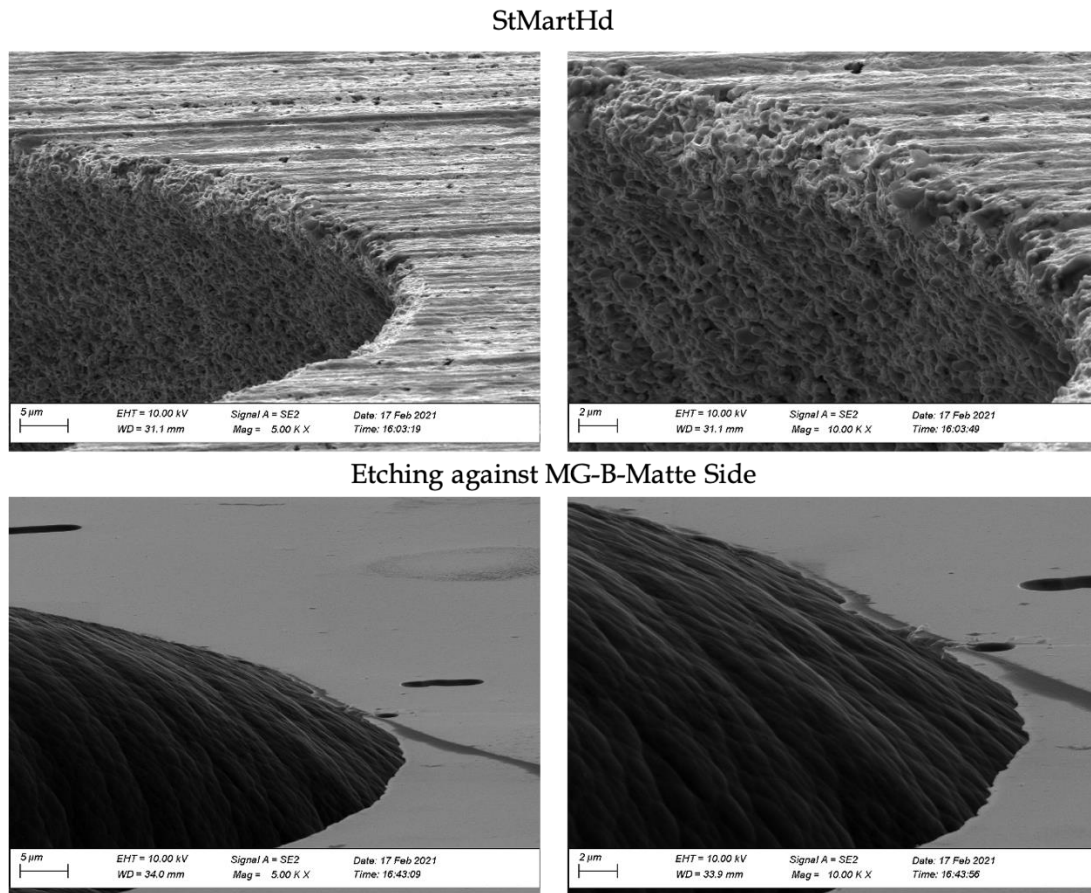


Figure 32: SEM images of the cutting edges of StMartHd and MG-B-Matte side. Images taken by [PG6].

The SEM images show the cutting edges of StMartHd and MG-B-Matte side of the samples with the most successful parameters each. A noticeable difference between the two materials is the edges of the cutting tip. The MG-B sample not only has a much finer and smaller tip but is more homogenous along the edge. The StMartHd sample has more of a bread-knife-like structure. This could suggest a more efficient cutting performance, with fewer “pass-overs” of the shaver against the face required.

The etching trials were also performed on amorphous metal MG-C, glossy and matte side, in a thickness of 35  $\mu\text{m}$ . The overall shape of the design that was illuminated on the laminate was etched successfully. However, due to the much smaller thickness of this sample, the overall application of this material in the shaver is more challenging. Nevertheless, the same conclusion of etching against the matte side yielded straighter cutting edges than etching against the glossy, as shown in Figure 33.

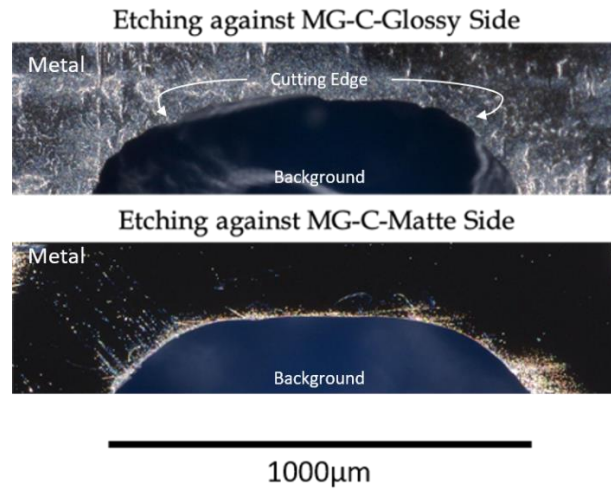


Figure 33: Light microscope images of MG-C of glossy and matte side. Annotations indicating the metal sample and the background surface of the light microscope plate. First image indicates the cutting edge of the material, applicable to all second image.

#### 4.1.1.3 Challenges and Possible Improvements

There are several challenges associated with photochemical machining on stainless steels that were also occurring for amorphous metals. Due to the aggressive nature of the pre-etchant, surface attacks on both the StMartHd and metallic glasses MG-B and MG-C were seen. Additionally, a poor adhesion between the metal and the photoresist can result in the etchant to come between the laminate and the covered surface.

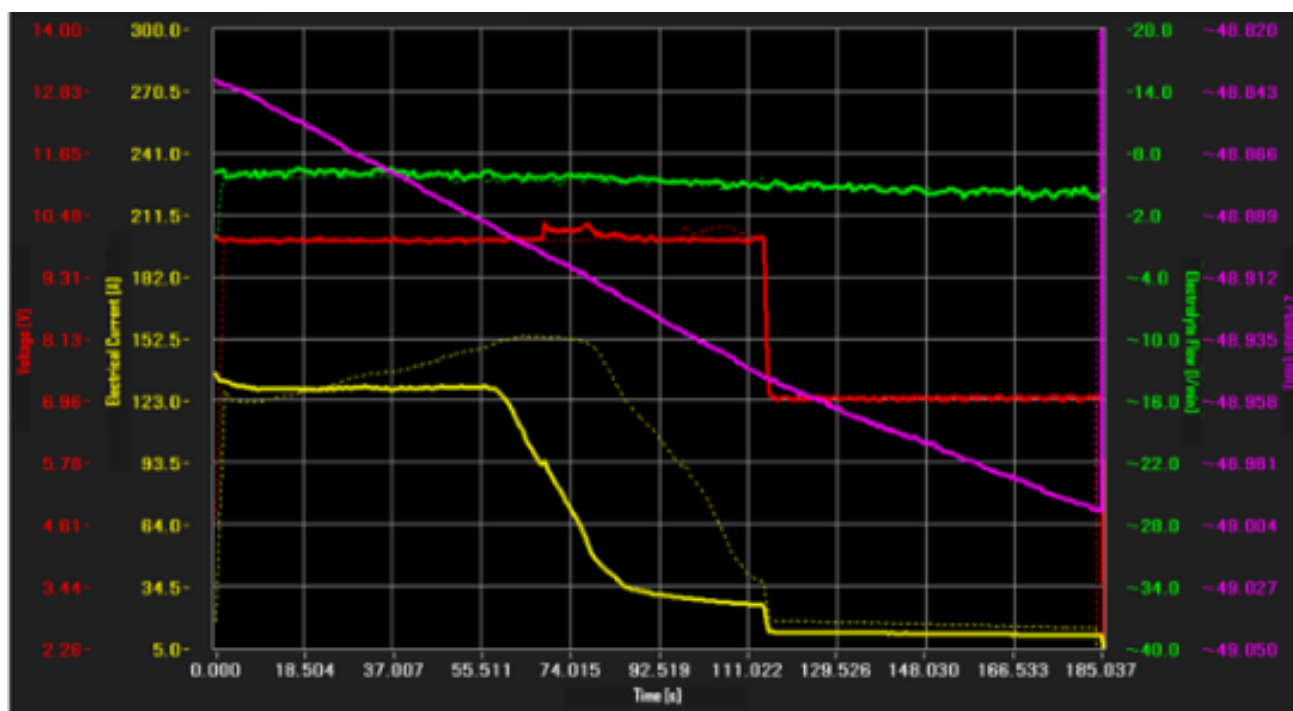
Potential improvements can be done on the sheet preparation. The amorphous metals do not have as much manufacturing grease on the surface as the stainless steels from the coil. Therefore, it is possible that with only the mechanical degreasing step, it will eliminate the surface attacks from the pre-etchant. Another option would be to change the solution of the pre-etchant in order to minimise the chlorine-induced surface attack.

### 4.1.2 Precision/Pulse Electrochemical Machining (PECM)

#### 4.1.2.1 Processability with respect to amorphous compositions

The processability of amorphous metals through PECM was under debate prior to this project as it had never been tried before. The first experiments consisted of comparing the thickest metallic glass samples, which would have the most potential application in the shaver, MG-A and MG-B, with the austenitic and martensitic stainless steel metals. Using the same cathode with specific cutting element geometry, the design was machined into each of the metals. The main objective of this trial was to see how the composition and microstructure of the metal affects its processability through PECM. Using the same PECM parameters, the generated current observed can be used to compare the dissolution of each material. These experiments were performed with a trained technician [PG4]. Figure 34 shows the PECM graphs generated during the experiment.

# Amorphous Metal: MG-A



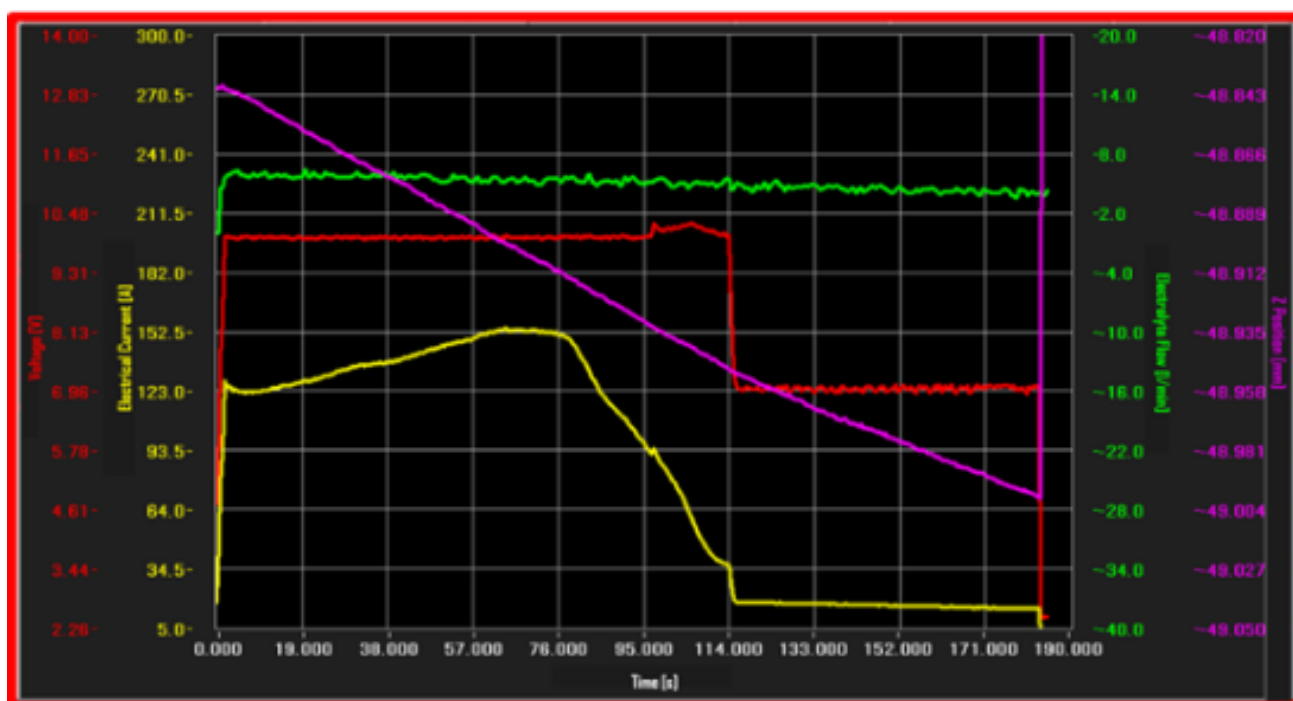
Voltage [V]

Electrical Current [A]

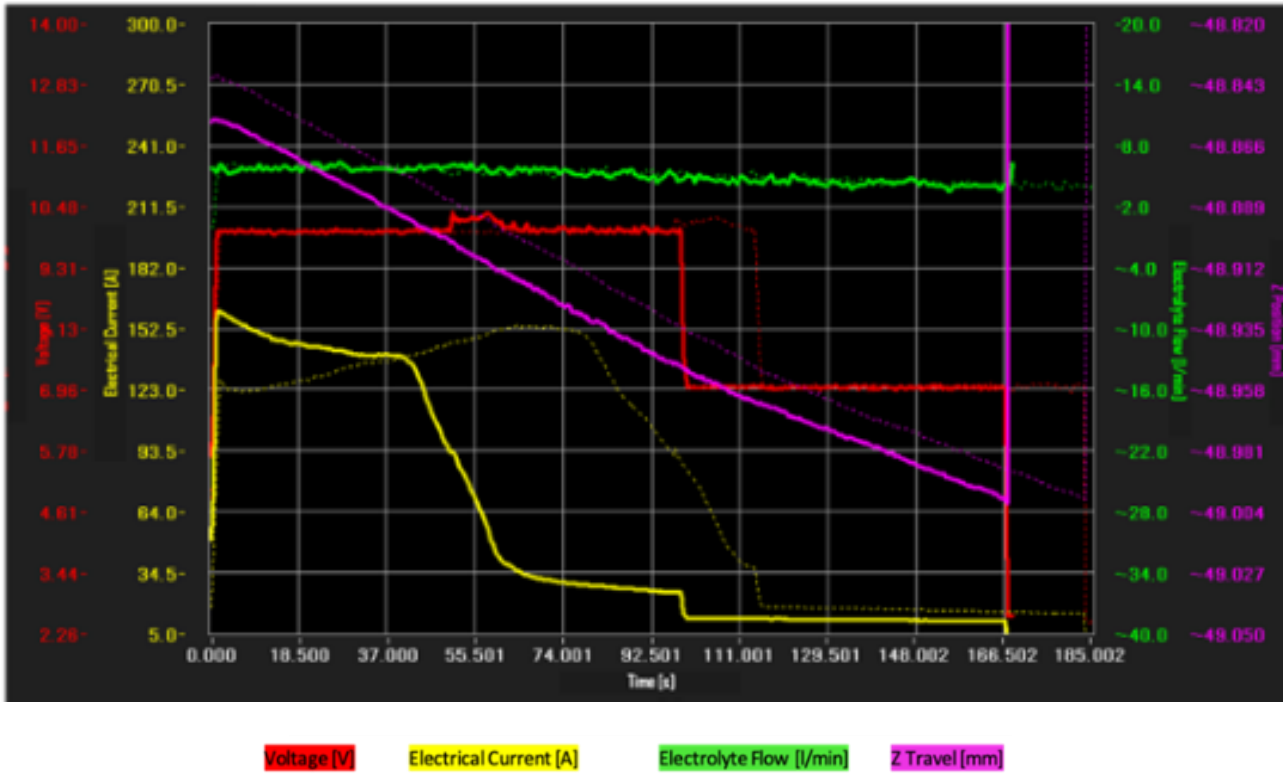
Electrolyte Flow [l/min]

Z Travel [mm]

# Amorphous Metal: MG-B



### Stainless Steel: StAust



### Stainless Steel: StMart

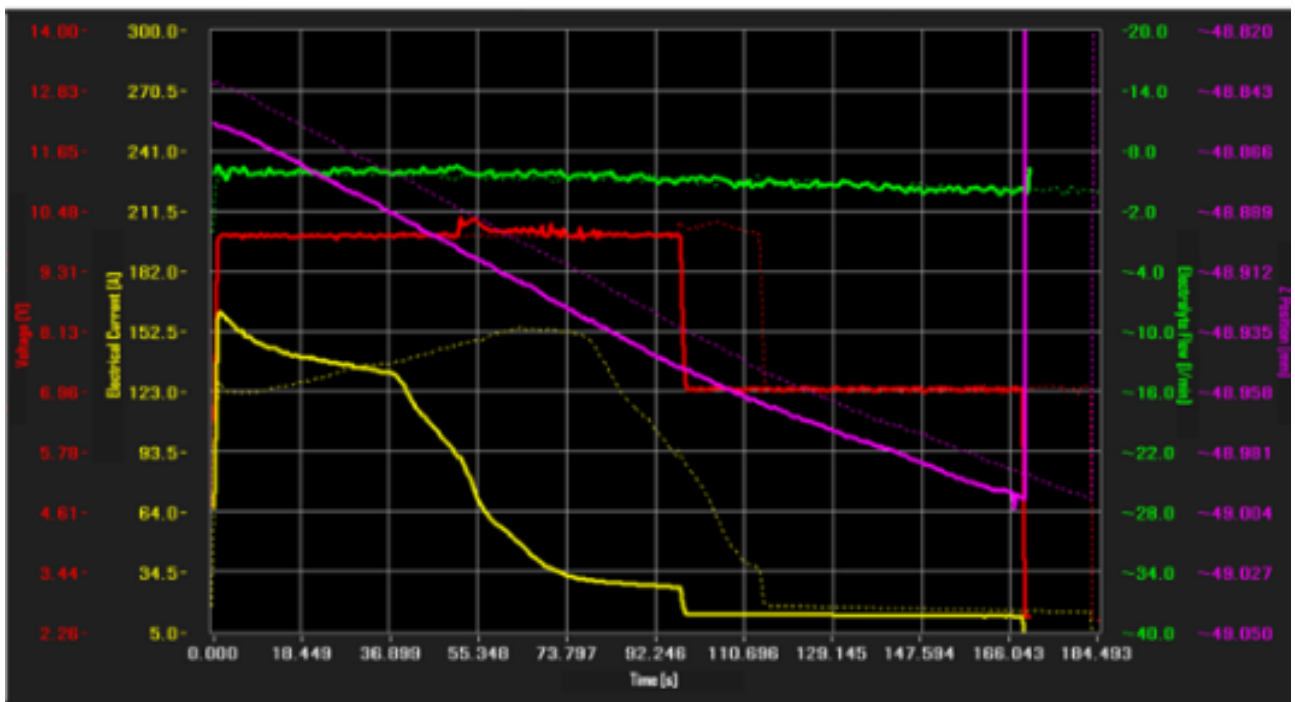


Figure 34: PECM generated graphs of amorphous metals MG-B and MG-A and stainless steels StAust and StMart using the same PECM parameters

Sample MG-B is shown to be the most difficult sample to dissolve, highlighted with a red box. The electrical current generated (yellow line) increases when the working gap is reduced, implying that the

dissolution rate is slower, as can be seen in the graph of MG-B. Therefore, the program was based off of this metal and applied to the other materials (highlighted in a red box), and its graph is present in dashed lines in the back of the other three graphs for more direct comparison.

#### 4.1.2.2 PECM Trials

SEM images of the samples from the graphs of Figure 34 are shown in Figure 35.

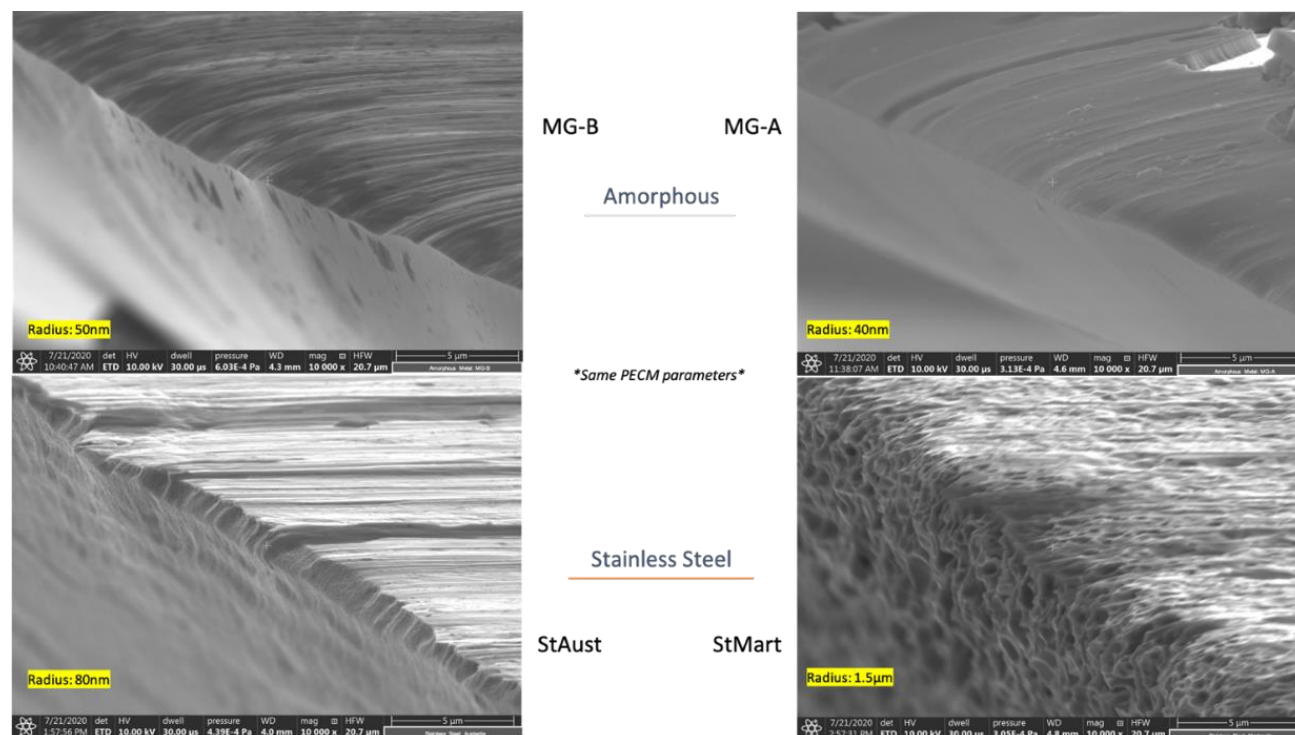


Figure 35: SEM images of the samples after PECM and the respective cutting edge radius measured in the SEM

Similar to the etching trials, the sharp cutting edges of the amorphous metals are smooth and homogenous as opposed to the rougher texture apparent in the StMart sample. The austenitic stainless steel has less of the bread-knife-like edge than the martensitic stainless steel arising from the smoother microstructure of the metal. The cutting edges of both metallic glasses were measured using the software in the SEM and reach 40 to 50 nm compared to the crystalline metals, showing not only the successful processability of the materials but also the shaper cutting edges achieved.

An unexpected result from the PECM processing on amorphous metal MG-A was the surface of the sample seen in the SEM images, shown in Figure 36.

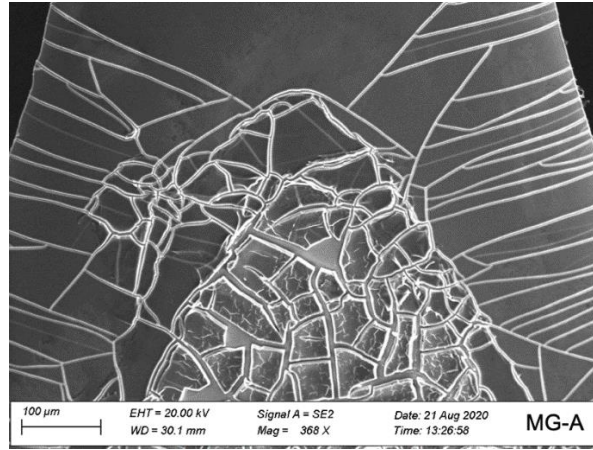


Figure 36: Image of MG-A surface after PECM

This texture of “cracked-glass” on the surface raised the concern of possible unintentional crystallisation of the amorphous metal, similar to that seen in Figure 14. For this reason, the second research question was designed; the characterisation of the amorphous metals before and after processing to verify that the necessary properties (hardness, corrosion resistance, etc.) are maintained after PECM and not impacted by the process.

#### 4.1.2.3 Challenges and Possible Improvements

The main challenge that arose from the PECM process was the buckling of the sample. Due to the small thickness of the metallic glasses, the oscillation of the cathode causes the material to lift and touch the cathode. This short-circuits the program, making the process stop, and thereby reducing the reproducibility of the cutting elements. This can be resolved through inserting a down-holder that is integrated within the cathode. This plastic down-holder comes out through the middle of the cathode and holds the piece down during the process to prevent the sample from buckling. Considering the expensive nature of designing and producing such a specific cathode, double sided tape was used to fix the sample down.

#### 4.1.3 Comparing Etching and PECM

For direct comparison between materials and processes, the same samples and geometry that were etched were also machined through PECM: the StMartHd stainless steel and the amorphous metal MG-B, processing against the matte side. To understand the differences more visually, Focused Ion Beam cuts via SEM were performed on the samples, with the aid of an expert [PG8]. This consists of depositing platinum on a specified area of the surface and cutting through the material with gallium ions. Figure 37 shows each step of this procedure.

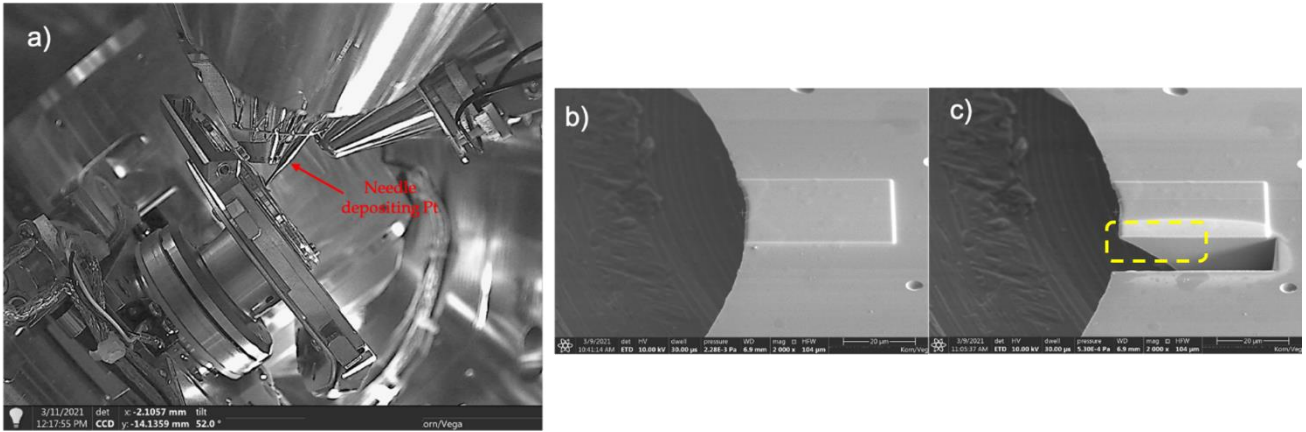


Figure 37: (a) Picture taken inside the SEM of the sample holder and the needle, (b) the surface of the material after the deposition of platinum and (c) after the FIB cut. The yellow dashed box on (c) indicates the area where the following SEM images were taken

The images taken of the FIB cuts are shown in Figure 38.

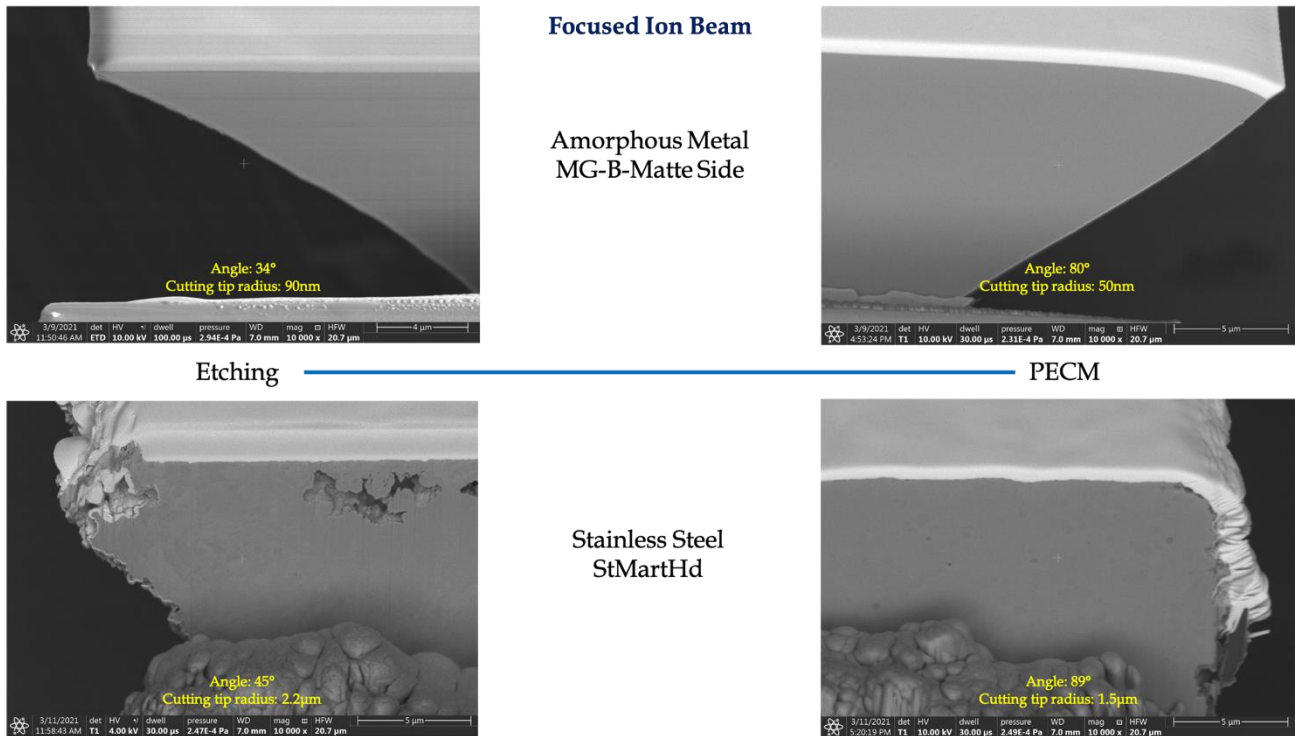


Figure 38: Focused ion beam cuts of amorphous metal MG-B-Matte side and StMartHd after etching and PECM with the respective cutting angles and tip radius measured in the SEM

These images provided not only insight on the achievable sharpness of the cutting edges of the amorphous metals, but also how the different processes affect the resulting tips. (Note, the lighter layer on the surface of the metal is the platinum deposition, not the material itself.) Primarily, the cutting tip radius of the amorphous metal MG-B through both etching and PECM reach much sharper edges than the StMartHd, 50 to 90 nanometers compared to 1.5 to 2.2 micrometers. For both materials, the angle of the edge is larger after PECM than after etching. This could be due to the nature of the process, as with PECM the cathode travels straight down into the material while the etchant in the photochemical machining spreads through the uncovered

by laminate area and dissolves the metal. Furthermore, the cavity seen in the StMartHd etched sample provides additional insight into the attack of the pre-etchant on the surface. A cutting test could determine which process achieves the more efficient performance.

All amorphous metal samples were processable through PECM. The parameters had to be adjusted for the varying thicknesses, but it was confirmed that the composition does not influence the overall processability to the same degree as with etching. This is also the case for which side the amorphous metal should be processed against. For photochemical machining, the matte-side-etching yielded the straightest cutting edges. The correlation between composition and processing is summarised in Table 3.

*Table 3: Amorphous metal sample and successful processing method*

Amorphous Metal	PECM	Photochemical Machining (Etching)
MG-A		No dissolution
MG-B		Matte-side etching
MG-C		Matte-side etching
MG-D		No dissolution

## 4.2 Material Characterisation

The analytical characterisation experiments were performed to verify that the advantageous amorphous metal properties are maintained after processing, as stated in the Research Question 2. It is also a way to analyse the influence of compositions and categorise the best performing metallic glass from the samples available as well as comparing them to the reference materials currently used in shavers. Additionally, further understanding of the properties of amorphous metals after crystallisation was required. Therefore, the samples under investigation were classified into three categories:

Raw: samples cut straight from the manufactured coil.

PECM: amorphous metals that have been processed through PECM. This was due to the surface observed on MG-A after PECM, where it resembled “cracked glass”.

ReX: these amorphous metals samples have undergone heat treatment to purposely crystallise the structure. This involved heating up to 700°C by 10 K/min and cooled to room temperature, allowing for the nucleation of grains.

Due to the adjustments to business needs, not all material samples were investigated through each analytical method. However, it was maintained that each experiment was also applied to at least one reference material.

To facilitate the following discussion points from the presented data, Table 4 summarises the compositions of the amorphous metals in a condensed version.

Table 4: Review of amorphous metal compositions, condensed [wt %]

Amorphous Alloy	Ni	Fe	Cr	Mo	Si	P	B	C
<b>MG-A</b>	70	$\leq 1$	21	-	0.5	8.0	0.5	$\leq 0.1$
<b>MG-B</b>	82.4	3.0	7.0	-	4.5	$\leq 0.02$	3.1	$\leq 0.06$
<b>MG-C</b>	43.6	35	11	1.5	6.4	-	1.5	$\leq 0.1$
<b>MG-D</b>	42.5	32	16	1.5	1.5	6.0	1.5	-

#### 4.2.1 Thermal Analysis

As described in Section 3.3.1, the samples were cut and weighed when placed in the crucible. Table 5 records the mass of each sample.

Table 5: Mass log of samples measured in DSC

Material Class	Sample	Raw/PECM'ed	Sample Holder	Mass [mg]
<b>Amorphous</b>	<b>MG-A</b>	<i>Raw</i>	<b>A1</b>	4.458
			<b>A2</b>	4.373
		<i>PECM</i>	<b>A3</b>	4.648
			<b>A4</b>	4.501
	<b>MG-B</b>	<i>Raw</i>	<b>B1</b>	4.667
			<b>B2</b>	4.572
		<i>PECM</i>	<b>B3</b>	4.656
			<b>B4</b>	4.640
	<b>MG-C</b>	<i>Raw</i>	<b>C1</b>	4.485
			<b>C2</b>	4.433
		<i>PECM</i>	<b>C3</b>	4.499
			<b>C4</b>	4.495
<b>Stainless Steel</b>	<b>MG-D</b>	<i>Raw</i>	<b>D1</b>	4.493
			<b>D2</b>	4.435
	<b>StAust</b>	<i>Raw</i>	<b>E1</b>	4.679
			<b>E2</b>	4.725
			<b>F1</b>	4.775
			<b>F2</b>	4.834

Each sample had two measurements taken. The amorphous metal samples were taken both raw and after PECM, excluding MG-D as it was a new composition and had not yet been processed at the time of this thermal analysis. The two stainless steels were included in this analysis to further understand amorphous metal behaviour compared to traditional crystalline metals. Additionally, there does not exist the similar risk of crystallisation after processing with the stainless steels and were therefore only used as raw.

Figure 39 is an overlay of the DSC scans of one of each of the samples measured, in both conditions (raw/PECM). The execution of the DSC scans as well as the peak determination was performed by an expert [PG3].

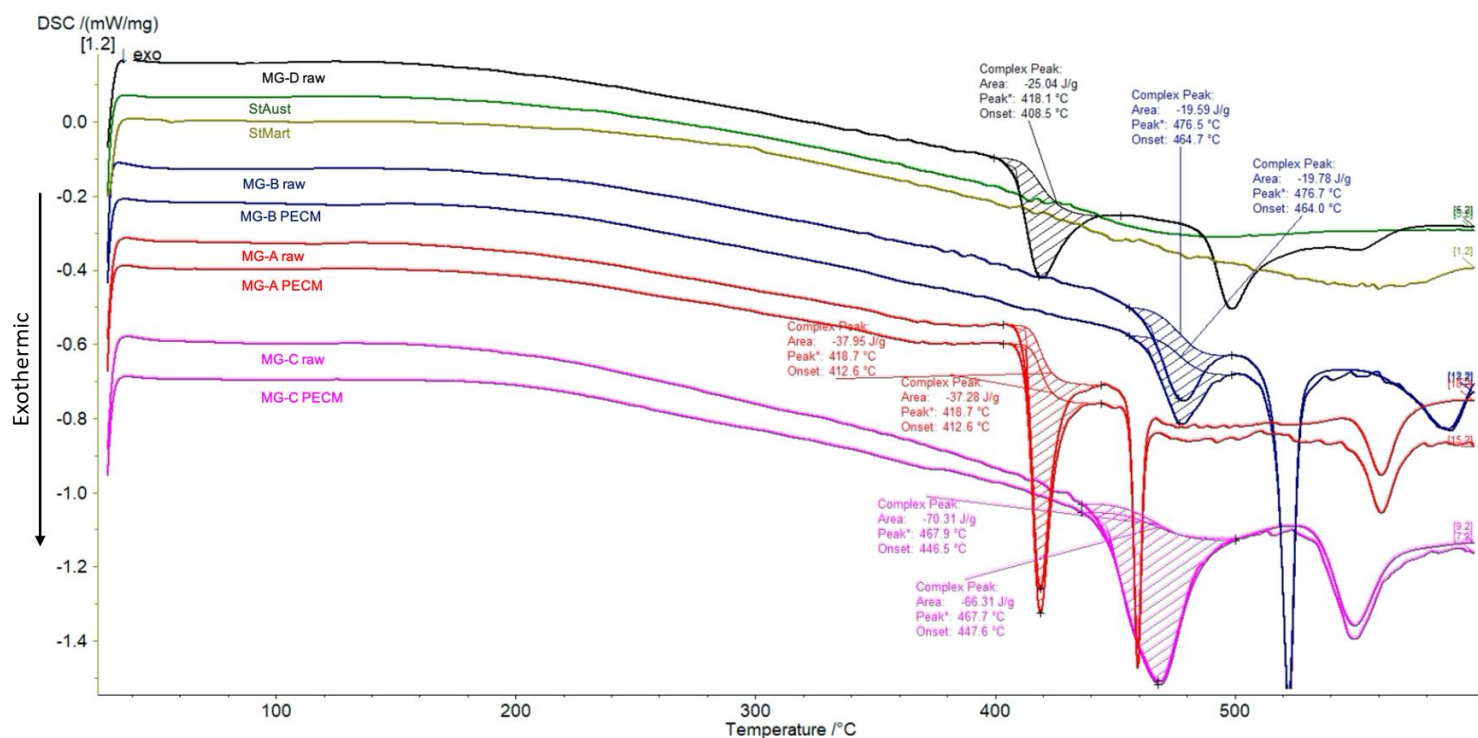


Figure 39: DSC scans overlay showing the raw and PECM conditions for amorphous metals MG-A,B,C and raw condition of MG-D. Stainless steel samples StAust and StMart are included

The first point of comparison is between the amorphous metal and the stainless steel reference samples. As can be seen, the metallic glasses exhibit exothermic peaks, beginning in the range of 400°C. This is indicative of the crystallisation of an amorphous structure, therefore not present in the austenitic and martensitic stainless steels. The small endothermic peak present before the large exothermic peak is evidence of the glass transition. The stainless steels have a melting temperature over 1000°C and will thus not be affected in this specified temperature range (max 600°C).

Figure 39 also displays the data of the first peak of each amorphous metal scan. This includes the area of the peak, peak temperature, and the onset temperature. Table 6 summarises this data.

Table 6: DSC curve material summary from Figure 39. Uncertainty associated with determination of peak onset  $\pm 5$  °C

Sample	Raw/PECM'ed	Area [J/g]	Peak Temp [°C]	Onset Temp [°C]
MG-A	Raw	-38.0	419	413
	PECM	-37.3	419	413
MG-B	Raw	-19.6	477	465
	PECM	-19.8	478	464
MG-C	Raw	-70.3	468	445
	PECM	-66.3	468	448
MG-D	Raw	-25.0	418	409

Literature [96] [97] shows that the DSC is sensitive to the heat evolved during the formation of new phases and highlights the changes in the chemical short-range order of the amorphous structure. Therefore, each exothermic peak in the DSC scan is a stage of crystallisation, the biggest peak representing the dominant crystallisation process. The subsequent smaller peaks belong to small volume changes in the chemical short-range order during the diffusion rearrangement of the metastable crystalline phases into a stable compound phase.

When comparing the amorphous metals between each other, the onset temperature of the first crystallisation peak is an indication of the thermal stability of the metal. Reported by Masumoto [77] is the correlation between the crystallisation temperature and the combination of transition metal base (Fe, Co, Ni) and metalloids (P, C, Si, B). It is found that in general iron-based amorphous metals have a higher thermal stability than nickel-based alloys. However, the addition of phosphorus significantly lowers the crystallisation temperature. Contrarily, the addition of silicon increases the crystallisation temperature. These trends are observed in the DSC data of these amorphous samples. The lowest peak temperatures are of the alloys that contain phosphorus, whilst the two highest have higher concentrations of silicon.

The main objective of this thermal analysis was to verify that the metallic glass samples were not impacted after PECM with respect to the amorphous structure, in the sense that no undesired crystallisation occurred. This is only applicable to amorphous metals MG-A, MG-B, and MG-C that were analysed before (raw) and after PECM. Through thermal analysis, the degree of crystallinity can be analysed with the DSC as the peak area and glass transition would be different if the sample had crystallised [72]. Both MG-A and MG-B have almost identical peak areas. However, MG-C has a discrepancy of 4.00 J/g, which could be within the range of precision of the DSC as well as the uncertainty associated with the method of determining the initial point of the peak ( $\pm 5^\circ\text{C}$ ). It also had the largest peak area of all the samples, indicating greater changes in short range chemical order. Performing X-Ray Diffraction analysis on these samples can confirm crystallisation after PECM and provide more information on the crystal structure of the grains.

#### 4.2.2 Hardness

The hardness measurements were performed with the microindenter on the cross-section of the embedded samples in both the parallel and perpendicular directions. This was followed by measuring the length of the diagonals of the indentation with the light microscope and calculating the hardness. Collaboration and training were given by an expert [PG8]. A summary of the results is shown in Figure 40. The materials under investigation are the four amorphous metals in the three conditions: raw, PECM (except for MG-D) and after heat treatment, ReX. The reference material used for the hardness comparison was the hardened martensitic stainless steel, StMartHd. Figure 40 shows the hardness values after averaging the parallel and perpendicular directions.

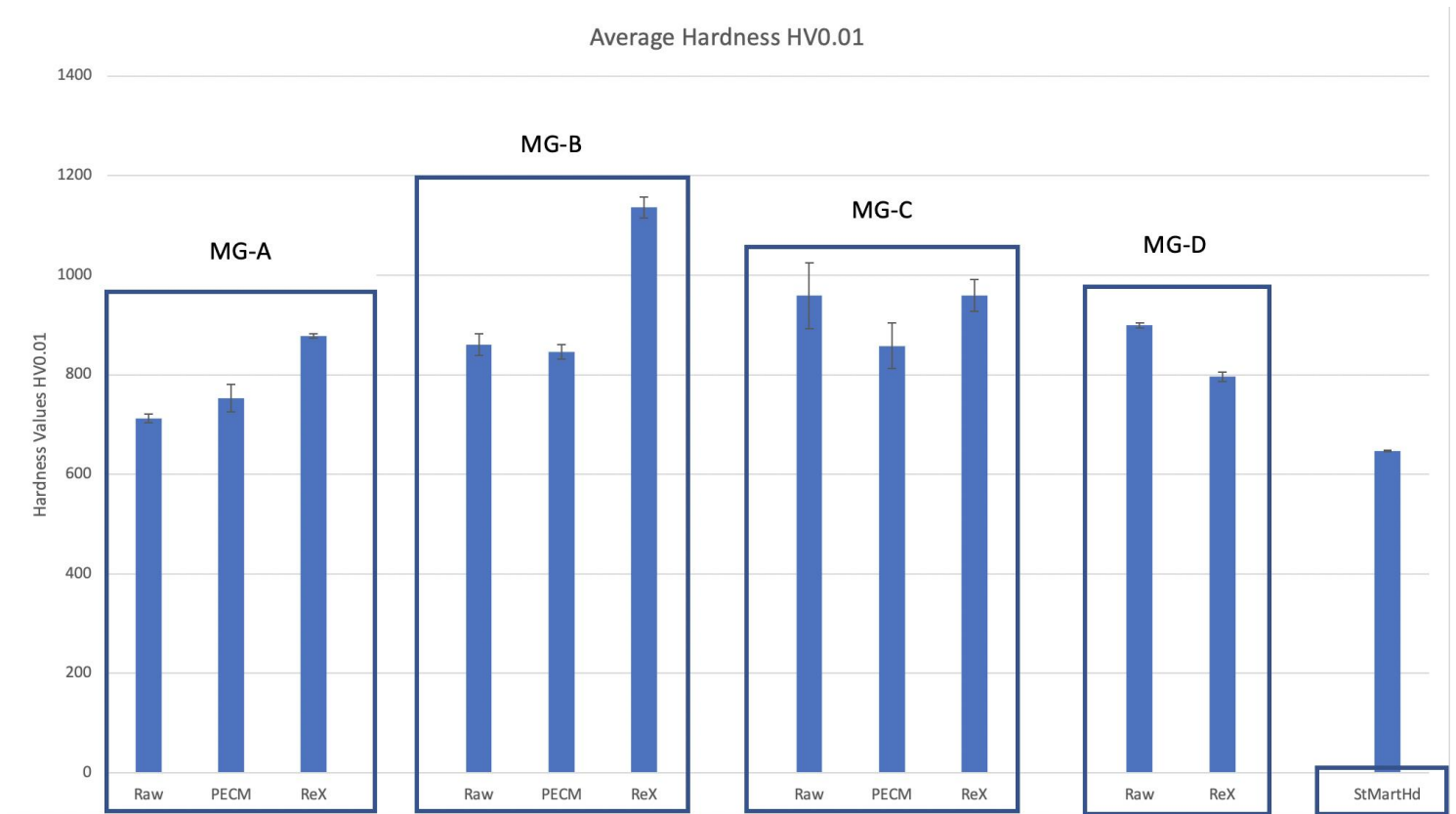


Figure 40: Average hardness values reported in HV0.01

The first conclusion that can be seen directly is that the hardness values of the metallic glasses are higher than of the reference stainless steel. This is due to the disordered structure of the amorphous metal, exhibiting a lack of translational symmetry within the atomic structure and without well-defined crystallographic slip systems and dislocation-mediated mechanisms [98]. The difficulty in movement of the atoms results in very hard materials.

The next point of comparison is the condition of the metallic glass within each composition. As can be seen, the hardness values of the Raw and PECM samples are not significantly different for the three amorphous metals. There is a more distinct variation between the Raw and PECM of sample MG-C, although it is still within the standard deviation. This offers more security in the conclusion that the amorphous structure is not affected by the PECM process. To expose the microstructure, colour etching was applied to the cross-section of the embedded samples, shown in Figure 41.

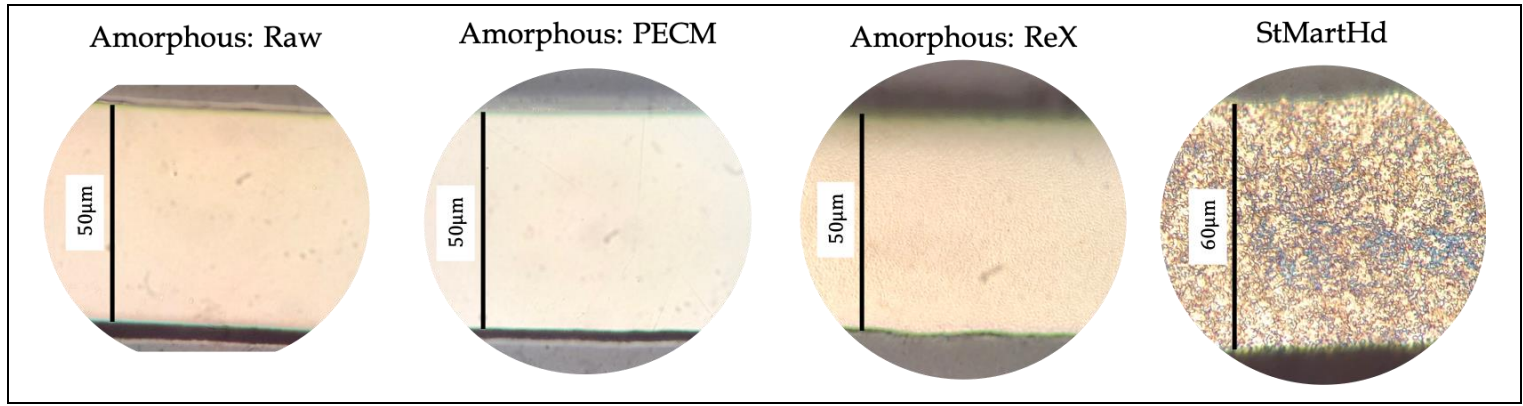


Figure 41: Colour etching of amorphous metal in Raw, PECM and ReX condition and the reference stainless steel StMartHd.

The unexpected values came from the crystallised samples, ReX. Research [66] [99] show that the crystallisation of amorphous metals causes drastic effects on the mechanical properties. However, samples MG-A and MG-B clearly show higher hardness values in ReX than in the Raw condition. This could be due to nano-crystallites forming in the structure through the nucleation of the grains, as seen in Figure 41. It was found in a study [100] that dual-phase amorphous-crystalline alloys exhibited an enhanced hardness and elastic modulus with increasing volume fraction of nanocrystals. It is known that nanocrystalline alloys are strong as a result of the Hall-Petch effect [101]. This relation explains that the strength of the material is inversely proportional to the square root of the grain size, evident when comparing the hardness and grain size of the amorphous metal compared to the stainless steel sample.

A study [99] performed on the partial crystallisation of an aluminium-based amorphous metal showed an increase in Vickers hardness values due to the formation of three specific crystallisation reactions: alpha-Al crystallites,  $\text{Al}_3\text{Ni}$  and  $\text{Al}_{11}\text{Ce}_3$ . It was also found that the hardness increased with increasing volume fraction of alpha-Al. Although the amorphous metals used in this project are of different compositions than this cited literature [99], the findings could provide insight as to why the hardness increases after crystallisation. Further investigation into the crystal formation of the given metallic glass samples used here after heat treatment with X-Ray Diffraction could offer additional understanding to the correlation between the crystallising phases and the increase in hardness.

It must be pointed out however, that an increase in hardness of the heat-treated metallic glass samples does not offer a potential use in this specific application of shaving elements. This is due to the extreme brittleness of the material after crystallisation. When fitting the sample in the holder for the embedding process, it would easily crack into little pieces if only slightly bent. Figure 42 is a picture of the heat-treated amorphous metal MG-A, after attempting to be cut down the middle with scissors.

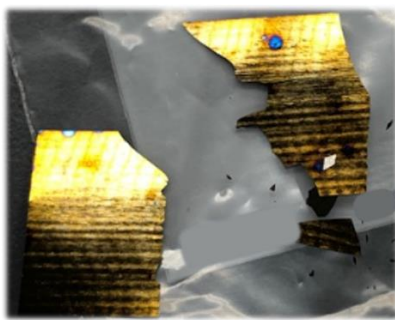


Figure 42: Heat-treated MG-A broken to pieces after cutting with scissors

The next point of comparison is between the amorphous metals with respect to the composition. Focusing on the Raw state for each material, it can be seen that MG-C and MG-D have higher hardness values than MG-A and MG-B. The main reason for this is the increased concentration of iron for both these metallic glasses. The very slight advantage that MG-C may have over MG-D with respect to the hardness is that it contains higher levels of silicon, whilst MG-D contains phosphorus. It was reported that the order of metalloid content for increasing hardness is P, C, Si and B [72].

#### 4.2.3 Corrosion Resistance

The three different electrochemical analyses that were performed, the open circuit potential, the potentiodynamic measurements and the double-loop electrochemical potentiokinetic reactivation, will be discussed in this section. Similar to the hardness measurements, the corrosion resistance was tested on the three conditions: raw, after PECM and after heat treatment (ReX). However, since the samples had to be in the coin shape for the electrochemical set up, the PECM condition was recreated by exposing the raw sample to the PECM electrolyte,  $\text{NaNO}_3$ , and applying a voltage. These experiments were performed by an expert [PG2] and his apprentice [PG9].

##### Open Circuit Potential

The first electrochemical analysis that will be discussed is the open circuit potential performed in the artificial skin sweat solution. Figure 43 illustrates the equilibrium potential of the metal in the solution with respect to time. *Note: there are two lines present for each amorphous metal. These represent the corrosion analysis of each side of the metallic glass (the glossy and matte). For this discussion the materials will be analysed as a whole rather than by specific sides.*

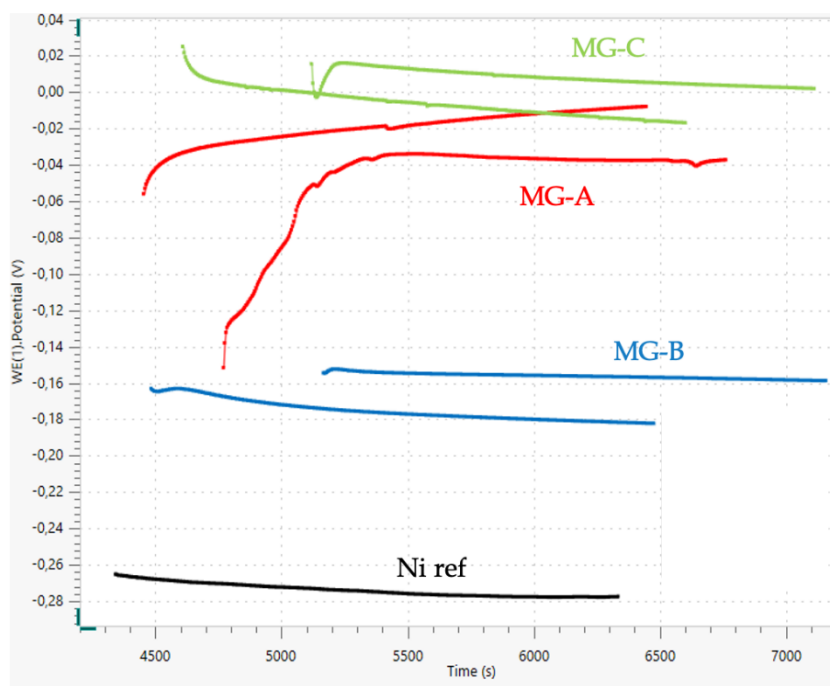


Figure 43: Open Circuit Potential of the raw amorphous metals MG-A (red), MG-B (blue), MG-C (green) [with the Glossy side having a higher potential than the Matte side for each amorphous metal] and the reference nickel reference (black).

The higher the measured potential, the greater the corrosion resistance. As can be seen, all three amorphous metals exhibit a higher equilibrium potential than the nickel reference material. This is the first indication that the metallic glass samples have a better corrosion resistance to the sweat solution.

From the observed surface of the amorphous metal MG-A after PECM, it was hypothesised that the corrosion resistance, a surface property, could be affected. Therefore, the same open circuit potential was performed on sample after being exposed to the PECM electrolyte,  $\text{NaNO}_3$ . The corrosion resistance in artificial sweat of the amorphous metals after the recreated PECM procedure is shown in Figure 44.

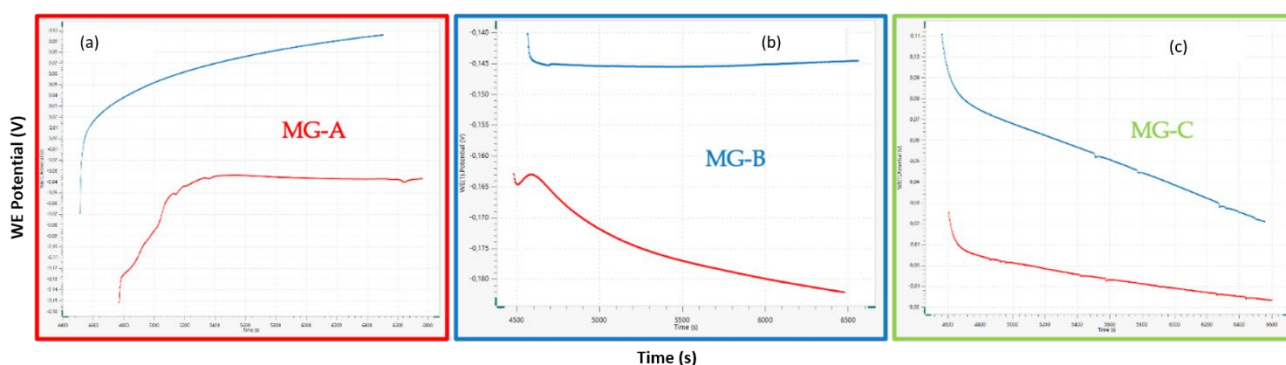


Figure 44: Open Circuit Potential of amorphous metals MG-A (a), MG-B (b) and MG-C (c). The red lines are the samples in raw condition and the blue lines are those after having been exposed to the PECM condition.

The open circuit potential is higher after the PECM process for all three amorphous metal samples. A potential explanation for this is that during the PECM process, the  $\text{NaNO}_3$  electrolyte and applied voltage, dissolved the less noble elements including phosphorus and nickel on the surface. This could then allow for

more of the chromium to be exposed and create a stronger passive layer. These results gave an exciting selling point to its use with respect to shavers as the corrosion resistance to sweat is improved after processing.

### Potentiodynamic Measurements

The potentiodynamic analysis in artificial skin sweat of the four amorphous metals and the nickel reference material are shown in Figure 45.

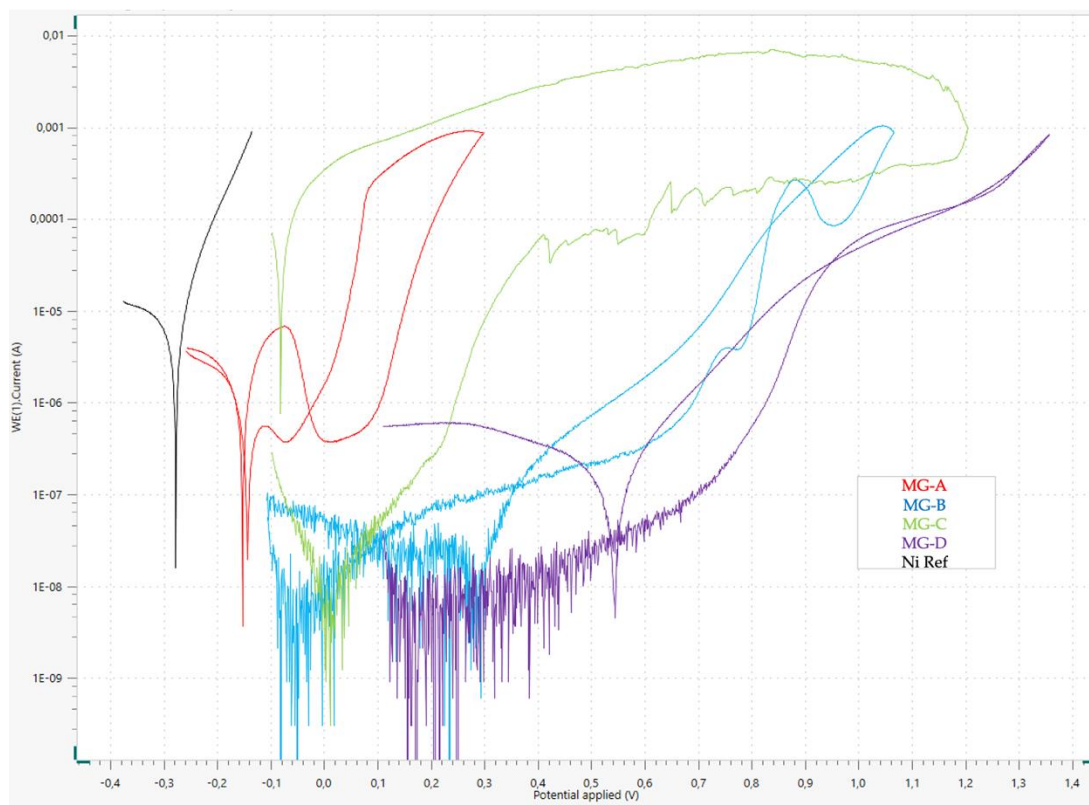


Figure 45: Potentiodynamic analysis in artificial skin sweat of: MG-A (red), MG-B (blue), MG-C (green), MG-D (purple) and the nickel reference (black)

The general trend of the curves follows the transition of the negative current representing the cathodic reaction (hydrogen evolution) to a positive current, the anodic reaction (oxidation). The peak at which the reactions transition from negative to positive illustrates the corrosion potential. The higher the corrosion potential, the better the corrosion resistance. The nickel reference material scan in Figure 45 shows to have the lowest corrosion potential, thereby the weakest corrosion resistance, in agreement with the open circuit potential analysis in Figure 43. Sample MG-D has the highest corrosion potential.

Another clear difference between the nickel sample and the amorphous metals is the anodic current. For the nickel, there is direct dissolution of  $\text{Ni} \rightarrow \text{Ni}^{2+} + 2\text{e}^-$  above the corrosion potential without any passivation. However, MG-C for example shows an extended potential range with near constant current. This is the formation of a passive layer, a dense nonporous chromium/molybdenum-oxide layer. As the potential further increases, the current suddenly increases by orders of magnitude, highlighting the breakdown of the passivation

layer, no longer protecting the material. This passive layer is not as clearly defined in sample MG-A. This analysis on the corrosion resistance of the samples in artificial skin sweat indicates the longevity of the cutting element should it be implemented in the shaver.

### Double Loop Electrochemical Potentiokinetic Reactivation

As explained, stainless steels are prone to intergranular corrosion due to the chromium depletion along grain boundaries arising from the precipitation of chromium carbides. This phenomenon would not be apparent in amorphous metals as there are no grains or grain boundaries. The Double Loop-EPR demonstrates this form of corrosion. Figure 46 shows the data of amorphous metal MG-C and the reference martensitic stainless steel StMart.

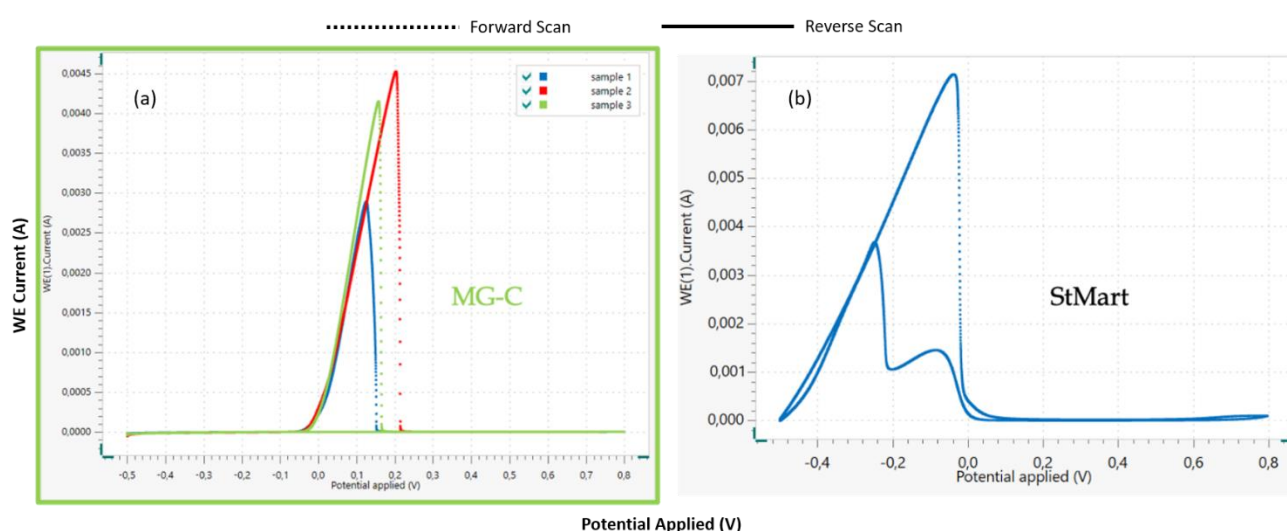


Figure 46: Double Loop-EPR of three measurements of (a) raw MG-C and (b) the reference material, StMart, where the dotted line is the forward scan and the solid line is the reverse scan

From the metallic glass sample on the Figure 46 (a), it can be seen that for all three replicated measurements, the reverse scan shows no peak. This indicates that the material has no sensitisation and therefore no intergranular corrosion. On the other hand, the stainless steel in Figure 46 (b) does exhibit sensitisation observed from the peaks on the reverse scan. Having this comparison made the indication to crystallisation more apparent for the heat-treated samples. This same amorphous sample MG-C was analysed in the ReX condition, shown in Figure 47.

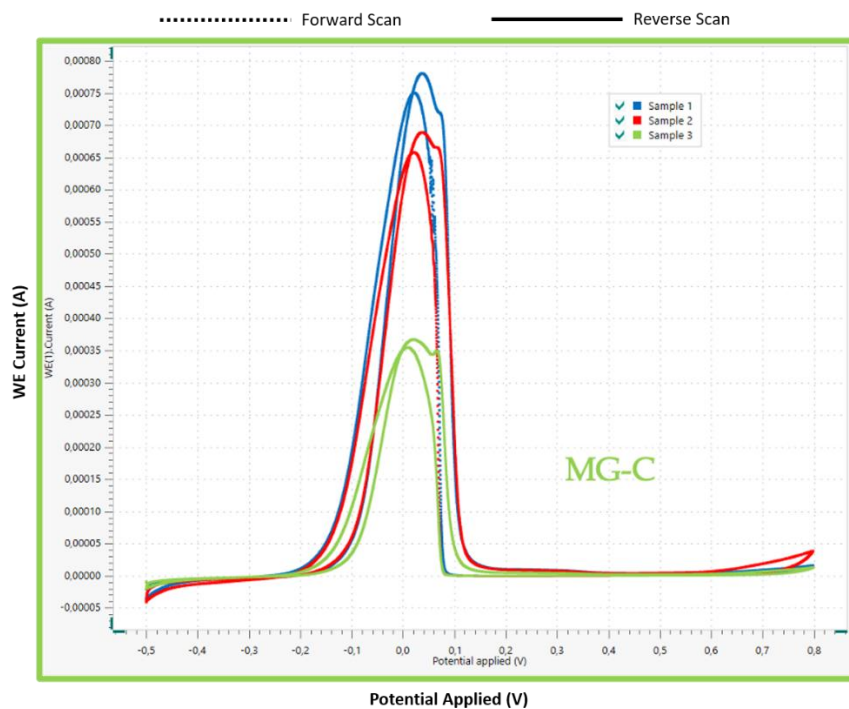


Figure 47: Double Loop-EPR of three measurements of the heat-treated amorphous metal MG-C, where the dotted line is the forward scan and the solid line is the reverse scan

As can be seen from these scans, the reverse sweep now shows a peak for each measured sample, indicating intergranular corrosion. Comparing these scans to those from the raw samples, Figure 46 (a), it is evident that grains have formed and impacted the corrosion resistance to the artificial skin sweat, exhibiting intergranular corrosion from the chlorine ions present in the solution.

#### 4.2.4 Nickel Release

As explained in the introduction, the important factor of nickel related dermatitis is not the content of nickel but the nickel release. The European Union restriction on the Nickel Directive established the limits of levels of nickel release to less than  $0.2 \mu\text{g}/\text{cm}^2/\text{week}$  for assemblies pierced or inside the human body and no more than  $0.5 \mu\text{g}/\text{cm}^2/\text{week}$  for elements with prolonged contact [17].

All amorphous metal samples used in this project are nickel based. The nickel release of each amorphous metal in the three conditions (raw, PECM and ReX) are shown in Figure 48, as well as the nickel reference material and the austenitic stainless steel.

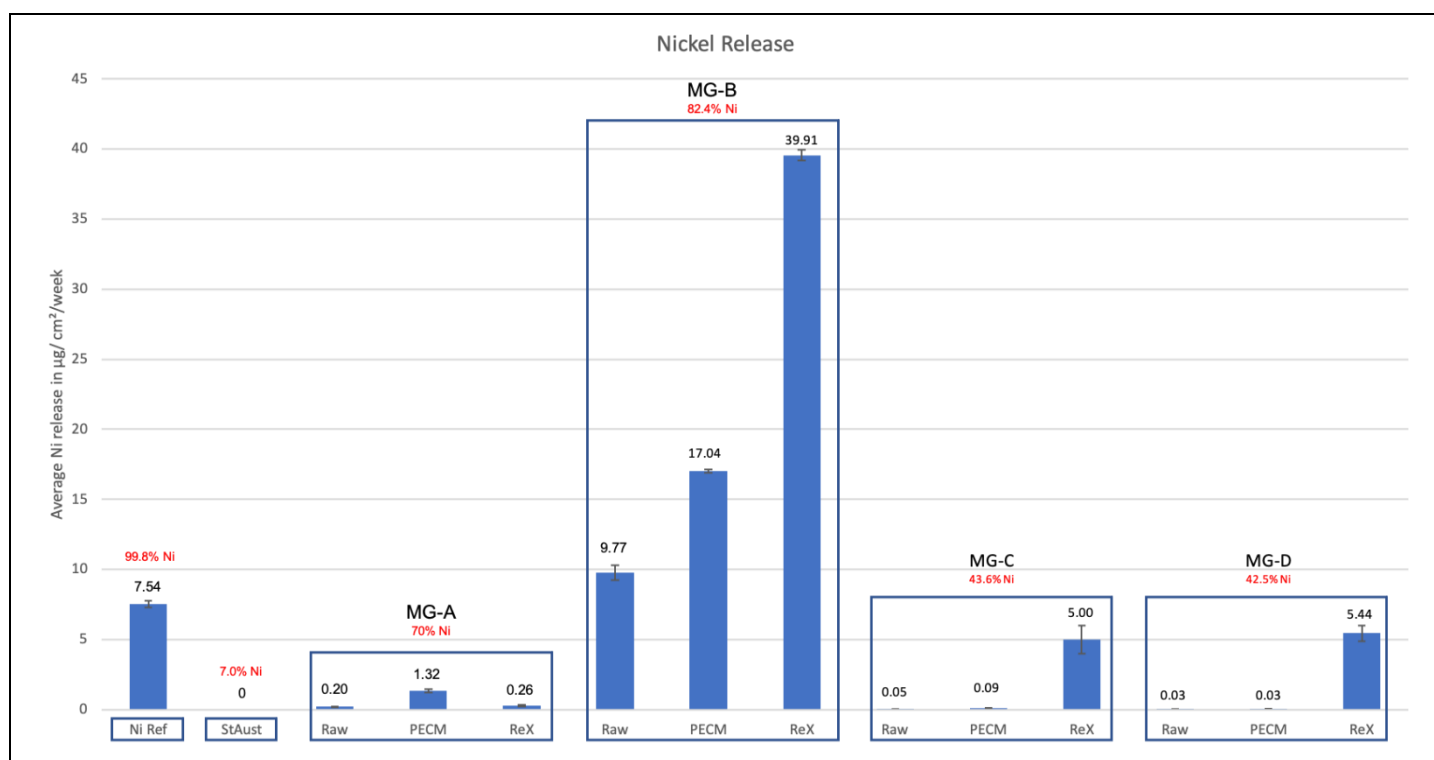


Figure 178: Nickel release in micrograms per centimeter squared per week, values expressed in black with the error bars. In red is the percent nickel content of the sample.

As regulation states, the nickel release of elements making contact with skin should be kept below a threshold. Figure 48 shows that amorphous metal MG-B releases the highest levels of nickel, in any condition, compared to the rest of the samples tested. The rest of the samples, however, release lower levels of nickel than the reference material. The levels of nickel in the solution from the austenitic stainless steel were below the limit of detection (part per billion).

Samples MG-C and MG-D have a very similar response to the artificial skin sweat, with only trace levels in the raw and PECM conditions and around 5 µg/cm²/week of the crystallised sample. Since the metallic glasses MG-C and MG-D have the lowest content of nickel, there is the least amount of nickel released in the raw condition. MG-A has high levels of nickel in the alloy, but released 0.2 µg/cm²/week. The difference between the raw and PECM MG-A values could be attributed to the surface of the material after PECM, this cracked-glass like structure, influencing the expulsion of nickel.

An interesting conclusion from this data is the lack of linearity between the nickel release and the nickel content between the amorphous metals, summarised in Figure 49.

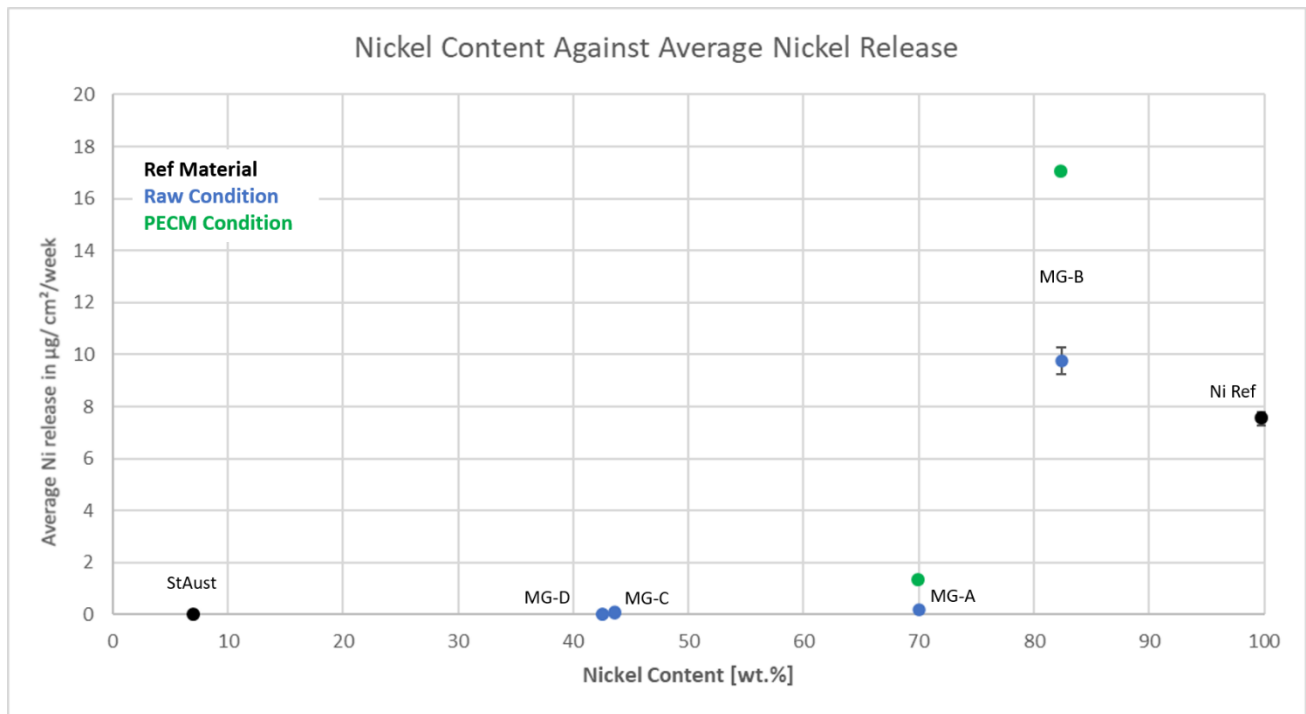


Figure 49: Average nickel release against the nickel content of the sample. The reference materials are in black and the amorphous metals in the raw condition in blue and PECM condition in green. Note: the values of the raw and PECM are indistinguishable for MG-C and MG-D and therefore overlap. Small error bars may not be visible due to the marker.

Although sample MG-B has the highest levels of nickel content at 82.4% and exhibits the highest amounts of nickel release in the three conditions, MG-A has the second highest level of nickel content with 70%, although only releases 0.20  $\mu\text{g}/\text{cm}^2/\text{week}$  in the raw condition. This could be attributed to the overall composition of the alloy, with different elements causing changes in short range order, thereby potentially influencing the ease of nickel release. The lack of linearity could make the predictability of the nickel release based on alloy composition more difficult with future metallic glass samples. Men spend around 5 minutes shaving their beard, potentially every day, but is not considered prolonged contact. However, replacing an element of a shaving machine that releases 7.54  $\mu\text{g}/\text{cm}^2/\text{week}$  as the nickel reference material does with one that releases on average 0.05 to 0.20  $\mu\text{g}/\text{cm}^2/\text{week}$  would reduce the likelihood of nickel related dermatitis.

## 5. Discussion

### 5.1 Processability

The first research question is: How does the composition of the amorphous metal influence the processability of the material? The processability of amorphous metals through photochemical machining and pulse/precision electrochemical machining were explored. With a small-scale beaker experiment investigating the rate of mass loss of the metal in the iron chloride etching solution, it was found that only two of the four amorphous metals dissolve (MG-B and MG-C) and are therefore processable through etching. It is hypothesised that the lack of processability through etching is due to the high levels of chromium and phosphorus in the alloys MG-A and MG-D. This conclusion based on the composition of the alloy could also facilitate future decisions of other potential amorphous metals that become commercially available. Furthermore, it was found that etching against the glossy side of the metallic glass produced cutting edges that were not as smooth and homogenous as etching against the matte side.

The machining of cutting elements through etching results in sharper cutting edges of amorphous metals than those of the hardened martensitic stainless steel. Furthermore, the process of etching is proficient for the bulk mass production of parts. On the other hand, the long loop times result in slow parameter testing for research and development purposes. The overall integration of amorphous metals in this standardised processing method could be applied, adjusting for the dimensions of the metallic glass ribbon as opposed to the large stainless steel sheets.

The use of PECM to machine metallic glasses was shown to be possible and successful. A crucial outcome of these experiments was the verification that all four compositions are processable through PECM. The resulting cutting edges of the machined pieces reached 40-50 nanometers. Additionally, the time required for the machining is a few minutes, making trial and error testing quick and efficient. However, this method produces single pieces, effective for prototyping, but would be more challenging in implementing within the mass production. Additionally, the requirement of a down-holder to fix the sample during the oscillation of the cathode is crucial for reproducibility.

### 5.2 Characterisation

The second research question is: Are the advantageous amorphous metal properties maintained after processing? The first aspect of this guided question refers to the advantageous properties of amorphous metals. Without including a sharp cutting edge, the most important qualities that a cutting element in shavers requires are wear resistance and corrosion resistance. The wear resistance is characterised by the hardness of the material. From Section 4.2.2, the hardness values of the amorphous metals were greater than of the hardened martensitic stainless steel reference metal. Additionally, the metallic glasses have a greater corrosion resistance, demonstrated by the open circuit potential and potentiodynamic experiments from Section 4.2.3. Amorphous

metals are not vulnerable to intergranular corrosion like stainless steels are, due to chlorine ions targeting grain boundaries.

The second aspect of the research question is intended to understand the differences in properties after processing. This was mainly focused on the PECM process due to the nature of the surface found on amorphous metal MG-A. From the thermal analysis, it was demonstrated that the crystallinity of the raw amorphous metal samples and those having been processed by PECM were the same. The hardness was also shown to be the same within the standard deviation of the measurements. However, the surface properties including the corrosion and nickel release did show variation between the raw samples and the samples after PECM processing. One of the biggest selling points of using PECM on amorphous metals was the increase in corrosion resistance. The nickel release was affected after PECM for samples MG-A and MG-B. The analysis of the heated samples, inducing crystallisation in the structure, was purely for research purposes. As was found during the embedding process for the hardness measurements, the brittleness of these crystallised (ReX) samples rendered the material unusable for real-world applications.

### 5.3 Integration in Shaving Appliance





















The final research question is: How can amorphous metals be best utilised as cutting elements in shavers? The knowledge and understanding derived from the first two research questions based on the processability and amorphous metal properties cannot be exploited unless the metal is integrated in the shaver in an appropriate way.

In the shaver design, there are various components that could be considered integrating by metallic glasses. The first is thick stainless steel, above 300  $\mu\text{m}$ , that has direct contact to the face during shaving. Unfortunately, due to the method of manufacturing the amorphous metals by the suppliers, the maximum thickness is currently 75  $\mu\text{m}$ . This renders this option not possible. The next is an integral component for the cutting system, with a thickness above 150  $\mu\text{m}$ . Though the thickness is still a challenge, it could be managed through the adaptation of the design concept to accommodate for a thinner blade. However, the assembly of this component is now done through welding. Welding metallic glasses causes crystallisation due to the applied heat. An alternative to this would be the use of adhesives such as glue. This could be a long-term project to explore different joining technologies. Finally, the nickel component is 60  $\mu\text{m}$  that also makes direct contact with the face. With the increased corrosion resistance to the skin sweat, the lifetime of the element of an amorphous metal would outlast that of the original nickel component. Furthermore, the assembly of this element is a mechanical joining technology, thereby not causing the metallic glass to crystallise. The notion of metallic glasses replacing the current materials used as cutting elements can also be considered in future designs of the next generation shavers.

## 5.4 Trade-Offs

The decision which of the presented amorphous metals would be the most suitable depends on the business needs and requirements. Table 7 emphasises the relative pros and cons of each alloy.

Table 7: Summary of advantages and disadvantages associated with each amorphous metal sample

Property	MG-A	MG-B	MG-C	MG-D
High Hardness				
High Corrosion Resistance				
High Thermal Stability				
Low Nickel Release				
Large Thickness Available				

As can be seen from the table, the advantages and disadvantages of the amorphous metals lead to a trade-off. However, the properties mentioned do not have the same weighing in criticality. For example, MG-C is a hard and corrosion-resistant material, but due to its manufacturing thickness limitation, its application to shaving elements in general could be more challenging than the thicker samples. This is also the case for MG-D. Furthermore, MG-A is a thick material with little nickel release but can only be processed through PECM. Therefore, the decision of whether the processing method or the required physical property is more essential to the business needs must be made prior to choosing from the given amorphous metal samples. For instance, since the photochemical machining provides the most mass production option, the levels of chromium in the alloy would be the determining factor, where only MG-B and MG-C would apply.

Similar to traditional crystalline metals, another benefit of using amorphous metals is the ability to pick and choose the elements involved in the metallic glass alloy to enhance specific properties. For example, it is known that iron-based amorphous metals have a higher hardness than nickel-based. However, iron-based alloys are in general thinner [27]. In the same manner, the metalloid elements and concentration can be adjusted. Boron has been shown to also make the material harder, compared to phosphorus [77], although phosphorus improves corrosion resistance more than the addition of boron [81]. Therefore, it is important to consider the application in question when deciding between these trade-offs.

## 6. Conclusion

The processability of amorphous metals through photochemical machining and pulse/precision electrochemical machining were explored. It was found that the composition limits the processing through etching due to the high corrosion resistance from the levels of chromium and phosphorus. This is not the case for PECM. Although the dissolvability of the metal depends on the composition of the alloy, each of the four amorphous metal samples used in this project were processable through PECM. The advantageous properties of the metallic glasses were not compromised through the processing. The corrosion resistance was found to improve after PECM. The integration of metallic glasses in shavers could replace the nickel component in a short-term solution.

The use of amorphous metals as cutting elements for the next generation of shavers could provide previously unmet consumer benefits. This is highlighted in the superior properties of the material compared to the crystalline stainless steel and nickel reference metals. Not only can the metallic glasses reach nanometer level cutting edges, the wear and corrosion resistance offers a longer lifetime of the blade. This cutting efficiency and longevity provide a more sustainable solution to the currently disposable shavers. Additionally, the recyclability of amorphous alloys could ensure a cradle-to-cradle approach and encourage a circular economy of the socially accepted necessity such as shaving appliance.

## References

Procter & Gamble, KIC sources:

- [PG1] U. Bublitx – MPD Process Development Department
- [PG2] A. Moehring – Analytical Department
- [PG3] P. Weyand – Analytical Department
- [PG4] M. Perez-Molina – MPD Process Development Department
- [PG5] B. Ahmeti – MPD Process Development Department
- [PG6] E. Sabattié – MPD Process Development Department
- [PG7] D. Korn – Analytical Department
- [PG8] S. Harder – Analytical Department

Published sources:

- [1] Tamburrino, F. *et al.* (2018). Advanced Manufacturing for Novel Materials in Industrial Design Applications. *American Journal of Engineering and Applied Sciences*, 11(2), 932-972. <https://doi.org/10.3844/ajeassp.2018.932.972>
- [2] Roscioli, G., Taheri-Mousavi, S. M., & Tasan, C. C. (2020). How hair deforms steel. *Science*, 369(6504), 689–694. <https://doi.org/10.1126/science.aba9490>
- [3] *Your hair can crack steel when it hits the right spot - YouTube.* (2020). [https://www.youtube.com/watch?v=6kgw6j9n\\_2o&feature=youtu.be](https://www.youtube.com/watch?v=6kgw6j9n_2o&feature=youtu.be)
- [4] McVeigh, C., Vernerey, F., Liu, W. K., Moran, B., & Olson, G. (2007). An interactive micro-void shear localization mechanism in high strength steels. *Journal of the Mechanics and Physics of Solids*, 55(2), 225–244. <https://doi.org/10.1016/j.jmps.2006.08.002>
- [5] Chu, J. P., Diyatmika, W., Tseng, Y. J., Liu, Y. K., Liao, W. C., Chang, S. H., Chen, M. J., Lee, J. W., & Jang, J. S. C. (2019). Coating Cutting Blades with Thin-Film Metallic Glass to Enhance Sharpness. *Scientific Reports*, 9(1), 1–11. <https://doi.org/10.1038/s41598-019-52054-3>
- [6] Yi, J., Wang, W. H., & Lewandowski, J. J. (2015). Guiding and Deflecting Cracks in Bulk Metallic Glasses to Increase Damage Tolerance. *Advanced Engineering Materials*, 17(5), 620–625. <https://doi.org/10.1002/adem.201400209>
- [7] Solid Waste and Emergency Response. (1990). *The Environmental Consumer's Handbook*.
- [8] *Coal: Sidetracking the Impurities EPRI OURN.* (1979).
- [9] *Thermal Analysis & Rheology Thermal Analysis Application Brief Detection Of The Glass Transition in Metal Glasses By Differential Scanning Calorimetry (DSC) and Dynamic Mechanical Analysis (DMA).* (n.d.). Retrieved December 25, 2020, from <http://www.tainst.com>
- [10] *Hitachi Metals Amorphous Metal Recycling Plant - Metglas, Inc.* (n.d.). Retrieved December 28, 2020, from <https://metglas.com/hitachi-metals-amorphous-metal-recycling-plant/>
- [11] *Recycling of Amorphous Transformer Cores - Metglas, Inc.* (n.d.). Retrieved December 28, 2020, from <https://metglas.com/recycling-amorphous-transformer-cores/>
- [12] Blengini, G. A., Latunussa, C. E. L., Eynard, U., Torres de Matos, C., Wittmer, D., Georgitzikis, K., ... Pennington, D. (2020). *Study on the EU's list of Critical Raw Materials (2020) Final Report*. Publications Office of the European Union. <https://doi.org/10.2873/904613>

- [13] Amnesty International. (2016). *“This is what we die for”: Human rights abuses in the Democratic Republic of the Congo Power the Global Trade in Cobalt*. London: 71 pages
- [14] Radio Okapi, 15 creuseurs artisanaux morts brûlés dans une galerie souterraine à Kolwezi, 15 December 2017: <https://www.radiookapi.net/actu-alite/2014/12/27/katanga-15-creuseurs-artisanaux-morts-brules-dans-une-galerie-souterraine-kolwezi/>
- [15] Lauwerys, R. and Lison, D. (1994) Health risks associated with cobalt exposure – an overview. *The Science of the Total Environment* Vol 150, 1-6.
- [16] Saito, M., Arakaki, R., Yamada, A., Tsunematsu, T., Kudo, Y., & Ishimaru, N. (2016). Molecular Mechanisms of Nickel Allergy. *International Journal of Molecular Sciences*, 17(2), 202. <https://doi.org/10.3390/ijms17020202>
- [17] *Nickel allergy and EU nickel restriction Position Paper*. (2018).
- [18] Kapsenberg, M.L., Wierenga, E.A., Stiekema, F.E., Tiggeleman, A.M., Bos, J.D. Th1 lymphokine production profiles of nickel-specific CD4+T-lymphocyte clones from nickel contact allergic and non-allergic individuals. *J. Investig. Dermatol.* 1992, 98, 59–63
- [19] *Nickel allergy and EU nickel restriction State of play and challenges ahead articles in direct and prolonged contact with skin BRUSSELS, JUNE 2017 WORKSHOP REPORT*. (2017). Retrieved from <https://www.nickelinstitute.org/KnowledgeBase/>
- [20] Thyssen, J. P., Menné, T., & Zachariae, C. (2012). Allergic nickel dermatitis caused by shaving: Case report and assessment of nickel release from an electric shaver. *Acta Dermato-Venereologica*. Medical Journals/Acta D-V. <https://doi.org/10.2340/00015555-1160>
- [21] Sharma, P., & Inoue, A. (2010). Metallic Glass. In *Handbook of Silicon Based MEMS Materials and Technologies* (pp. 447–472). Elsevier Inc. <https://doi.org/10.1016/B978-0-8155-1594-4.00027-9>
- [22] Greer, A. L. (2014). Metallic Glasses. In *Physical Metallurgy: Fifth Edition* (Vol. 1, pp. 305–385). Elsevier Inc. <https://doi.org/10.1016/B978-0-444-53770-6.00004-6>
- [23] Cheng, Y. Q., & Ma, E. (2011). Atomic-level structure and structure-property relationship in metallic glasses. In *Progress in Materials Science* (Vol. 56, Issue 4, pp. 379–473). Elsevier Ltd. <https://doi.org/10.1016/j.pmatsci.2010.12.002>
- [24] Kartouzian, A., & Antonowicz, J. (2016). Metallic Glasses from the Bottom-up. In *Metallic Glasses - Formation and Properties*. InTech. <https://doi.org/10.5772/63514>
- [25] Inoue, A. (2000). Stabilization of metallic supercooled liquid and bulk amorphous alloys. *Acta Materialia*, 48(1), 279–306. [https://doi.org/10.1016/S1359-6454\(99\)00300-6](https://doi.org/10.1016/S1359-6454(99)00300-6)
- [26] Aqida, S. N., Shah, L. H., Naher, S., & Brabazon, D. (2014). Rapid Solidification Processing and Bulk Metallic Glass Casting. In *Comprehensive Materials Processing* (Vol. 5, pp. 69–88). Elsevier Ltd. <https://doi.org/10.1016/B978-0-08-096532-1.00506-9>
- [27] Jafary-Zadeh, M., Praveen Kumar, G., Branicio, P., Seifi, M., Lewandowski, J., & Cui, F. (2018). A Critical Review on Metallic Glasses as Structural Materials for Cardiovascular Stent Applications. *Journal of Functional Biomaterials*, 9(1), 19. <https://doi.org/10.3390/jfb9010019>
- [28] Greer, A. L., & Ma, E. (2007). Bulk metallic glasses: At the cutting edge of metals research. *MRS Bulletin*, 32(8), 611–615. <https://doi.org/10.1557/mrs2007.121>
- [29] Senkov, O. N., Miracle, D. B., & Scott, J. M. (2006). Development and characterization of Ca-Mg-Zn-Cu bulk metallic glasses. *Intermetallics*, 14(8–9), 1055–1060. <https://doi.org/10.1016/j.intermet.2006.01.024>
- [30] Reardon, A. C. (2011). *Metallurgy for the Non-Metallurgist, Second Edition*. ASM International. <https://books.google.com/books?hl=en&lr=&id=o-YTN9aXAeIC&pgis=1>

- [31] Gostin, P. F., Gebert, A., & Schultz, L. (2010). Comparison of the corrosion of bulk amorphous steel with conventional steel. *Corrosion Science*, 52(1), 273–281. <https://doi.org/10.1016/j.corsci.2009.09.016>
- [32] Li, N., Zhang, J., Xing, W., Ouyang, D., & Liu, L. (2018). 3D printing of Fe-based bulk metallic glass composites with combined high strength and fracture toughness. *Materials and Design*, 143, 285–296. <https://doi.org/10.1016/j.matdes.2018.01.061>
- [33] Tkatch, V., Limanosvkii, A., Denisenko, S., & Rassolov, S. (2002). The effect of the melt-spinning processing parameters on the rate of cooling. *Materials Science*, 91(96). <https://www.sciencedirect.com/science/article/pii/S0921509301013466>
- [34] *Amorphous Metals - Preparation by a Melt-Spinning Method - TIB AV-Portal*. (n.d.). Retrieved November 11, 2020, from <https://av.tib.eu/media/14883>
- [35] Rong, C., & Shen, B. (2018). Nanocrystalline and nanocomposite permanent magnets by melt spinning technique. *Chin. Phys. B*, 27(11). <https://doi.org/10.1088/1674-1056/27/11/117502>
- [36] Pauly, S., Löber, L., Petters, R., Stoica, M., Scudino, S., Kühn, U., & Eckert, J. (2013). Processing metallic glasses by selective laser melting. *Materials Today*, 16(1–2), 37–41. <https://doi.org/10.1016/j.mattod.2013.01.018>
- [37] Mahbooba, Z., Thorsson, L., Unosson, M., Skoglund, P., West, H., Horn, T., Rock, C., Vogli, E., & Harrysson, O. (2018). Additive manufacturing of an iron-based bulk metallic glass larger than the critical casting thickness. *Applied Materials Today*, 11, 264–269. <https://doi.org/10.1016/j.apmt.2018.02.011>
- [38] Li, X. P., Roberts, M. P., O’Keeffe, S., & Sercombe, T. B. (2016). Selective laser melting of Zr-based bulk metallic glasses: Processing, microstructure and mechanical properties. *Materials and Design*, 112, 217–226. <https://doi.org/10.1016/j.matdes.2016.09.071>
- [39] T. Vilaro, V. Kottman-Rexerodt, M. Thomas, C. Colin, P. Bertrand, L. Thivillon, S. Abed, V. Ji, P. Aubry, P. Peyre, T. Malot, Direct fabrication of a Ti-47Al-2Cr-2Nb alloy by selective laser melting and direct metal deposition processes. *Adv. Mater. Res.* 89 (2010) 586.
- [40] *Amorphous Metal Injection Molding - Visser Precision*. (n.d.). Retrieved November 23, 2020, from <https://visserprecision.com/capabilities/amorphous-metal-injection-molding/>
- [41] *Get the Net Shape of Your Part Right out of the Mold*. (n.d.). Retrieved November 23, 2020, from <https://www.liquidmetal.com/net-shape/>
- [42] Telford, M. (2004). The case for bulk metallic glass. *Materials Today*, 7(3), 36–43. [https://doi.org/10.1016/S1369-7021\(04\)00124-5](https://doi.org/10.1016/S1369-7021(04)00124-5)
- [43] Bernal, J. D. (1964). The Bakerian Lecture, 1962. The Structure of Liquids. In *Source: Proceedings of the Royal Society of London. Series A, Mathematical and Physical Sciences* (Vol. 280, Issue 1382).
- [44] Cahn, R.W. and Haasen, P. (1983) Chapter 28. Alloys Rapidly Quenched from the Melt. *Physical Metallurgy*, 3<sup>rd</sup> ed. Elsevier Science Publishers
- [45] Gaskell, P. H. (1979). A new structural model for amorphous transition metal silicides, borides, phosphides and carbides. *Journal of Non-Crystalline Solids*, 32(1–3), 207–224. [https://doi.org/10.1016/0022-3093\(79\)90073-5](https://doi.org/10.1016/0022-3093(79)90073-5)
- [46] Miracle, D. B. (2006). The efficient cluster packing model - An atomic structural model for metallic glasses. *Acta Materialia*, 54(16), 4317–4336. <https://doi.org/10.1016/j.actamat.2006.06.002>
- [47] Fornell Beringues, J. (2012). *Metallic glasses and derived composite materials: a correlation between microstructure and mechanical properties*. [www.lmt.uab.es](http://www.lmt.uab.es)
- [48] Johnson, W. L. (1986). Thermodynamic and kinetic aspects of the crystal to glass transformation in metallic materials. In *Progress in Materials Science* (Vol. 30, Issue 2, pp. 81–134). Pergamon. [https://doi.org/10.1016/0079-6425\(86\)90005-8](https://doi.org/10.1016/0079-6425(86)90005-8)

- [49] Pusztai, L., Sietsma, J., & Thijsse, B. J. (1995). Structure and relaxation of the metallic glass pds2ni32pi6 modelled by reverse monte carlo simulation. *Philosophical Magazine B: Physics of Condensed Matter; Statistical Mechanics, Electronic, Optical and Magnetic Properties*, 71(3), 383–396. <https://doi.org/10.1080/13642819508239041>
- [50] De Hey, P., Sietsma, J., & Van Den Beukel, A. (1998). Structural disordering in amorphous Pd40Ni40P20 induced by high temperature deformation. *Acta Materialia*, 46(16), 5873–5882. [https://doi.org/10.1016/S1359-6454\(98\)00234-1](https://doi.org/10.1016/S1359-6454(98)00234-1)
- [51] Johari, C. P., & Goidstein, M. (1970). Viscous liquids and the glass transition. II. Secondary relaxations in glasses of rigid molecules. *The Journal of Chemical Physics*, 53(6), 2372–2388. <https://doi.org/10.1063/1.1674335>
- [52] Egami, T. (1984). Magnetic amorphous alloys: Physics and technological applications. In *Reports on Progress in Physics* (Vol. 47, Issue 12, pp. 1601–1725). IOP Publishing. <https://doi.org/10.1088/0034-4885/47/12/002>
- [53] Cohen, M. H., & Turnbull, D. (1959). Molecular transport in liquids and glasses. *The Journal of Chemical Physics*, 31(5), 1164–1169. <https://doi.org/10.1063/1.1730566>
- [54] Kalogeras, I. M., & Lobland, H. E. H. (2012). The Nature of the Glassy State: Structure and Glass Transitions. In *Journal of Materials Education* (Vol. 34, Issue 4).
- [55] Sietsma, J., & Thijsse, B. J. (1995). Characterization of free volume in atomic models of metallic glasses. *Physical Review B*, 52(5), 3248–3255. <https://doi.org/10.1103/PhysRevB.52.3248>
- [56] Rätzke, K., H ppe, P. W., & Faupel, F. (1992). Transition from single-jump type to highly cooperative diffusion during structural relaxation of a metallic glass. *Physical Review Letters*, 68(15), 2347–2349. <https://doi.org/10.1103/PhysRevLett.68.2347>
- [57] Beukel, A. Van Den. (1992). Analysis of Anelastic Relaxation and Internal Friction Data of Amorphous Materials. *Physica Status Solidi (A)*, 129(1), 49–58. <https://doi.org/10.1002/pssa.2211290103>
- [58] Duine, P. A., Sietsma, J., & Van Den Beukel, A. (1993). Atomic transport in amorphous Pd40Ni40P20 near the glass-transition temperature: Au diffusivity and viscosity. *Physical Review B*, 48(10), 6957–6965. <https://doi.org/10.1103/PhysRevB.48.6957>
- [59] van den Beukel, A., & Sietsma, J. (1990). The glass transition as a free volume related kinetic phenomenon. *Acta Metallurgica Et Materialia*, 38(3), 383–389. [https://doi.org/10.1016/0956-7151\(90\)90142-4](https://doi.org/10.1016/0956-7151(90)90142-4)
- [60] Tuinstra, P., Duine, P. A., Sietsma, J., & van den Beukel, A. (1995). The calorimetric glass transition of amorphous Pd40 Ni40 P20. *Acta Metallurgica Et Materialia*, 43(7), 2815–2823. [https://doi.org/10.1016/0956-7151\(94\)00450-V](https://doi.org/10.1016/0956-7151(94)00450-V)
- [61] Greer, A. L., Cheng, Y. Q., & Ma, E. (2013). Shear bands in metallic glasses. In *Materials Science and Engineering R: Reports* (Vol. 74, Issue 4, pp. 71–132). Elsevier Ltd. <https://doi.org/10.1016/j.mser.2013.04.001>
- [62] Park, E. S. (2015). Understanding of the Shear Bands in Amorphous Metals. *Applied Microscopy*, 45(2), 63–73. <https://doi.org/10.9729/am.2015.45.2.63>
- [63] Ding, J., Patinet, S., Falk, M. L., Cheng, Y., & Ma, E. (2014). Soft spots and their structural signature in a metallic glass. *Proceedings of the National Academy of Sciences of the United States of America*, 111(39), 14052–14056. <https://doi.org/10.1073/pnas.1412095111>
- [64] Chang, H. J., Kim, D. H., Kim, Y. M., Kim, Y. J., & Chattopadhyay, K. (2006). On the origin of nanocrystals in the shear band in a quasicrystal forming bulk metallic glass Ti40Zr29Cu9Ni8Be14. *Scripta Materialia*, 55(6), 509–512. <https://doi.org/10.1016/j.scriptamat.2006.05.037>
- [65] Ashby, M. F., & Greer, A. L. (2006). Metallic glasses as structural materials. *Scripta Materialia*, 54(3), 321–326. <https://doi.org/10.1016/j.scriptamat.2005.09.051>
- [66] Dittmer, M., & R ssel, C. (2012). Colorless and high strength MgO/Al2O3/SiO2 glass-ceramic dental material using zirconia as nucleating agent. *Journal of Biomedical Materials Research Part B: Applied Biomaterials*, 100B(2), 463–470. <https://doi.org/10.1002/jbm.b.31972>

- [67] Irifune, T., Kawakami, K., Arimoto, T., Ohfuji, H., Kunimoto, T., & Shinmei, T. (2016). Pressure-induced nano-crystallization of silicate garnets from glass. *Nature Communications*, 7(1), 1–7. <https://doi.org/10.1038/ncomms13753>
- [68] Cao, C. C., Wang, Y. G., Zhu, L., Meng, Y., Zhai, X. B., Dai, Y. D., Chen, J. K., & Pan, F. M. (2018). Local structure, nucleation sites and crystallization behavior and their effects on magnetic properties of Fe<sub>81</sub>Si<sub>x</sub>B<sub>10</sub>P<sub>8-x</sub>Cu<sub>1</sub> (x = 0~8). *Scientific Reports*, 8(1), 1243. <https://doi.org/10.1038/s41598-018-19665-8>
- [69] Zhukova, V., Blanco, J. M., Ipatov, M., Churyukanova, M., Taskaev, S., & Zhukov, A. (2018). Tailoring of magnetoimpedance effect and magnetic softness of Fe-rich glass-coated microwires by stress-annealing. *Scientific Reports*, 8(1), 3202. <https://doi.org/10.1038/s41598-018-21356-3>
- [70] Vasić, M. M., Žák, T., Pizúrová, N., Roupcová, P., Minić, D. M., & Minić, D. M. (2018). Thermally induced microstructural transformations and anti-corrosion properties of Co<sub>70</sub>Fe<sub>5</sub>Si<sub>10</sub>B<sub>15</sub> amorphous alloy. *Journal of Non-Crystalline Solids*, 500, 326–335. <https://doi.org/10.1016/j.jnoncrysol.2018.08.017>
- [71] Frankel, G. S., Vienna, J. D., Lian, J., Scully, J. R., Gin, S., Ryan, J. V., Wang, J., Kim, S. H., Windl, W., & Du, J. (2018). A comparative review of the aqueous corrosion of glasses, crystalline ceramics, and metals. *Npj Materials Degradation*, 2(1), 1–17. <https://doi.org/10.1038/s41529-018-0037-2>
- [72] Yazdani, A., Höhne, G. W. H., Misture, S. T., & Graeve, O. A. (2020). A method to quantify crystallinity in amorphous metal alloys: A differential scanning calorimetry study. *PLoS ONE*, 15(6 June), e0234774. <https://doi.org/10.1371/journal.pone.0234774>
- [73] Hermans, P. H., & Weidinger, A. (1950). Quantitative investigation of x-ray diffraction by “amorphous” polymers and some other noncrystalline substances. *Journal of Polymer Science*, 5(3), 269–281. <https://doi.org/10.1002/pol.1950.120050301>
- [74] Hermans, P. H., & Weidinger, A. (1948). Quantitative x-ray investigations on the crystallinity of cellulose fibers. A background analysis. *Journal of Applied Physics*, 19(5), 491–506. <https://doi.org/10.1063/1.1698162>
- [75] Falvo, M. R., Clary, G., Helser, A., Paulson, S., Taylor, R. M., Chi, V., Brooks, F. P., Washburn, S., & Superfine, R. (1998). Nanomanipulation experiments exploring frictional and mechanical properties of carbon nanotubes. *Microscopy and Microanalysis*, 4(5), 504–512. <https://doi.org/10.1017/S1431927698980485>
- [76] Karmakar, B. (2017). Functional bulk metallic glasses. In *Functional Glasses and Glass-Ceramics* (pp. 365–390). Elsevier. <https://doi.org/10.1016/b978-0-12-805056-9.00012-x>
- [77] Masumoto, T. (1976). Mechanical Characteristics of Amorphous Metals. *Science reports of the Research Institutes, Tohoku University. Ser. A, Physics, chemistry and metallurgy*, 26, 246-262. <http://hdl.handle.net/10097/27855>
- [78] Ashby, M. F. (1992). *Materials Selection in Mechanical Design* (Second Edi). British Library Cataloguing in Publication Data Library of Congress Cataloguing in Publication.
- [79] Sarkar, P. P., Kumar, P., Manna, M. K., & Chakraborti, P. C. (2005). Microstructural influence on the electrochemical corrosion behaviour of dual-phase steels in 3.5% NaCl solution. *Materials Letters*, 59 (19–20), 2488–2491. <https://doi.org/10.1016/j.matlet.2005.03.030>
- [80] Schroeder, V., Gilbert, C. J., & Ritchie, R. O. (1998). Comparison of the Corrosion Behavior of Bulk Amorphous Metal , Zr 41 . 2 Ti 13 . 8 Cu 12 . 5 Ni 10 Be 22 . 5 , with its Crystallized Form.
- [81] Naka, M., Hashimoto, K., & Masumoto, T. (1978). Effect of metalloid elements on corrosion resistance of amorphous iron-chromium alloys. *Article in Journal of Non-Crystalline Solids*, 28, 403–413. [https://doi.org/10.1016/0022-3093\(78\)90090-X](https://doi.org/10.1016/0022-3093(78)90090-X)
- [82] Masumoto, T., & Hashimoto, K. (1980). CORROSION PROPERTIES OF AMORPHOUS METALS. *Le Journal de Physique Colloques*, 41(C8), C8-894-C8-900. <https://doi.org/10.1051/jphyscol:19808221>
- [83] Froment, M. (1983). *Passivity of Metals and Semiconductors* (1st Editio). Elsevier.

- [84] Virtanen, S., & Böhni, H. (1990). Passivity, breakdown and repassivation of glassy FeCrP alloys. *Corrosion Science*, 31(C), 333–342. [https://doi.org/10.1016/0010-938X\(90\)90128-R](https://doi.org/10.1016/0010-938X(90)90128-R)
- [85] Chen, Y., Fang, M., & Jiang, L. (2017). Multiphysics simulation of the material removal process in pulse electrochemical machining (PECM). *Int J Adv Manuf Technol*, 91, 2455. <https://doi.org/10.1007/s00170-016-9899-z>
- [86] *Thermal Analysis & Rheology Thermal Analysis Application Brief Detection Of The Glass Transition in Metal Glasses By Differential Scanning Calorimetry (DSC) and Dynamic Mechanical Analysis (DMA)*. (n.d.). Retrieved from <http://www.tainst.com>
- [87] Lesz, S., & Dercz, G. (2016). Study on crystallization phenomenon and thermal stability of binary Ni–Nb amorphous alloy. *Journal of Thermal Analysis and Calorimetry*, 126(1), 19–26. <https://doi.org/10.1007/s10973-016-5786-y>
- [88] Stark, W., & Bohmeyer, W. (2013). Non-destructive evaluation (NDE) of composites: Using ultrasound to monitor the curing of composites. In *Non-Destructive Evaluation (NDE) of Polymer Matrix Composites: Techniques and Applications* (pp. 136–181). Elsevier Ltd. <https://doi.org/10.1533/9780857093554.1.136>
- [89] Daw, J. E. (2008). *Measurement of Specific Heat Capacity Using Differential Scanning Calorimeter*. Retrieved from <http://www.inl.gov>
- [90] Reardon, A. C. (2011). *Steel Metallurgy for the Non-Metallurgist* (Second). ASM International.
- [91] Popov, B. N. (2015). Basics of Corrosion Measurements. In *Corrosion Engineering* (pp. 181–237). Elsevier. <https://doi.org/10.1016/b978-0-444-62722-3.00005-7>
- [92] Enos, D. G., & Scribner, L. L. (n.d.). *The Potentiodynamic Polarization Scan*. Retrieved from <http://www.solartron.com>
- [93] Amadou, T., Braham, C., & Sidhom, H. (2004). *Double Loop Electrochemical Potentiokinetic Reactivation Test Optimization in Checking of Duplex Stainless Steel Intergranular Corrosion Susceptibility*.
- [94] Neale, Z. (2020). Inductively coupled plasma optical emission spectroscopy (ICP-OES) Overview - YouTube. Retrieved April 27, 2021, from [https://www.youtube.com/watch?v=InFhIHPZYIc&ab\\_channel=ZacharyNeale](https://www.youtube.com/watch?v=InFhIHPZYIc&ab_channel=ZacharyNeale)
- [95] He, M., Hu, B., Chen, B., & Jiang, Z. (2017). Inductively coupled plasma optical emission spectrometry for rare earth elements analysis. *Physical Sciences Reviews*, 2(1). <https://doi.org/10.1515/psr-2016-0059>
- [96] Fazakas, E., Varga, B., Varga, L. K. (2012) Study of Amorphous-Crystalline Phase Transformations by DSC and Dilatometer in the Case of Al-based Amorphous Alloys. *ISRN Metallurgy*, 2012, 1-5. <https://doi.org/10.5402/2012/602108>
- [97] Mendes, M. A. B., Kiminami, C. S., Filho, W. J. B., Bolfarini, C., De Oliveira, M. F., Kaufman, M. J. (2015) Crystallization behavior of amorphous Ti51.1Cu38.9Ni10.0 alloy. *Materials Research*, 18, 104-108. <https://doi.org/10.1590/1516-1439.343014>
- [98] Jafary-Zadeh, M., Praveen Kumar, G., Brancio, P., Seifi, M., Lewandowski, J., & Cui, F. (2018). A Critical Review on Metallic Glasses as Structural Materials for Cardiovascular Stent Applications. *Journal of Functional Biomaterials*, 9(1), 19. <https://doi.org/10.3390/jfb9010019>
- [99] Kim, T. S., Hong, S. J., & Lee, B. T. (2003). Hardness behavior of the partially crystallized amorphous Al86Ni9Mm5 alloys. *Materials Science and Engineering A*, 363(1–2), 81–85. [https://doi.org/10.1016/S0921-5093\(03\)00597-5](https://doi.org/10.1016/S0921-5093(03)00597-5)
- [100] Li, F. C., Liu, T., Zhang, J. Y., Shuang, S., Wang, Q., Wang, A. D., ... Yang, Y. (2019, December 1). Amorphous–nanocrystalline alloys: fabrication, properties, and applications. *Materials Today Advances*. Elsevier Ltd. <https://doi.org/10.1016/j.mtadv.2019.100027>
- [101] Cordero, Z. C., Knight, B. E., & Schuh, C. A. (2016). Six decades of the Hall–Petch effect – a survey of grain-size strengthening studies on pure metals. *International Materials Reviews*, 61(8), 495–512. <https://doi.org/10.1080/09506608.2016.1191808>